

UNIVERSITÀ DEGLI STUDI “ROMA TRE”



Corso di Dottorato di Ricerca in Fisica
XXXIII Ciclo

**Towards a Reconstruction of Supernova
Progenitor Mass by using the Neutrino spectrum
measured with the JUNO detector**

Cristina Martellini

Docente guida:

Prof. Stefano Maria Mari

Coordinatore:

Prof. Giuseppe Degrassi

This page is intentionally left blank.

Contents

Contents	i
Introduction	2
1 Supernova Neutrinos	3
1.1 Supernova classification	4
1.2 Supernova rates	7
1.3 Core-collapse supernova dynamics	9
1.4 SN1987A	19
1.4.1 Kamiokande-II	19
1.4.2 IMB	22
1.4.3 Baksan	22
1.4.4 Comparison with supernova theory	23
1.5 Neutrino mixing	24
1.6 Future	25
2 The JUNO experiment	27
2.1 Experimental Site	28
2.2 Detector Systems	28
2.2.1 Liquid Scintillator	29
2.2.2 Stainless Steel Truss	31
2.2.3 Photo-multiplier tubes	31
2.2.4 Shielding and veto systems	32
2.2.5 OSIRIS	34
2.2.6 TAO	35
2.2.7 DAQ and Trigger strategy	35
3 Software Framework and Data	39
3.1 MC Simulation	40
3.2 Supernova neutrino flux	42
3.3 Flavor Conversion of SN burst neutrinos	43
3.4 Neutrino Interactions	44
3.4.1 Inverse Beta Decay	45

3.4.2	Neutrino-proton elastic scattering	46
3.4.3	Neutrino-electron elastic scattering	46
3.4.4	^{12}C CC and ^{12}C NC	47
3.5	Detector Simulation	48
3.6	Electronic Simulation	49
3.7	Calibration	49
4	Neutrino Identification and sample selection	51
4.1	Fiducial cuts	52
5	Supernova neutrino energy spectrum	61
5.1	Neutrino flavour transition in supernovae	63
5.2	Neutrino mass physics from Supernova neutrinos	64
5.3	Spectrum Unfolding	65
5.4	Bayes Unfolding	67
5.4.1	Simulated data sample	70
5.5	Reconstructed Flux	70
5.6	Uncertainties evaluation	72
5.6.1	Background	74
6	Progenitor Mass Reconstruction	85
6.1	Mass Reconstruction	88
	Conclusions	96
	A Additional Unfolding Results	97
A.1	Additional Unfolding Results for the Nakazato Model	97
	Bibliography	101

Introduction

Neutrinos are elementary particles which are copiously produced thanks to several different processes. The first observation of these particles is in the 1950s and since then a lot of efforts have been made to find different and more effective ways to detect them. Among the variety of processes, a supernova explosion represents a valuable source to detect them.

In 1987 a supernova was observed in the Magellanic Cloud, ref.[1]. This was the first explosion of a star not only detected by electromagnetic radiation, but also through neutrino detection, ref.[1]. Only dozen of neutrinos were registered from the collapse of the SN1987A, but it was enough to confirm theoretical assumptions, that when a massive star collapse into a supernova explosion includes a massive production of neutrinos, see ref.[2]. Within the years a lot of progresses have been made in the detection and understanding of the neutrino processes.

While it is unknown when the next core-collapse supernova will happen, its neutrino signal will be measured through the neutrino flux with unprecedented accuracy by different detectors around the world. The Jiangmen Underground Neutrino Observatory is one of the most prominent candidates for this task. The JUNO experiment is under construction in China, since 2015 and it will consist of a 20 kton liquid scintillator with a great energy resolution ($3\%/\sqrt{MeV}$). JUNO is a multipurpose neutrino experiment designed to determine the neutrino mass ordering by measuring the anti-neutrino energy spectrum coming from nearby nuclear power plants, observe supernova neutrinos, study atmospheric, solar neutrinos and geo-neutrinos. It is a spherical volume of liquid scintillator, that is placed around 700 m underground and it will start data taking in early 2022. The very high light yield of the scintillator and optimal transparency, together with the angular photo-coverage will assure the measurement with great accuracy.

In this work is reported the attempt to reconstruct the supernova neutrino energy spectrum from a galactic core-collapse supernova. A large set of supernova MC simulation have been used to simulate the performance of the detector. An independent simulation has been generated as data sample to evaluate the potential of the detector in case of a SN burst. The event is then processed in subsequent event reconstruction stage.

The second part of this work presents a probabilistic algorithm with the purpose of retrieving the progenitor mass of the supernova that generated the neutrino flux in the detector, at a fixed distance.

Chapter1 gives a brief overview of supernova neutrino physics and the unanswered

question in this field. Chapter2 describes the final design of the JUNO detector. Chapter3 gives an overview of the JUNO software framework and the MC simulation used for this work. Chapter4 describes the selection criteria applied for the study of the supernova neutrino energy spectrum, in Chapter5 the unfolding procedure of the spectrum is presented and discussed, and at last, in Chapter6 the reconstruction of the progenitor mass is discussed and final results are presented.

Chapter 1

Supernova Neutrinos

Supernovae (SNe) are extremely powerful explosions happening when a star life ends. Usually, some solar masses are ejected in the interstellar space with a kinetic energy of the order of 10^{51} erg. The ejecta includes heavy elements that are important for the chemical evolution of galaxies, stars and planets. Some SNe produce a compact remnant, a neutron star or a black hole, which may be observed.

After in 1920s there was the understanding that if the spiral nebulae are extragalactic star systems some of the novae observed in these spiral nebulae have been extremely bright [3]. W.Baade and F.Zwicky were between the first people to suggest that the great energy released from a SN comes from the gravitational collapse of a star to a neutron star and that SNe may be source of cosmic rays. Subsequent studies have shown the presence of thousands of SNe. During all the studies it was decided a naming scheme for SNe: each Supernova is indicated with a prefix followed by the year of discovery, which is followed, in years where there are more than one supernova, by an upper-case letter A through Z for the first 26 SNe discovered in a given year or the lower-case letters *aa*, *bb*,...for the subsequent SNe discovered in the same year.

Some of the SNe that exploded in our galaxy have been observed with a naked eye during the last 2000 years [4]. The most famous one is the one that created the Crab nebula and the Crab Pulsar (1054 Supernova), whilst the 1006 Supernova is the brightest of all times. In the last few centuries many SNe occurring in the other galaxies have been observed with telescopes since their light emission is comparable to the one emitted from an entire galaxy. Supernova 1987A, which occurred on 23rd of February 1987 in the Large Magellanic Cloud, is the best studied of all SNe ([5], [6], [7]) and it was the only one to be also detected through its neutrino emission. This first historical observation of neutrinos outside of the solar system (and outside of our galaxy) it is important for SN dynamics but also for the study of the neutrino properties, and in particular for the study of neutrino masses.

1.1 Supernova classification

SNe are classified into different types due to their spectroscopic characteristics near minimum luminosity and by the properties of the light curve, which depend on the composition of the envelope of the SN progenitor star. A schematic image is presented below.

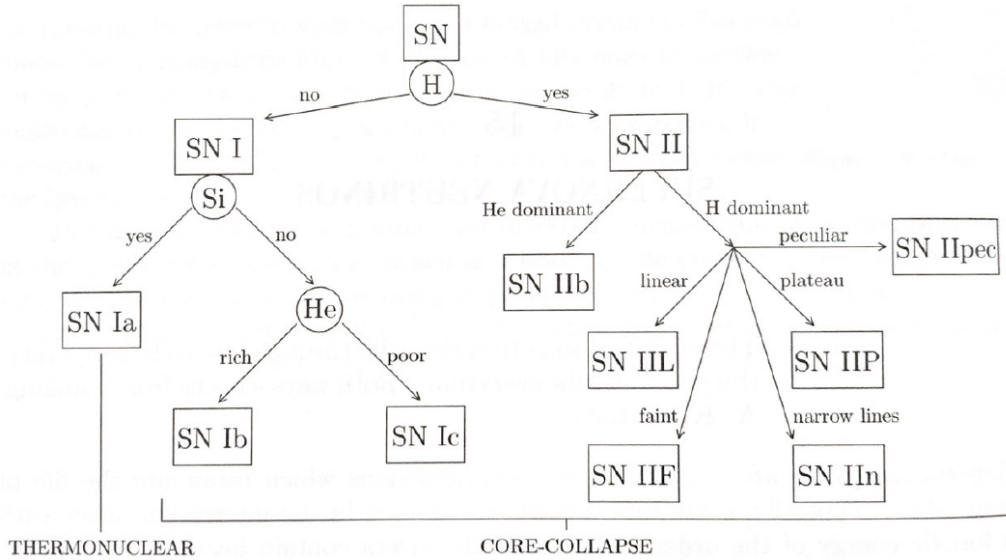


Figure 1.1: The Supernovae classification scheme.

The first big classification is between type I and type II Supernovae, respectively indicating the absence or the presence of hydrogen lines. Despite this, the most important physical characteristic between different types is given by the different exploding mechanism, which allows us to distinguish SNe type I from type Ib, Ic or II, as shown in Fig. 2.3. This difference becomes relevant in the light spectrum some months after maximum luminosity, when the ejecta material becomes optically thin and the innermost regions becomes therefore visible: while the type Ia SN spectrum is dominated by *Fe* emission lines, the Ib, Ic and II SNe show *O* and *C* emission lines. SNe are classified as Type I if their light curves exhibit a narrow luminosity peak and then they die away smoothly and gradually.

Type II SNe have broad peaks compare to Type I. The subclass Ia refers to those which have a strong Silicon line at 615nm, while type Ib have strong helium lines and Ic do not.

Studies led us to believe Type Ia SNe can be generated by carbon-oxygen white dwarfs with a close companion star from which the white dwarf can accrete its mass. Those stars are the evolutionary products of stars which ended thermonuclear fuel burning. They are about $\sim 1 M_{\odot}$, with a radius of about ~ 5000 km and a density of the order of 10^6 g cm^{-3} . They are characterized by a electron degenerate pressure that supports the white dwarfs against the inwards pull of gravity. When white dwarfs accrete their mass enough to exceed the *Chandrasekhar Mass* (which was discovered in 1931 was discovered to be the maximum mass that a white dwarfs can have before exploding and it equals $1.4 M_{\odot}$).

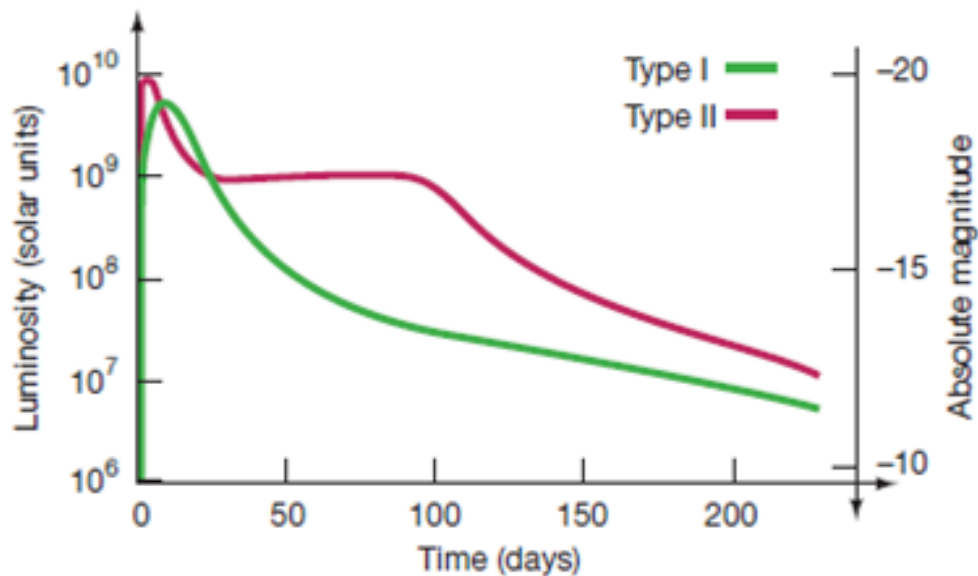


Figure 1.2: Light curves of typical Type I and Type II SNe both show that their maximum luminosities can sometimes reach that of billion suns, but there are differences in the decline of luminosity after the initial peak.

It was Landau that in 1932 presented a qualitative derivation of the Chandrasekhar limit [8], which can be applied to the calculation of the limit of stability of neutron stars too, by replacing electrons with neutrons. If we consider a white dwarf with N electrons and radius R . According to the Pauli exclusion principle, the volume per electron is $v \sim R^3/N$, with a characteristic size of $r \sim v^{1/3} \sim R/N^{1/3}$. Applying then, the Heisenberg uncertainty principle, the momentum of an electron is $p \sim r^{-1} \sim N^{1/3}/R$. The pressure which balances the inward pull of gravity is due to degenerate electrons. For small stellar masses these electrons are non-relativistic and the star can find an equilibrium between pressure and gravity. For more massive stars, during contraction the central density becomes so high that relativistic regime is reached. In this case, the electron mass can be neglected and the pressure energy is given by $E_p \simeq p \sim N^{1/3}/R$. Each electron is associated with a mass $m \simeq m_N/Y_e$, where m_N is the nucleon and Y_e is the electron fraction ($Y_e = \frac{N_p}{N_n+N_p}$, where N_p and N_n are the numbers of protons and neutrons, respectively). This allows us to say that the gravitational energy per electron is $E_G \sim \frac{-G_N M m}{R} \sim \frac{-G_N m_N^2 N Y_e^{-2}}{R}$, where $M \simeq mN \simeq m_N N/Y_e$ is the total mass. The equilibrium of the star is reached at a minimum of the total energy:

$$E = E_P + E_G \sim \frac{N^{1/3}}{R} - \frac{G_N m_N^2 N Y_e^{-2}}{R} \quad (1.1)$$

Since both terms scale with $1/R$, if E is negative, the total energy can decrease without any limit decreasing R , leading to the star' collapse. In order to reach a stable configuration,

the total energy must be positive, yielding the upper bound:

$$N < N_C \sim (G_N m_N^2 Y_e^{-2})^{-3/2} = \left(\frac{M_P Y_e}{m_N} \right)^3 \simeq 2 \cdot 10^{57} Y_e^3 \quad (1.2)$$

The corresponding mass is the Chandrasekhar mass:

$$M_C \sim N_C m_N Y_e^{-1} \sim 2 \cdot 10^{57} Y_e^2 \text{ GeV} \simeq 2 Y_e^2 M_\odot \quad (1.3)$$

This brings us for a typical value of $Y_e \simeq 0.5$, to have $M_C \simeq 1.46 M_\odot$.

When the Chandrasekhar limit is reached, the stars becomes unstable, this because the degenerate electron gas pressure can no longer sustain the gravitational weight. It is at this point that the white dwarf begins to collapse, triggering the fusion of carbon and oxygen to heavy nuclei, which releases an enormous quantity of energy, causing the thermonuclear explosion of the star [9]. This explosion disrupts the progenitor white dwarf and generates an expanding nebula without a central compact object.

The light emission of a type Ia SNe is mainly given by the decay of ^{56}Ni , which is produced abundantly during the collapse of the outer layer of the core. It contains silicon absorption lines, because Si is a product of C and O fusion. The ^{56}Ni decays into ^{56}Co , which then decays into ^{56}Fe , whose emission lines dominates the spectrum some months later. Iron and other heavy nuclei are ejected in interstellar space by the explosion.

SNe of type Ia are all generated under similar physical circumstances, therefore they all have almost identical characteristics, the most important being the amount of energy being released and the *light curve*, i.e. they release almost the same total light and the visible light decays at the same rate. This has been confirmed by the observation of many type Ia SNe in nearby galaxies of known distance.

An empirical relation between the duration of the peak phase of the light curve and the luminosity of type Ia SNe has been discovered by Phillips in 1993 [10]. This width-luminosity relation (bringing to *broader is brighter*) allows us to use of type Ia SNe also as standard candles for the measurement of the distance of galaxies as far as 100 Mpc or more [11].

From the point of view of neutrino physics, type Ib, Ic, and II SNe are much more interesting than type Ia SNe, simply because they produce a huge flux of neutrinos of all types. These SNe are generated by the collapse of the core of massive stars ($M \simeq 8 M_\odot$), which leaves a compact remnant. During the few seconds following the collapse, the compact remnant is very hot and neutrinos of all types are copiously produced. Since the remnant and the surrounding envelope are optically thick, about 99% of the gravitational binding energy liberated by the collapse (about $3 \cdot 10^{53} \text{ erg}$) is carried away by neutrinos. The average energy of the emitted neutrinos is of the order of 10 MeV, and their number is about 10^{58} , one order of magnitude larger than the lepton number of the collapsed core.

Type II SNe are supposed to be generated by the core collapse of red (or blue as for SN1987A) giant stars with mass between about 8-20 and 40-60 Solar masses. Since the size and mass of the hydrogen envelope can be very different from star to star, even if

Rate [$10^{-2}y^{-1}$]	Reference
5.8 ± 2.4	Tammann (1982) [14]
$1.2^{+1.7}_{-0.7}$	Ratnatunga & Van der Bergh (1989) [15]
3^{+2}_{-1}	Strom (1990) [16]
4.0 ± 2.0	Muller et al. (1992) [17]
2.0 ± 1.1	Cappellaro et al. (1993)[18]
3.0 ± 1.5	Van der Bergh (1993)[19]
$2.5^{+0.8}_{-0.5}$	Tamman et al. (1994)[20]
5.7 ± 1.7	Strom (1994)[21]
1.3 ± 0.9	Cappellaro et al (1997) [22]
3.4 ± 2.8	Timmes et al. (1997) [23]
8.4 ± 2.8	Dragicevich et al. (1999) [24]
1.5 ± 1.0	Cappellaro & Turatto (2000) [25]
1 - 2	Reed (2005) [26]

Table 1.1: Estimates of the rate of core-collapse SNe in the Milky-Way.

they have the same initial mass, the visible effect of the supernova explosion have a wide range of variability, leading to a further classification of type II SNe into the subtypes [12]: again there are two types of SNe subtypes, the ones determined by properties of the light curve and the ones classified by the spectral properties.

Supernova SN1987A was an extreme case of type IIP (those type of SNa which shows a plateau in the luminosity), since the luminosity increased for about 3 months after the collapse and the supernova was rather faint (characteristic that usually belongs to the subtype IIF). So sometimes the SN1987A is classified as one or another. Its faintness is most likely due to the compactness of the progenitor (radius of about 10^{12} cm). If this is the case, much of the available energy is used in the expansion and the luminosity increases for some time because of the growing contribution of radioactive decay of heavy elements in inner shells, which becomes more visible as the envelope expands.

1.2 Supernova rates

A very important problem is how to estimate SNe rates. Fig. 1.3 shows the estimates of SN rates presented in [13].

One can see that SN rates depend strongly on galaxy type. No core-collapse SNe of type Ib/c and II have been observed in elliptical galaxies, which are very old and have a little star formation which could produce short-lived massive stars ending their life with a core-collapse supernova explosion.

One of the most important questions for SN neutrino astronomy is the rate of core-collapse SNe in our galaxy, which could produce observable neutrino bursts with high statistics in neutrino telescopes. Estimates of the rate of core-collapse SNe in the Milky-Way are summarized in Tab. 1.1.

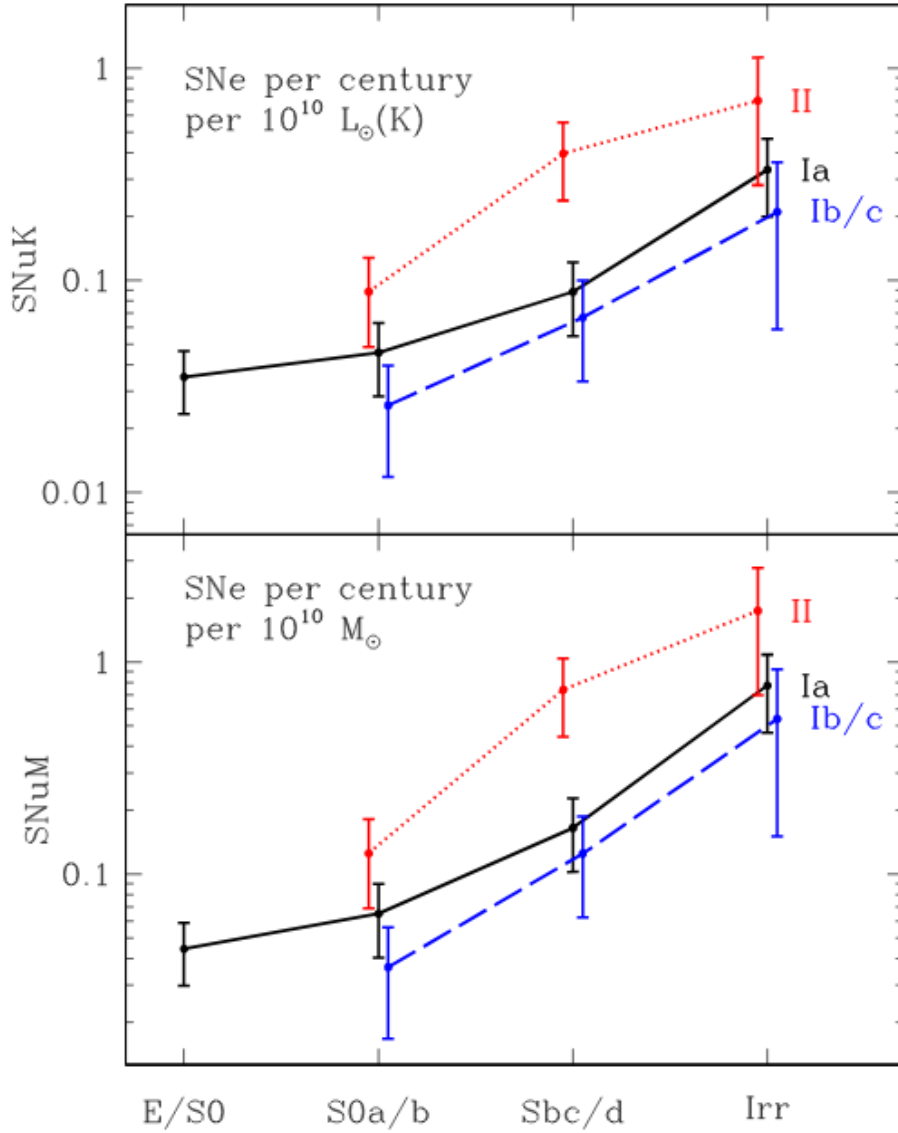
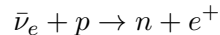


Figure 1.3: SN rate as a function of the galactic morphological index [13]. *Upper panel:* SN rate expressed in SNUK (number of SNe per century per $10^{10} L_{\odot}$ of luminosity in the K band). *Lower panel:* SN rate expressed in SNUM (number of SNe per century per $10^{10} M_{\odot}$). The lines correspond to type Ia (solid), type II (dotted) and Ib/c (dashed), with 1σ error bars

This shows of course, that the large uncertainties leaves the problem open to further study. The lack of observation of neutrinos from core-collapse SNe in our galaxy since the Baksan Underground Scintillator Telescope began observations in June 1980 imply upper bound of 13 SNe per century in the Milky Way at 90% CL. This measurements is consistent with the estimated rates and shows that the true rate cannot be much higher than the estimations.

The rate of core-collapse SNe is also important for the estimation of the *Relic Supernova Neutrino Background* (RSNB) [27]. The Super-Kamiokande collaboration [28] searched for $\bar{\nu}_e$'s of the RSNB by means of the inverse neutron decay process shown below:



For neutrino energies above the end points of the 8B and the *hep* solar neutrino spectra. Since no signal was observed, the Super-Kamiokande data yielded the upper bound [28]:

$$\Phi_{\bar{\nu}_e}(E > 19.3MeV) < 1.2cm^{-2}s^{-1} \quad (90\% CL)$$

1.3 Core-collapse supernova dynamics

Supernovae produced by the collapse of the core of massive stars produce large fluxes of neutrinos that could be detected on Earth. Here a short description of the current standard theory of the dynamics of core-collapse SNe and the resulting neutrino flux (see [8, 29]). As explained in Section 1.1, core-collapse SNe are classified as of types II, Ib, or Ic depending on their spectroscopic characteristics at maximum luminosity. However, these characteristics depend only on the composition of the envelope, which plays no role in the collapse of the core and neutrino production. Therefore, the following theory applies equally well to all types II, Ib, and Ic core-collapse SNe.

Core-collapse SNe are the final explosion of single stars with mass between about 8-9 and 40-60 Solar Masses. The explosion is due to the shock wave created when the core-collapses to a proto-neutron star, which ejects the stellar envelope. Stars lighter than about $9M_{\odot}$ end their life as white dwarfs (but may explode as type Ia SNe if they belong to a multiple system). As shown in Fig. 1.4, stars heavier than about $40 M_{\odot}$ can end their life in a supernovae explosion if they have a sufficient initial metallicity [30], i.e. abundance of heavy elements (especially iron), which implies a larger photon opacity. During their life, these stars go through significant mass losses because of the stellar wind, leading to smaller envelopes which can explode when the core collapses to a proto-neutron star. The core of low and medium metallicity stars, with masses included between 25 and $40 M_{\odot}$ initially collapses to a proto-neutron star, generating a weak SN IIP, to then collapse to a black-hole because of the increase of mass of the proto-neutron star due to the fallback of the envelope.

Stars with masses in excess of about $10 M_{\odot}$ are thought to undergo all the stage of nuclear fusion of hydrogen, helium, carbon, oxygen, neon, silicon, until the star has an onion-like structure shown in Fig. 1.5, with an iron core surrounded by shells composed of elements with decreasing atomic mass. At this point the iron core has a mass of about $1M_{\odot}$, a radius of a few thousands km's, a central density fo about $10^{10}gcm^{-3}$, a central temperature of roughly 1 MeV and its weight is sustained by the pressure of degenerate relativistic electrons.

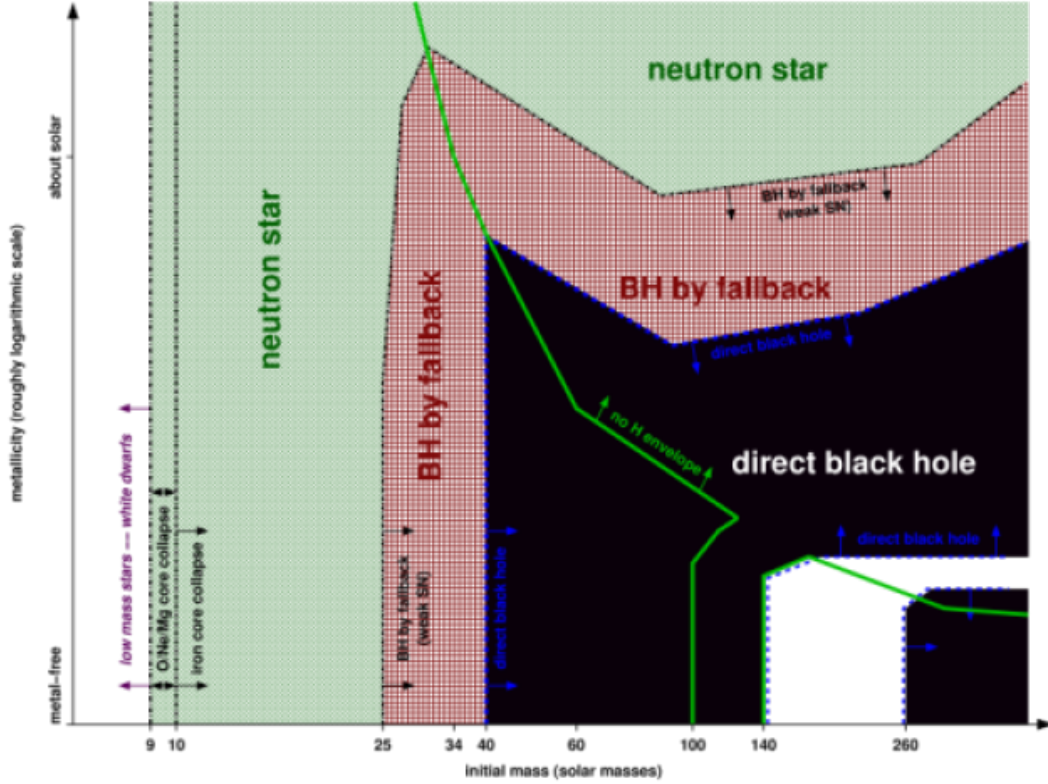


Figure 1.4: Remnants of massive single stars as a function of initial mass (x axis) and initial metallicity (y axis) [30]. The line marked *no H envelope* separates the regimes where the stars keep their hydrogen envelope (left and lower right) from those where the hydrogen envelope is lost (upper right and small strip at the bottom between 100 and 140 M_{\odot}). The line marked *direct black-hole* points the border of the regime of direct black-hole formation (black). This domain is interrupted by a strip of pair-instability supernovae that leave no remnant (white). Outside the direct black-hole formation region, at lower mass and higher metallicity, there is the regime of black-hole formation by fallback. And again, outside of this, there is the formation of neutron stars. The lowest mass neutron stars may be made by O/Ne/Mg core collapse rather than iron core collapse (vertical dash-dotted lines at the left). At even lower masses, there is not a core collapse and only white dwarfs can be made (white strip at the very left).

Since iron is the most tightly bound nucleus, there remains no thermonuclear fuel to burn. The core contracts and the increased temperature causes photo-dissociation of iron through the following process:



This reaction absorbs about 124 MeV of energy and reduces the kinetic energy and pressure of the electrons. Electron capture of nuclei and free protons, both shown underneath in Eq. 1.5 and Eq. 1.6, favored by the high electron Fermi energy, additionally reduces the

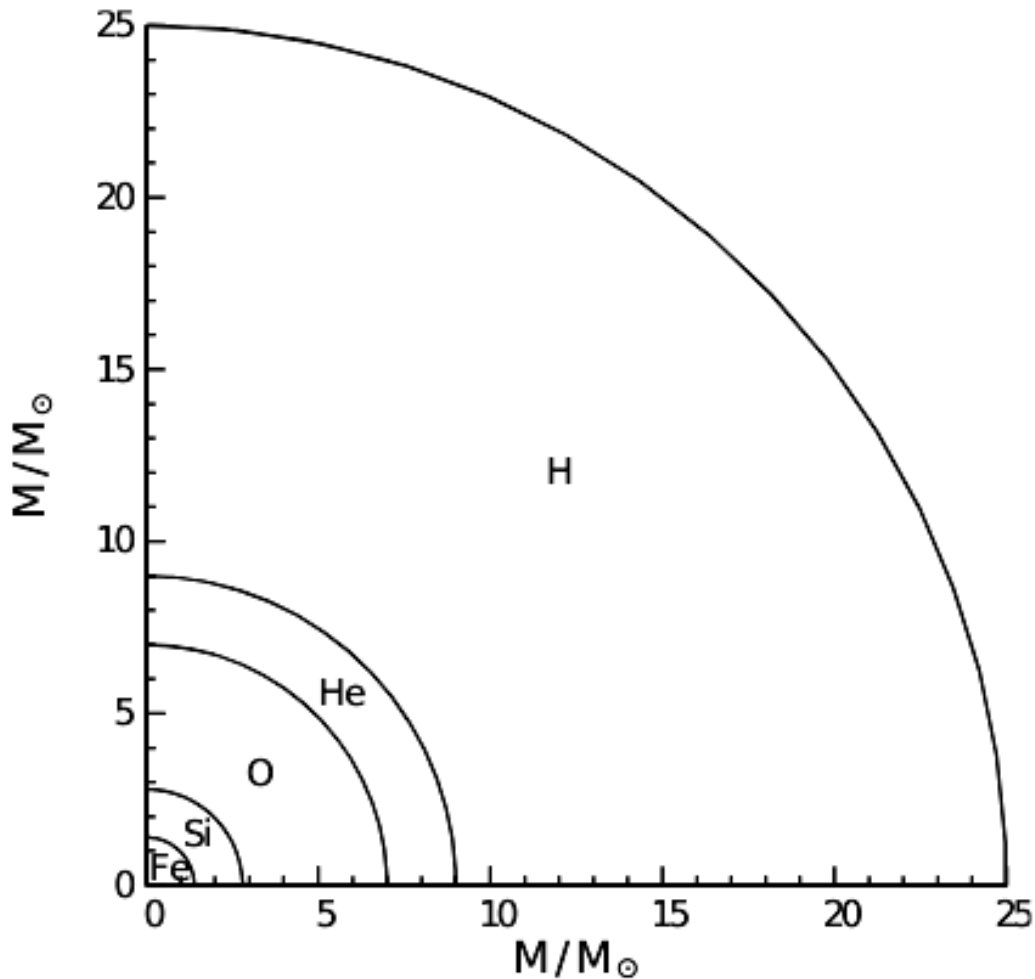
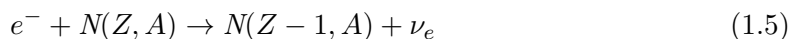


Figure 1.5: Onion-like interior structure of a Population I star of $25 M_{\odot}$ just before the genesis of the collapse [3]. Fe represents assorted iron-peak elements: ^{48}Ca , ^{50}Ti , ^{54}Fe , ^{58}Fe , ^{66}Ni . The Si shell contains less abundant amounts of S, O, Ar, Ca, the O shell contains less abundant amounts of He, Ne, O, N, C.

number and pressure of the electrons.



At the genesis of the collapse, when the density of the iron core is not too high, the electron neutrinos produced by electron capture leave the core carrying away most of the kinetic energy of the captured electrons. The combined effect of iron photo-dissociation and electron capture lower the electron pressure, decreasing therefore the value of the Chandrasekhar Mass, until the Chandrasekhar mass becomes smaller than the core mass. At this point the pressure of degenerate relativistic electrons cannot sustain the weight of

the core anymore and the collapses begins. As the density and the temperature increase, the process described in Eq. 1.4 and Eq. 1.6 proceed faster, lowering further the electron pressure and favoring the collapse, which therefore accelerates. According to theory, stars with mass between 9 - 10 M_{\odot} burn hydrogen, helium, carbon, but the core does not get hot enough to burn oxygen. In the core there are neon and magnesium at high density, and it can undergo electron capture, reducing the electron pressure that sustains the core against gravity. As a result, the core collapses and, during the collapse, oxygen, neon and magnesium are converted to iron. Therefore, also in this case, the supernova explosion energy is produced by the collapse of an iron core.

The result of the collapse of the core creates a neutron star and a huge amount of gravitational energy is released mainly as neutrino flux, with a small fraction as electromagnetic radiation and kinetic energy of the ejecta, which form the visible explosion. The released gravitational energy is about 3×10^{53} erg, of which 0.01 % is transformed into electromagnetic radiation while 1% is transformed into kinetic energy of the ejecta.

The electron neutrinos produced by the electron capture process in Eq. 1.5 and Eq. 1.6 initially leave the core freely, carrying away energy and lepton number since their mean free path is longer than the radius of the core. In this so-called *capture* phase electron neutrinos have a non-thermal spectrum and average energy that grows from about 12 to about 16 MeV. The luminosity reaches about 10^{53}ergs^{-1} , but, in total only about 10^{51} erg are released before the core bounce, because, the capture phase is too short (less than about 10 ms). When the density of the inner part of the core (about $0.8 M_{\odot}$) raises above $3 \times 10^{11} \text{gcm}^{-3}$, neutrinos are trapped in the collapsing material leading to an adiabatic collapse with constant lepton number. During this stage, the inner part of the core collapses with subsonic velocity proportional to the radius. On the outer side, the outer part of the core collapses with supersonic free-fall velocity.

When the core reaches its instability stage, after one second roughly from its start, the core density becomes the one of nuclear matter, $\sim 10^{14} \text{gcm}^{-3}$, and the degenerate pressure of non relativistic nucleons stops the collapse. The inner core reaches and settles into hydrostatic equilibrium, forming a proto- neutron star with a radius of $\sim 10 \text{km}$, while a shock wave caused by the stumbling and rebound of the inner core forms at its surface. The shock propagates outward through the outer iron core, which although is still collapsing, with an initial velocity of the order of 100 km msec^{-1} . The gas that is in-falling at free-fall velocity is decelerated within the shock. As a consequence of this the proto-neutron star develops an un-shocked core and a shocked mantle. The core has a radius of $\sim 10 \text{km}$ with a density of about 10^{14}gcm^{-3} , as a nucleus. The mantle has a radius of 100 km , with a density decreasing from the nuclear density of the core to about 10^9gcm^{-3} at the surface of the proto-neutron star, where the density has a steep reduction of several orders of magnitude.

As the shock propagates through the in-falling dense matter of the outer core, the energy is dissipated by the photo-dissociation of nuclei into protons and neutron. This means, the material behind the shock wave is mainly composed of free nucleons. Free protons have a

high electron capture rate, guiding the transformation of most protons into neutrons, with a conspicuous amount of electron neutrinos produced. These neutrinos pile up behind the shock, which is dense and opaque to them, until the shock reaches an area with density of the order of 10^{11}gcm^{-3} , which is called *shock breakout*, a few milliseconds after the bounce and the electron neutrinos behind the shock are released in the subsequent few milliseconds.

The neutrino emission is called a *prompt electron neutrino burst*, or *neutronization burst*, or *breakout pulse*, to distinguish it from the thermal production of all flavor neutrinos. The characteristics of the neutronization burst include a luminosity peak of $6 \times 10^{51} \text{ergs}^{-1}$, carrying away a few 10^{51}erg in few milliseconds, and neutronize just the low density periphery of the star, while the core remains trapped. The energy loss due to photo-dissociation of nuclei and neutrino emission weakens the shock ($\sim 1.5 \times 10^{51} \text{erg}$ are dissipated for each $0.1 M_{\odot}$ of photo-dissociated material).

Although, the shock, once reached the *prompt* SN explosion scenario, is able to expel the envelope of the star generating the SN explosion on a time scale of the order of 100 ms. If the progenitor mass is more than $10 M_{\odot}$, the shock is weakened and stalls after about 100 ms from the bounce, at a 200-300 km radius, with insufficient energy to extend to the outer layers. Matter continues to fall through the stalled shock, but if too much matter lands on the proto-neutron star, the pressure of degenerate nucleons is not enough to maintain stability and the core collapses into a black -hole, in all probability without a SN explosion. The conditions that allow a prompt SN explosion, without a stalling shock, are controversial and are supposed to depend on the mass of the progenitor star and on the equation of state of nuclear matter, which determines the energy transferred to the shock wave by the bounce.

In case the shock stalls, the SN explosion can only be achieved if the shock is revived by some mechanism that is able to renew its energy. The mechanisms which is currently thought to be able to do this , is the energy deposition by the huge neutrino flux thermally produced in the proto-neutron star [31]. It has been realized that the shock revival is helped by the convectional motion behind the shock , which can bring to an asymmetric explosion [32]. If the shock is revived, a so-called *delayed* SN explosion is produced on a time scale of the order of 0.5 s after the bounce.

Neutrinos of all flavors are produced in the hot core of the proto-neutron star, which has a temperature of about 40 MeV, through electron-positron pair annihilation,

$$e^{-} + e^{+} \rightarrow \nu + \bar{\nu} \quad (1.7)$$

electron-nucleon bremsstrahlung,

$$e^{\pm} + N \rightarrow e^{\pm} + N + \nu + \bar{\nu}, \quad (1.8)$$

nucleon-nucleon bremsstrahlung,

$$N + N \rightarrow N + N + \nu + \bar{\nu}, \quad (1.9)$$

plasmon decay,

$$\gamma \rightarrow \nu + \bar{\nu}, \quad (1.10)$$

and photo-annihilation:

$$\gamma + e^\pm \rightarrow e^\pm + \nu + \bar{\nu}. \quad (1.11)$$

Electron neutrinos are also produced by the electron capture process in Eq. 1.6, and electron antineutrinos are produced by positron capture on neutrons:

$$e^+ + n \rightarrow p + \bar{\nu}_e \quad (1.12)$$

Despite their weak interactions, these neutrinos are trapped into the SN core because of the very high matter density. Neutrinos can free-stream out of the mantle of a proton-neutron star only at a distance from the center where the matter density is low enough (of the order of 10^{11}gcm^{-3}) so that the neutrino mean free path is larger than the radius of the core. This region where they can freely stream out is called *neutrinosphere*, and it lies within the mantle of the proto-neutron star. Forasmuch as neutrino interactions depend on flavor and energy, there are different energy-dependent *neutrinospheres* for different neutrino's flavors. More precisely, since the medium is composed of protons, neutrons and electrons, and the neutrino energy does not allow creation of muons and taus, the ν_e and $\bar{\nu}_e$ neutrinos flavor can interact with the medium through both charged-current and neutral-current weak processes, whereas the $\nu_\mu, \bar{\nu}_\mu, \nu_\tau, \bar{\nu}_\tau$ neutrinos can only interact through neutral-current weak processes, which are flavor-independent. Consequently we can only distinguish three energy-dependent *neutrinosphere*: one for ν_e , one for $\bar{\nu}_e$ and one for $\nu_\mu, \bar{\nu}_\mu, \nu_\tau, \bar{\nu}_\tau$. We will therefore, address to the latter one collectively as ν_x . Each energy-dependent *neutrinosphere* emits a black-body thermal flux of neutrinos at the considered energy. The estimated radii of the neutrinospheres lies between 50 and 100 km. As already seen, when the shock passes through the electron neutrino neutrinosphere (shock breakout), a few milliseconds after the bounce, a large flux of electron neutrinos is released in a few milliseconds in the neutronization burst. After this phase, each neutrinosphere produces a thermal flux of the corresponding neutrino flavor.

The opacity of ν_e and $\bar{\nu}_e$ are dominated by the following charged-current weak interaction processes:

$$\nu_e + p \rightarrow n + e^+ \quad (1.13)$$

$$\bar{\nu}_e + n \rightarrow p + e^- \quad (1.14)$$

These reactions permit exchanges of energy and lepton number between the neutrinos and

the medium. For example, in the process in Eq. 1.13 the neutrino energy is mainly transferred to the final electron, whose creation increases by one unit the lepton number of the medium (Infact, the kinetic energy of the final neutron is negligible. Momentum conservation implies that the momentum p_n of the final neutron is of the order of the momentum p_{ν_e} of the initial neutrino, which is practically equal to the neutrino energy, because of the smallness of the neutrino masses. So the recoil kinetic energy of the neutron is suppressed by the large mass m_n of the neutron).

Since the mantle of the proto-neutron star is neutron rich, the opacity of ν_e of a given energy is larger than the one of $\bar{\nu}_e$ with the same energy and the corresponding ν_e neutrinosphere has a larger radius than the $\bar{\nu}_e$ one. This means that for a fixed neutrino energy $\bar{\nu}_e$'s are emitted by a deeper and hotter layer than ν_e 's, meaning that $\bar{\nu}_e$ mean energy is larger than ν_e mean energy. Moreover, the spectra do not follow a perfect black-body shape (Fermi-Dirac distribution), but they are *pinched*. So Time wise the flux can be

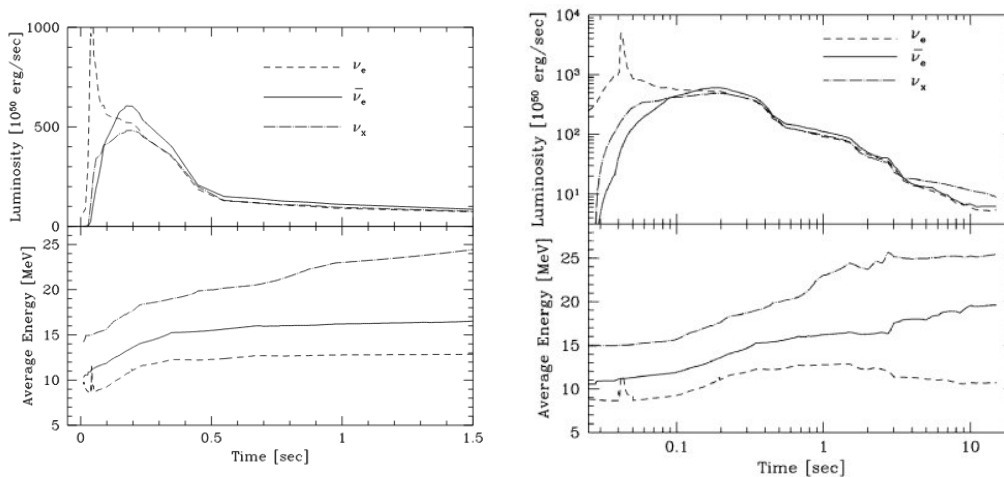


Figure 1.6: Time evolution of the neutrino luminosity and averaged energy obtained from numerical SN model from [33]. The left panel shows the early phase in linear coordinates. The right panel shows the time evolution until about 10 s after the start of the collapse. The dashed lines are for ν_e , the solid lines are for $\bar{\nu}_e$ and the dot-dashed lines for ν_x . The core bounce time is about 3-4 msec before the neutronization burst of ν_e 's.

divided in three-phases as depicted in Fig. 1.7:

1. The *neutronization burst*, which happens shortly (around 2 ms) after the core bounce. Because at this point the central part of the star is set free by the explosion, the ν_e referred to, in Eq. 1.6 can escape in a bulk, resulting in the peak of neutrino luminosity. The other flavors are produced in increasing number following Eq. 1.7 and Eq. 1.9.
2. The subsequent phase is defined by the matter accretion on the remaining proto-neutron star. This way the production of ν_e and $\bar{\nu}_e$ in the mantle of the proto-neutron star keeps being high while the rate for non-electron neutrinos is lower. These neutrinos mainly come from nucleon bremsstrahlung (Eq. 1.9) in the core.

3. In the end the proto-neutron star begins its cooling phase. Over a few tens of second the neutrino luminosity drops to a low level, whereby the differences between the different flavors basically vanish [2].

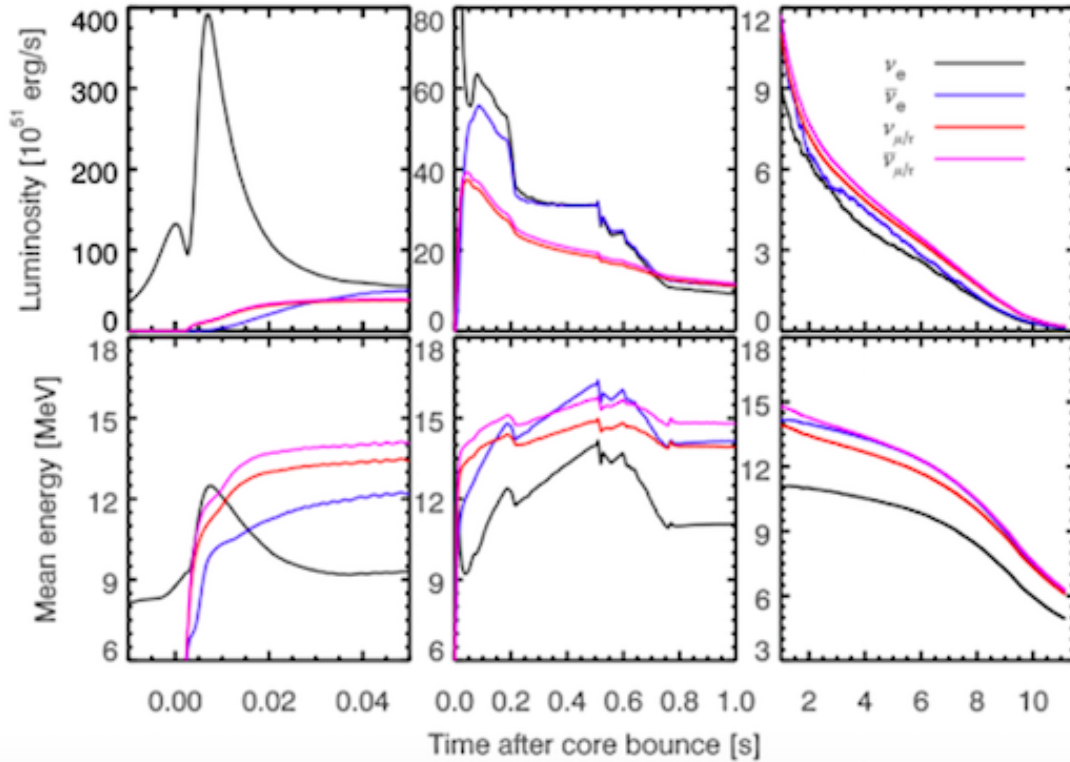


Figure 1.7: Neutrino signal obtained from a simulated supernova explosion. The left panels correspond to the shock break-out phase; the *middle panels* are the post-bounce accretion phase and in the *right panels* is the cooling phase. The *upper panels* represent the neutrino luminosities and the *bottom panels* are the mean energies of the radiated neutrinos.

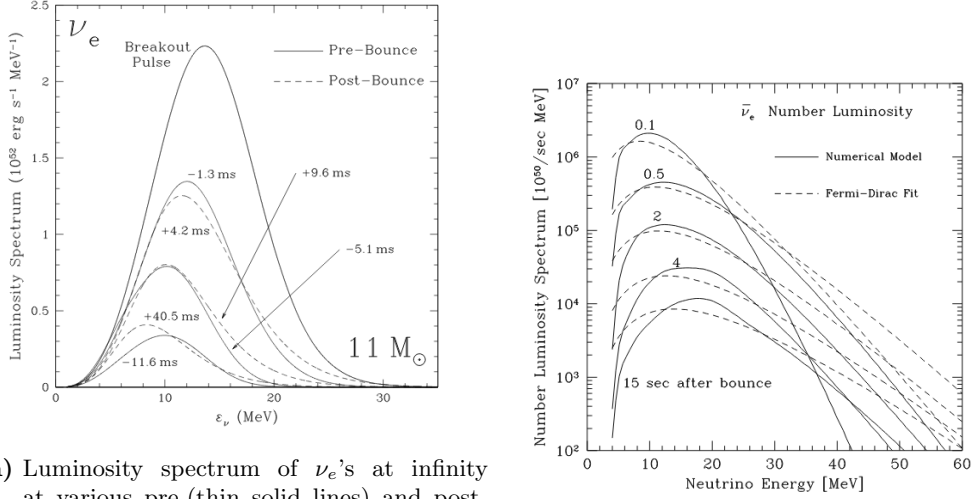
Fig. 1.6 shows the time evolution of neutrino luminosity and average energy obtained, with the numerical model from [33]. Other similar estimates of neutrino luminosity and average energy have been obtained with other numerical simulations. Rough estimates of the time-integrated average energies are:

$$\langle E_{\nu_e} \rangle \approx 10 \text{ MeV}, \quad \langle E_{\bar{\nu}_e} \rangle \approx 15 \text{ MeV}, \quad \langle E_{\nu_x} \rangle \approx 20 \text{ MeV}. \quad (1.15)$$

Fig. 1.8(a) and Fig. 1.8(b) show, respectively, the energy spectra of ν_e 's and $\bar{\nu}_e$'s in the numerical SN models of [34] and [33]. However, we can notice that the model in [34] did not lead to a successful SN explosion. The dashed curves in Fig. 1.8(a) corresponds to Fermi-Dirac approximations with the number distribution

$$\frac{dN}{dE} = \frac{120L}{7\pi^4 T^4} \frac{E^2}{e^{E/T} + 1} \quad (1.16)$$

where $T=180 \zeta(3) \langle E \rangle / 7\pi^4 \simeq \langle E \rangle / 3.1514$ is the effective temperature ($\zeta(3) \simeq 1.20206$ is the Riemann zeta function of 3) and $L = \int_0^\infty dE E dN/dE$ is the total luminosity. In the most numerical simulations the time-integrated luminosities of the different flavor neutrinos are approximately equal. A better fit of the spectra obtained in numerical SN simulations can be achieved adding a pinching parameter η which acts as an effective chemical potential:



(a) Luminosity spectrum of ν_e 's at infinity at various pre- (thin solid lines) and post-breakout (dashed lines) times for a SN with a $11 M_\odot$ progenitor mass. In this figure, time is measured relative to the peak breakout spectrum (thick solid line). The thin solid lines correspond to 11.6, 5.1, and 1.3 ms before the peak and the dashed lines denote the ν_e spectrum 4.2, 9.6, and 40.5 ms after the peak.

(b) Energy spectrum of $\bar{\nu}_e$'s of the numerical supernova model in [33]. The time (after the bounce) is indicated in the figure. The dashed lines are the Fermi-Dirac fits which have the same luminosity and average energy with the numerical model. The chemical potential is set to zero for the FD distribution.

Figure 1.8

$$\frac{dN}{dE} = \frac{L}{F(\eta)T^4} \frac{E^2}{e^{E/(T-\eta)} + 1} \quad (1.17)$$

with $F(\eta) = \int_0^\infty dx x^3 / (e^{x-\eta} + 1)$. In this case, $\langle E \rangle / T \simeq 3.1514 + 0.1250\eta + 0.0429\eta^2 + O(\eta^3)$. Typical values of η are $\eta_{\nu_e} \simeq 2$, $\eta_{\bar{\nu}_e} \simeq 3$, $\eta_{\nu_x} \simeq 1$ [35].

Another widely used parametrization of the neutrinos is:

$$\frac{dN}{dE} = \frac{(1+\beta)^{1+\beta} L}{\Gamma(1+\beta)\bar{E}^2} \left(\frac{E}{\bar{E}}\right)^\beta e^{-(1+\beta)E/\bar{E}} \quad (1.18)$$

where L is the total energy released in neutrinos, \bar{E} is the average neutrino energy, and β is a parameter. The fitting values of \bar{E} , β , and L for the time-integrated $\bar{\nu}_e$ and ν_x spectra in the calculations of [33], are listed in Tab. 1.2, which is reproduced from [27]. One can see that there are significant uncertainties on the value of the average neutrino energy.

In the delayed SN explosion scenario, the stalled shock lies at a radius of about 100-300km, well outside the neutrinosphere. The post-shock temperature is about 1.5 MeV

Ref.	Mass [M_{\odot}]	$\bar{E}_{\bar{\nu}_e}$ [MeV]	\bar{E}_{ν_x} [MeV]	$\beta_{\bar{\nu}_e}$	β_{ν_x}	$L_{\bar{\nu}_e}$ [erg]	L_{ν_x} [erg]
[33]	20	15.4	21.6	3.8	1.8	4.9×10^{52}	5.0×10^{52}
	11	11.4	14.1	3.7	2.2	-	-
[34]	15	11.4	14.1	3.7	2.2	-	-
	20	11.9	14.1	3.7	2.2	-	-

Table 1.2: Fitting parameters of Eq. 1.3 for the time integrated $\bar{\nu}_e$ and ν_x spectra in three different calculations. Table reproduced from [27]. In that reference it is assumed that the models of Ref.[34] $L_{\bar{\nu}_e} = L_{\nu_x} = 5.0 \times 10^{52}$ erg, although such equipartition is not realized in the models, since the models in Ref.[34] do not produce a SN explosion and the total energy released in neutrinos is unknown.

and the density of the order of 10^8gcm^{-3} . The capture of a small fraction, about 5-10 % [36], of the thermal flux of neutrinos emitted from the neutrinosphere could revive a shock, leading to the explosion. The largest energy deposition is due to electron neutrinos and antineutrinos, which have charged-current cross-section on the free-nucleon behind the shock that is larger than the neutral-current cross-section of all neutrino types.

If enough energy is deposited behind the shock, about half a second after the bounce the shock is revived and starts to sweep the outer layers of the star generating the explosion. In recent years several groups have performed multidimensional simulations which resulted in successful, partial explosions and complete failures. The multidimensionality of the simulations is important in order to take into account convection effects that enhance the efficiency of the neutrino energy deposition behind the shock.

While the shock is stalled, matter continues to accrete on the proto-neutron star passing through the shock. During this *accretion-phase* the shocked hot material behind the shock, which is mainly free nucleons, electrons and photons, is heated and produces neutrinos and antineutrinos of all types through Eq. 1.3 and Eq. 1.3. Because the stalled shock is out of the neutrinosphere, these neutrinos can free-stream out of the star and cause the so-called *hump* in the neutrino luminosity curve shown in Fig. 1.6. The average neutrino energy is low during the hump because the dense matter in the shock is opaque to high energy neutrinos. As shown in Fig. 1.6, as the shock gradually revives at about 0.5 s after the bounce, the matter density decreases and the average neutrino energy increases.

Summarizing, in the prompt explosion scenario there are two phases of the neutrino flux: first, a brief and intense burst of prompt electron neutrinos from shock breakout, with a degenerate spectrum of high energy, which is however, so brief that the little energy and lepton number are carried away. Then there is a less intense thermal emission of neutrinos of all flavours, which lasts for a few seconds and carries away most of the binding energy of the neutron star. The total number of emitted neutrinos exceeds by an order of magnitude the original lepton number of the collapsed core.

Whilst, in the delayed explosion, in addition to the prompt electron neutrino burst and

the thermal emission of neutrinos one expects an accretion phase which prolongs the peak of the thermal neutrino luminosity over a time scale of about half a second (*hump*). The delayed explosion scenario is a sort of standard-model of core-collapse SN explosion. Of course, all of these possibilities are still under study.

1.4 SN1987A

On 24 February 1987 a very bright type II SN, identified as SN1987A, was discovered in the Large Magellanic Cloud, which is a satellite galaxy of the Milky Way, at a distance of about 50 Kpc from the solar system [37, 38]. At the time four large underground neutrino detectors potentially sensitive to SN neutrinos were in operation: Kamiokande-II [39, 40], IMB [41, 42, 43], Baksan [44] and LSD [45]. These detectors observed an unusual number of events with energy of the order of 10 MeV within a time window of the order of 10 s in the hours before the optical observation of SN1987A. The events observed in the Kamiokande-II, IMB, and Baksan happened at the same time (within the uncertainties of the absolute time calibration of the detectors and the random occurrence of the events), whereas the LSD events have been recorded about 5 hours before those of the other detectors, at a time when the others did not see anything. For this reason, there is a controversy regarding the LSD data and usually they are not included in the analysis of the SN1987A.

SN1987A is the best studied of all SNe not only due to the detection of its neutrinos but also because, it was the first one visible to the naked eye after the Kepler SN in 1604. It is also, the only SN for which the progenitor star is known: it was a blue supergiant star named Sanduleak -69°202. The evolution of the remnant of SN1987A have been extensively studied in all spectral band, radio, infrared, optical ultraviolet, and x-rays. Although no compact remnant has been identified yet, there is some indication of the presence of a 2.14 ms optical pulsar [46]. The observation of SN1987A neutrinos marked the beginning of *extrasolar system neutrino astronomy*.

1.4.1 Kamiokande-II

After the optical discovery of SN1987A, the Kamiokande-II collaboration examined carefully their data looking for a significant number of events above background in a time interval of the order of 10 s and energy of the order of 10 MeV. They found such a collection of events at 7:35:35 UT of February 1987. Unfortunately, before the discovery of the supernova SN1987A, the Kamiokande-II collaboration did not think that an accurate measurement of the time was needed and the clock of the experiment was set by hand. Because of this, there is an uncertainty of about one minute in the Kamiokande-II determination of the time in which the SN1987A neutrino burst passed the Earth. Electron antineutrino with energy larger than 1.8 MeV can be detected through *inverse beta decay*

reaction:

$$\bar{\nu}_e + p \rightarrow e^+ + n \quad (1.19)$$

with the following cross-section:

$$\sigma_{CC}^{\bar{\nu}_e p} = \frac{2\pi^2}{\tau_n m_e^5 f} E_e p_e \simeq 9.56 \times 10^{-44} \left(\frac{E_e p_e}{\text{MeV}^2} \right) \left(\frac{\tau_n}{886 \text{s}} \right)^{-1} \text{cm}^2 \quad (1.20)$$

where f is the phase space integral :

$$f = \int_{m_e}^{E_0} dE_e \frac{(E_0 - E_e)^2 E_e |\vec{p}_e|}{m_e^5} \quad (1.21)$$

and taking into account Coulomb, radiative and other corrections, the value is [47]:

$$f = 1.71465 \pm 0.00015. \quad (1.22)$$

The produced positron can be detected in water Cherenkov detectors, as in Kamiokande-II. Since it is emitted almost isotropically, the information on the incoming neutrino direction is lost. On the other hand, the energy of the incident $\bar{\nu}_e$ can be measured through :

$$E_\nu = E_e + T_n + m_n - m_p \simeq E_e + 1.293 \text{MeV}, \quad (1.23)$$

where T_n is the negligibly small recoil kinetic energy of the neutron. And the neutrino energy threshold for an IBD process is:

$$E_\nu^{th} = \frac{(m_n + m_e)^2 - m_p^2}{2m_p} \simeq 1.806 \text{MeV} \quad (1.24)$$

The Kamiokande-II detector could observe SN neutrinos also through the elastic scattering reaction as follows:

$$\bar{\nu}_\alpha + e^- \rightarrow \bar{\nu}_\alpha + e^- \quad (1.25)$$

which was used for the solar neutrino detection. However, for SN neutrinos the elastic scattering cross-section is much smaller than the inverse neutron decay cross-section: neglecting m_e and $m_n - m_p$, we have :

$$\sigma_{CC}^{\bar{\nu}_e p} \simeq 9 \times 10^{-44} \frac{E_{\bar{\nu}_e}^2}{\text{MeV}} \text{cm}^2 \quad \text{and} \quad \sigma_{ES}^{\nu_e} \simeq 9 \times 10^{-45} \frac{E_{\nu_e}}{\text{MeV}} \text{cm}^2 \quad (1.26)$$

Tab. 1.3 shows the main characteristics of the 16 events measured in the Kamiokande-II detector during the SN1987A burst. It is important to keep in mind that is unlikely to know with certainty which events have been really produced by neutrinos coming from the SN1987A and which events are due to background. Therefore in Tab. 1.3 we can see all the known events, taken from [40, 48], even those that are likely to be background events and were excluded from statistical analysis of all kind, apart from the analysis in [48], in which background effects were taken into account. For each event the background rate $B(E_e)$

Event	Time t s	Kamiokande				
		Energy E_e MeV	Angle θ_e degrees	$B(E_e)$ [48] s^{-1}	P_B [48] (prompt)	P_B [48] (delayed)
1	0	20.0±2.9	18±18	1.6×10^{-5}	5.8×10^{-5}	2.4×10^{-5}
2	0.107	13.5±3.2	40±27	1.9×10^{-3}	6.3×10^{-3}	1.9×10^{-3}
3	0.303	7.5±2.0	108±32	2.9×10^{-2}	0.16	4.7×10^{-2}
4	0.324	9.2±2.7	70±30	1.2×10^{-2}	5.4×10^{-2}	1.7×10^{-2}
5	0.507	12.8±2.9	135±23	2.1×10^{-3}	7.6×10^{-3}	3.2×10^{-3}
6	0.686	6.3±1.7	68±77	3.7×10^{-2}	0.25	0.15
7	1.541	35.4±8.0	32±16	4.5×10^{-5}	1.2×10^{-3}	1.5×10^{-3}
8	1.728	21.0±4.2	30±18	8.2×10^{-5}	5.7×10^{-4}	1.0×10^{-3}
9	1.915	19.8±3.2	38±22	1.5×10^{-5}	9.9×10^{-5}	1.9×10^{-4}
10	9.219	8.6±2.7	122±30	1.5×10^{-2}	0.33	0.49
11	10.433	13.0±2.6	49±26	1.9×10^{-3}	0.11	0.12
12	12.439	8.9±1.9	91±39	1.6×10^{-2}	0.54	0.60
13	17.641	6.5±1.6	?	3.8×10^{-2}	0.92	0.89
14	20.257	5.4±1.4	?	2.9×10^{-2}	0.97	0.94
15	21.355	4.6±1.3	?	2.8×10^{-2}	0.97	0.93
16	23.814	6.5±1.6	?	3.8×10^{-2}	0.99	0.94

Table 1.3: Time t, energy E_e , and angle θ_e with respect to the direction opposite to SN1987A of the Kamiokande-II events [40, 48]. $B(E_e)$, P_B (prompt), and P_B (delayed) are, respectively, the event background rate and the probability that the event is due to background in the best-fit prompt and delayed supernova explosion models calculated in [48]. The event number 6 is reported in the original Kamiokande-II publication [40], but it is excluded in their signal analysis because of a low number of hit photomultipliers. While the events 13-16 were originally excluded in the analysis, they are considered in [48], because background effects are taken into accounts.

is also listed, calculated in the above reference, which depends on the event energy E_e , and the probabilities P_B (prompt) and P_B (delayed) that the event is due to background according to the best fit prompt and delayed supernova explosion models calculated in [48] See Section 1.3.

The number 6 events is reported in the original Kamiokande-II publication [40], but it is excluded in their signal rate because of a low number of hit photomultipliers, which implies a high probability that it could be a background event. The events number 13-16 are not in the original publication, but they are reported in [48]. Even if these events have a high probability to be background events, the probability that at least one of them is signal is not negligible and it is correct to include them in data analysis as done in [48]. The angles of the events 13-16 are not included in the analysis thou, since it has been assumed they can be background events or they can come from inverse beta decay Eq. 1.19, in which the positron is emitted almost isotropically. This assumption is acceptable because of the

Event	Time t s	IMB	
		Energy E_e MeV	Angle θ_e degrees
1	0	38 ± 7	80 ± 10
2	0.412	37 ± 7	44 ± 15
3	0.650	28 ± 6	56 ± 20
4	1.141	39 ± 7	65 ± 20
5	1.562	36 ± 9	33 ± 15
6	2.684	36 ± 6	52 ± 10
7	5.010	19 ± 5	42 ± 20
8	5.582	22 ± 5	104 ± 20

Table 1.4: IMB supernova SN1987A events from [42]

- . The time of each event is relative to the first one, which occurred at 7:35:41.37 UT of 23 February 1987. There is an additional systematic uncertainty in the energy scale estimated to be about 10%. The background rate is negligible.

dominance of the cross-section of the inverse beta decay (see Eq. 1.26)

1.4.2 IMB

THE IMB (Irvine-Michigan-Brookhaven) detector was a 24 m *times* 18 m \times 19 m tank filled with about 8000 ton of water. The fiducial mass was about 3300 tons. It was located deep underground in the Morton Thiokol salt mine near Cleveland, Ohio (USA), at a depth of 610 m, with an overburden of 1570 m.w.e. On 23 February 1987 the IMB detector recorded eight neutrino-produced events with energies between 20 and 40 MeV in a time interval of 6 s starting from 7:35:41.37 UT (the clock had an absolute uncertainty of 50 msec and a relative uncertainty of 0.5 msec). The background rate is negligible, about two per day in the range of 20-2000 MeV.

The important characteristics of eight IMB events are listed in Tab. 1.4. Since these events are most likely due to inverse beta decay process given by Eq. 1.19, the neutrino energy is given by Eq. 1.23. Taking into account the trigger efficiency and about 13% dead time of the detector, the IMB collaboration estimated that 35 ± 15 neutrino events with energy above 20 MeV occurred in the detector [42].

1.4.3 Baksan

The Baksan Underground Scintillation Telescope [44] is located in the Baksan neutrino Observatory at a depth of 850 m.w.e in the Baksan Valley in North Caucasus, Russia. The telescope consists of 3150 parallelepipedal tanks filled with oil-based liquid scintillator viewed by a 15 cm photomultiplier. The energy threshold for SN neutrinos is about 10 MeV. The total target mass is about 330 tons. The background, mainly caused by cosmic ray muons and discharges in the photomultipliers, is relatively large. So, only 1200 inner

Event	Time t s	Energy E_e MeV	Baksan		
			$B(E_e)$ [48] s^{-1}	P_B [48] (prompt)	P_B [48] (delayed)
1	0	12.0±2.4	8.4×10^{-4}	2.1×10^{-2}	4.9×10^{-3}
2	0.435	17.9±3.6	1.3×10^{-3}	3.6×10^{-2}	1.9×10^{-2}
3	1.710	23.5±4.7	1.3×10^{-3}	7.4×10^{-2}	0.12
4	7.687	17.6±3.5	1.3×10^{-3}	0.30	0.35
5	9.099	20.3±4.1	1.3×10^{-3}	0.55	0.52

Table 1.5: Time t , Energy E_e and angle θ_e , with the respect of the opposite to SN1987A of the Baksan events [48], $B(E_e)$, P_B (prompt) and P_B (delayed) are respectively, the event rate and the probability that the event is due to background in the best-fit prompt and delayed supernova explosion models in Ref.[48].

tanks with lower background and a mass of about 130 ton are used as signal triggers, and the inner tanks plus part of the external tanks are used as fiducial volume, with a mass of about 200 tons. Due to its characteristics, the detector is mainly sensitive to electron antineutrinos which interact with free proton through the *inverse beta decay* reaction seen in Eq. 1.19.

The Baksan collaboration could not claim an independent observation of SN1987A neutrinos, due to background. Afterwards, with the informations provided by the Kamiokande-II and the IMB collaborations, Baksan collaboration could identify 5 events in 10 seconds that could overlap with the data of the above experiments, with the uncertainty of ${}_{-54}^{+2}$ s in the absolute clock measurements.

The main characteristics of the five Baksan events are reported in Tab. 1.5, where one can see that the background rate is particularly high. For this reason most analysis do not include these events in data analysis. Although in [48] background rate has been taken into account and was proven that Baksan events are compatible with SN signal.

1.4.4 Comparison with supernova theory

Many authors agree that the detected neutrino events are compatible with the general scenario of the core-collapse SN explosion described in Section 1.3. In the accurate analysis of [48] it was found that models of supernova explosion with the delayed mechanism explained in Section 1.3 are about 100 times more probable than prompt explosion models. The electron antineutrino average energy is about 15 MeV, as expected from the cooling of the proto-neutron star (see Eq. 1.15). The cooling time scale is about 4 s, and the time scale of the accretion component is about 0.7 s, in agreement with numerical calculations. The total inferred number of electron antineutrinos emitted is about 3×10^{57} , implying a binding energy of the neutron star of about 3×10^{53} erg, as expected from simple calculation (see Section 1.3). Unfortunately the SN1987A neutrino data are too sparse to obtain more detailed information on the SN mechanism.

1.5 Neutrino mixing

Since neutrinos are mixed, an electron neutrino does not have a definite mass, but is a superposition of different massive neutrinos. In this case, m_{ν_e} must be considered as an effective electron neutrino mass, which represents the masses of the massive neutrinos which have a substantial mixing with ν_e .

In the three-neutrino mixing scenario, ν_e has large mixing only with ν_1 and ν_2 . However, since the squared-mass differences are very small, the kinematical upper limit for the ν_e applies to all the three neutrino masses, so to have:

$$m_k \leq 30\text{eV} \quad (\text{model} - \text{independent}) \quad (1.27)$$

$$m_k < 5.7\text{eV} \quad (95\% \text{ CL}) \quad [48] \quad (1.28)$$

con $k=1,2,3$.

It is, however, still possible that the electron antineutrino has a small mixing with one or more heavy massive neutrinos. The interaction probability of a heavy massive neutrino ν_h is proportional to $|U_{eh}^2|$, where this is the element of the lepton mixing matrix connecting the electron neutrino to the heavy neutrino. Since $|U_{eh}^2|$ is small, the SN1987A Kamiokande-II and Baksan data do not place any constraint on m_h , due to their relatively high background and a weakly interacting heavy massive neutrino arriving on Earth is indistinguishable from the background. On the other side, the IMB detector had a negligible background and there were not found any neutrino events in the 3.9 hours after the SN1987A neutrino burst.

From the results of the CHOOZ long-baseline reactor oscillation experiment, we know that the mixing of ν_e with heavy neutrino ν_h is small. In fact the effective mixing angle for two-neutrino $\bar{\nu}_e \rightarrow \bar{\nu}_h$ oscillations is:

$$\sin^2 2\theta_{eh}^{eff} = 4|U_{eh}|^2(1 - |U_{eh}|^2) \quad (1.29)$$

and from the limit set by the CHOOZ experiment given by:

$$\sin^2 2\theta \leq 0.1 \quad \text{for} \quad \Delta m^2 \geq 2 \times 10^{-3}\text{eV} \quad (1.30)$$

implies that

$$|U_{eh}|^2 \leq 2.6 \times 10^{-2} \quad (90\% \text{ CL}) \quad (1.31)$$

If the absolute value of the reactor $\bar{\nu}_e$ flux is considered to be uncertain, the spectral distribution of CHOOZ data do not put any limit on the mixing, of ν_e with a heavy neutrino ν_h .

Since the Kamiokande-II SN1987A events appear to be clustered in two groups separated by a time interval of roughly 10 s, some have claimed that there is evidence of two mass groupings at 4 eV and 22 eV [49]. To make this assertion, it has to be assumed that electron neutrinos are emitted from the SN in a very short time, of the order of 0.1s.

This contradicts our knowledge of the core-collapse SN mechanism, according to which the electron antineutrinos are emitted during the cooling phase of the proto-neutron star, which means on a time scale of the order of 10s (see Section 1.3). Moreover, the existence of neutrinos with masses of 4 eV and 22 eV, with large mixing with the electron antineutrino is excluded by the tritium upper bound on the effective electron antineutrino mass. Other informations were gathered on neutrino mixing from the SN1987A data considering the effect of vacuum, oscillations or MSW effect on the fluxes of different flavors. Large $\bar{\nu}_x \leftrightarrow \bar{\nu}_e$ transitions are disfavored, because they would imply a spectrum of $\bar{\nu}_e$'s on Earth which is more energetic than the one observed.

1.6 Future

Several detectors sensitive to SN neutrinos are currently in operation and in preparation. Current and future SN neutrino detectors are much larger than the detectors in operation during 1987. The order of magnitude of the number of expected events when the next galactic SN will explode is 10^4 . Such a high rate of events will be precious for the understanding of SN physics and improve our knowledge on neutrino properties. In this work we will look and try to have a better understanding of the potential of detecting the next SN neutrino signal with the JUNO detector, under construction in China, which is suppose to start taking data in 2022.

Chapter 2

The JUNO experiment

The Jiangmen Underground Neutrino Observatory (JUNO) is set to be the first next-generation detector with a target mass of 20 kton. It is a multi-purpose underground neutrino experiment, proposed in 2008 with the main physics goal of the determination of the neutrino mass hierarchy. As the name suggests, it is located close to *Kaiping*, which is part of the prefecture-level city *Jiangmen* in Southern China. JUNO although is also capable of observing neutrinos from terrestrial and extra-terrestrial sources, including supernova burst neutrinos, diffuse supernova neutrino background, geo-neutrinos, atmospheric neutrinos, solar neutrinos, as well as exotic searches, such as nucleon decays, dark matter and sterile neutrinos. The neutrino detector consists of a 20 kton fiducial

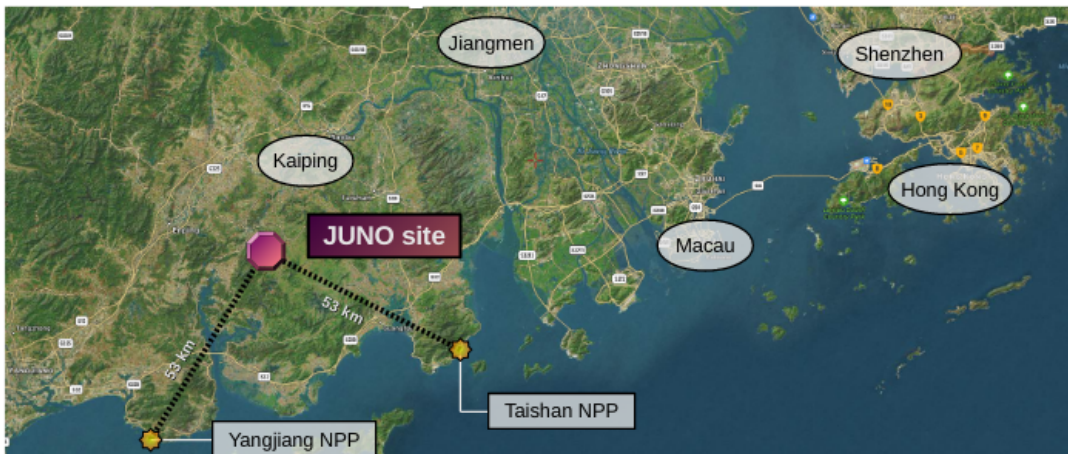


Figure 2.1: Location of the JUNO site, together with the main urban centers of Daya Bay complex.

mass liquid scintillator (LS), deployed in a laboratory 650 meter underground, where anti-neutrinos produced in the nuclear power plants can interact via inverse beta-decay (IBD), producing a positron and a neutron in the final state: $\bar{\nu}_e + p \rightarrow e^+ + n$. The positron loses its kinetic energy in a short length and then annihilates with an electron: the sum of these two processes generates a *prompt* signal within few ns. With a time delay of a

few hundred of μs the neutron will be captured by a proton in the LS and will produce a *delayed* signal of 2.2 MeV.

The scintillation light from those secondary particles is collected by a dual-system of photosensors installed on a spherical structure with a radius of about 20m. Photomultipliers (PMTs) are submerged in a liquid buffer to protect the LS from the radioactivity of the PMT's glass.

2.1 Experimental Site

JUNO is designed as a reactor anti-neutrino experiment, which of course, affects its requirements and its location. The experimental site was chosen in order to achieve the best sensitivity to the neutrino mass hierarchy and it is located 53 km from both *Yiangjiang* and *Taishan* nuclear power plants. The *Yiangjiang* NPP will operate at a thermal power of 2.9 GW each when JUNO starts data taking. On top of that there will be at least two 4.59 GW cores working in the *Taishan* NPP at the same time and two more cores of equal power will be finished later in time. Therefore, the total thermal power will amount to $\sim 36GW_{th}$ available when JUNO starts [50].

A second crucial requirement for JUNO is the achievable *overburden*, to shield the detector from cosmic backgrounds. It will account for a total overburden of 650 m or ~ 2000 w.m.e. [50]. The access to the laboratory will be guaranteed by two tunnels, a vertical shaft going straight down and an inclined slope tunnel, 1340 m long. Facilities of the underground laboratory include LS halls, which house the purification systems and OSIRIS, that is the only system to test the nominal operation of the purification plants and will guarantee that the concentrations of U and Th in the LS do not exceed the given limits, as well as the storage areas and the main detector hall.

The surface facilities, shown in Fig. 2.2, are mainly storage and assembly halls, but also include the first level of data processing and transfer.

2.2 Detector Systems

In its role of a neutrino observatory, JUNO does not only consist of one single detector, but several sub-systems, that are designed to interact according to their individual strengths. Nevertheless, the heart of the experiment is the Central Detector (CD) with 20 kt LS as a neutrino target. This volume is contained in a spherical acrylic vessel with a 12 cm thickness and a diameter of 34.4 m. It is enclosed in a *Stainless Steel Truss* (SST), that holds the sphere into place. With a diameter of 40 m, the SST is also the holding frame for two independent photo-multiplier (PMT) arrays for light detection. Details on the chosen LS mixture and the PMTs are given in Section 2.2.1 and Section 2.2.3 respectively.

The CD is placed in a large, cylindrical *Water Pool* (WP), that acts as shield against external radioactivity. In addition to that, it is instrumented with PMTs to act as a water Cherenkov detector for muon veto purposes. On top of the WP, there will be a plastic



Figure 2.2: Surface facilities at the JUNO site include storage and assembly halls as well as accommodation site for workers

scintillator tracker, to measure external radioactivity and the cosmic muon flux. Both systems are presented in Section 2.2.4 in more details. Section 2.2.5 introduces OSIRIS, which is a fully functional smaller LS detector on its own. It will be placed within the filling line of the CD to monitor the cleanliness of the LS after purification. Over the course of at least 6 months, the CD will then be filled with its LS mixture. With such a large target mass, it is imperative not to spoil the total LS in the CD with a single batch of contaminated LS.

Finally in Section 2.2.6, the TAO detector, the JUNO satellite experiment, will be described.

2.2.1 Liquid Scintillator

The unprecedented size of the CD introduces several challenges in particularly for the LS. For good data quality is essential that a vast amount of light can travel through the 40 m vessel and be detected by the PMTs systems without being absorbed or being scattered.

With the newly progress in increasing the attenuation length of commonly used LS, despite JUNO shape and size, it is possible to have 20 m of attenuation length necessary to detect direct scintillation light.

Another aspect to take under consideration is the light yield. JUNO physics goals rely on a very high energy resolution, so up to roughly 10000 photons per MeV of light yield. Combining this with the PMTs systems, a total of ~ 1300 detected *photo-electrons* (PE)

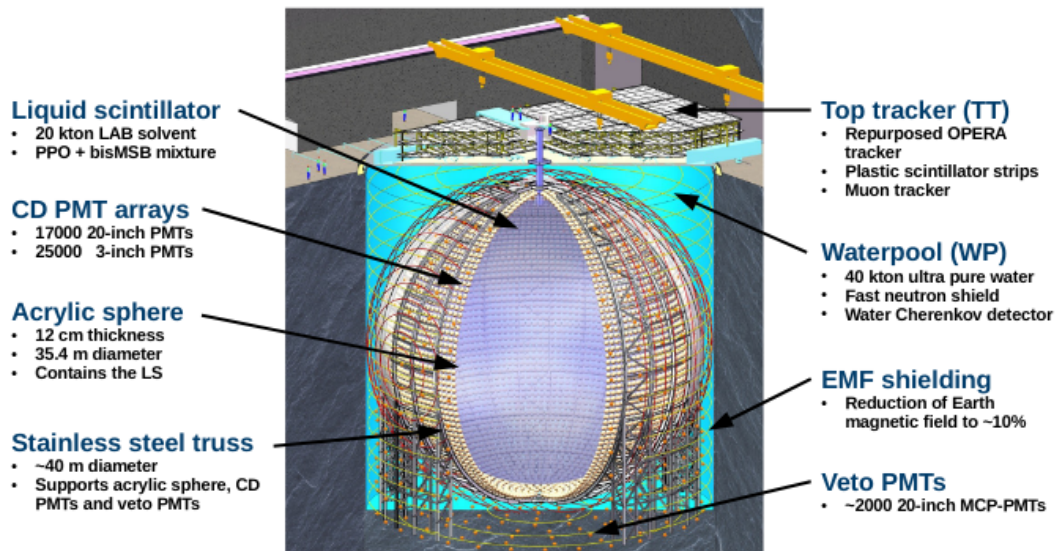


Figure 2.3: Main detector hall of JUNO

per MeV deposited energy, can be achieved.

JUNO will employ LAB for its LS mixture. It will serve as a solvent for a two component system of scintillating fluorine and wavelength shifter. The primary chosen fluorine is PPO, while the the wavelength shifter is Bis-MSB. With this mixture, the excitation of an ionizing particle is transferred to the PPO and shifted by the Bis-MSB to a wavelength of 430 nm. A higher concentration of PPO and Bis-MSB will increase the light yield, but there will be a bigger chance of self-absorption, and this will decrease the attenuation length.

Accurate studies and testing on the LS have been done to make sure the right balance between light yield and attenuation length was achieved. At the moment the reported attenuation length is reported to be > 25 m, while maintaining the needed light yield level.

The light production in the LS depends on the ionization density and it depends on the particle type. It is therefore expected to measure different responses for α particles, protons or neutrons and gamma, electrons and positrons in the mixture of PPO and Bis-MSB. There is another element to be taken into account, which is the LS internal radioactivity. The LS is an organic scintillator, and this implies the natural occurrence of uranium, thorium, and potassium in it. Along with their natural decay chains, those isotopes produce decays in sensitive energy range causing a background for the JUNO's proposed measurements. On top of that traces of ^{210}Bi , ^{210}Po and ^{85}Kr can be found. While the energy spectrum is fixed, the rate is proportional to the abundances of the isotopes. All this contamination can be reduced with the purification of the LS.

For the purification process JUNO has a sophisticated purification plant in place. It involves a Al_2O_3 column, distillation, water extraction and stream stripping stages in order

to fulfill the requirements on the LS. A review of the subsystem can be found in [51] Also as an organic substance the LS contains a high natural abundance of ^{14}C . This isotopes has a β^- decay with an endpoint at 156 keV. Currently there is not artificial way (e.g. purification) to reduce the amount of ^{14}C .

2.2.2 Stainless Steel Truss

It is a spherical, single-layer truss made of I-shaped components, arranged both in longitudinal and latitudinal directions. The truss is supported by pillars at the base of the Water Pool. In order to avoid any torsion in the structure, a ring of bracing is added in the truss grid.

In addition, due to the spherical shape, the square shaped structure has been replaced by triangle shaped one at the top, so to reduce the number of the truss members.

2.2.3 Photo-multiplier tubes

The next key elements of the detector are its PMTs systems. One of JUNO's main requirements is its unprecedented energy resolution, for which it requires a high photon statistics. In order to achieve this, the CD is instrumented with two independent PMTs systems, that combined supply coverage of 77.5%. The main modules for the coverage are large PMTs (LPMT) with 20 inch diameter, then there is an additional system of small PMTs (SPMT) with 3 inch diameter in place. Both are complementary and work in favour of the other.

LPMT The LPMT array in the CD is made up of about 18000 modules kept at a distance of $r=20$ m from the detector center. About 5000 of them are conventional dynode PMTs by *Hamamatsu* (R12860-HQE), while the rest 12000 modules are developed by MCP-PMTs by NNVT in China. Together they account for a coverage of 75%. Of course there are strict conditions on the PMTs performance. The most important one is the photon detection efficiency, that has to be at least $> 24\%$ at 420 nm for an individual PMT, but $> 27\%$ averaged over the array. An aspect to keep under control is the dark rate count, which has to be less than 100 kHz for the MCP-PMTs and below 50 kHz for the dynodes PMTs. Each individual high voltage supply will be calibrated with a gain of 10^7 . The resolution of photon hit times is defined by the PMTs TTS and it differs between the MCP and the dynode PMTs. The first ones satisfies a TTS of better than 12 ns(FWHM), while the latter are able to achieve 3.5 ns.

SPMT The SPMT system is an independent readout system made of 25000 PMTs by HZC. The size of these modules contributes only to the 2.5% to the total coverage. Their small size has a bigger upside, which is allowing them to work in a single *photon-counting* mode for events below 10 MeV, which is JUNO's focus. The Small photo-multiplier will be installed in between the Large ones and they are thought to provide a second set of eyes



Figure 2.4: Photograph of the two kind of PMTs that will be installed inside JUNO CD. The *Hamamatsu* dynode PMT(left) and the NNTV MCP-PMT (right)

with different systematic from the LPMT. While the 20 inch PMTs are new developments and need more characterization, small PMTs do not get affected by the effects from the utter size. In addition performing double calorimetry measurement can help to reduce systematic errors from the LPMT system. The specifics are a TTS smaller than 5 ns and an average quantum efficiency of 24% with a dark count rate lower than 1.8 kHz.

2.2.4 Shielding and veto systems

The CD is designed to be highly sensitive to a small energy deposition, and nonetheless is affected by natural radioactivity and cosmic rays. To assure the optimal sensitivity to the neutrino mass hierarchy, a strategic distance and position for the JUNO detector has been chosen to maximize the effect of the oscillation effects; for this very reason it has the same distance from all the reactors of both Nuclear Power Plants. In addition JUNO is located underground with a total of ~ 650 m of total rock overburden.

WaterPool A large cylindrical waterpool (WP) is added as an additional layer of shielding, which surrounds the CD. It has a 43.5 m diameter and a total height of 44 m and it will provide a minimum of 2 m of water between the rock wall and the CD at the closest area. The cylindrical tank is filled with ~ 20 kton of ultrapure water. (Fig. 2.3). Since the SST, that holds the PMTs, is a frame rather than a tank, the space between the acrylic vessel and the PMT array is also filled by water. Typically this area is called *buffer* and it is necessary to shield the LS from the radioactivity brought by the PMT's glass. Therefore the ultra pure water; impurities can compromise the shielding effect by introducing radioactive elements to the PMT's and vessel.

Finally, the WP is instrumented with 2400 MCP-PMTs to upgrade it from a pure shielding to an active water Cherenkov detector designed to identify and veto cosmic muons with high efficiency, arranged on the windows of the spherical SST frame and facing outward (Fig. 2.5).

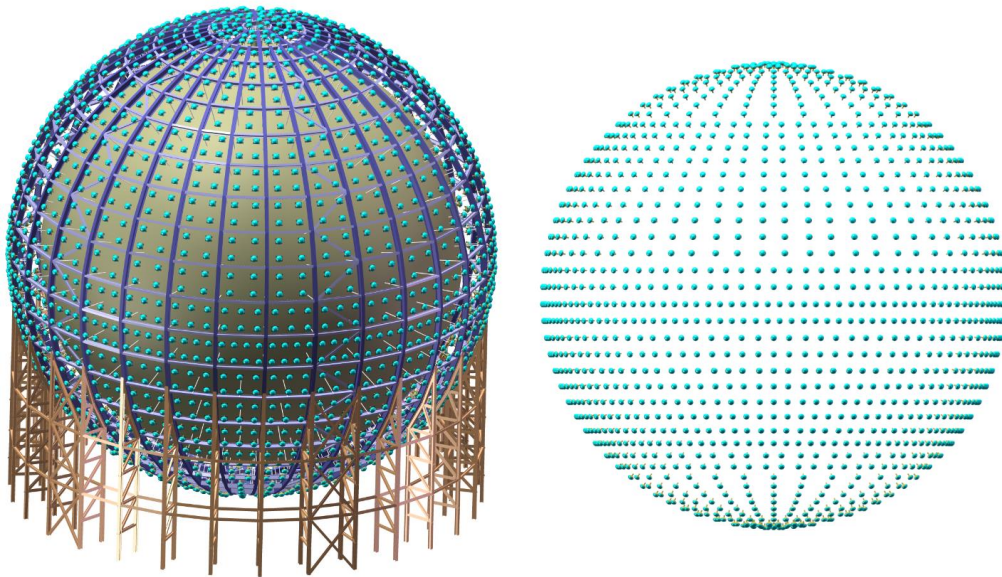


Figure 2.5: Schematic of the WP LPMTs arrangement on the SST (left) and alone (right). The PMTs are denser in the lower region of the detector, after optimization studies within the collaboration. Figures from [52].

A good knowledge of the muon's flux and their tracks' positions is essential, since their background contribution is multiple.

Top Tracker The Top tracker (TT) of JUNO will utilize the decommissioned target tracker of the *Oscillation Project with Emulsion Tracking Apparatus* (OPERA) [53], in order to also improve the reconstruction of cosmic muons directions. The well reconstructed muons are very important in the veto strategy for rejecting cosmogenic isotope background. Combining the muon information from the Top Tracker and the Water Cherenkov detector, most of the atmospheric muon-induced background can be removed. To detect their passage it will use plastic scintillator strips with multichannel PMT readout. In total there will be 63 so-called walls with a sensitive area of $6.7 \times 6.7 \text{ m}^2$ each. The walls are arranged in a 7×3 grid in 3 layers covering about 60% of the top surface above the WP as it is shown in Fig.2.6.

The wall in the middle of each layer is moved up in relation to the other layers to make space for the CD chimney, as shown in the left panel of Fig. 2.7.

Each wall is composed by 8 modules placed on two planes that are perpendicular to each other. One module contains 64 scintillator strips, which are read at both ends by two 64-channel multi-anode photo-multiplier tubes. The schematic view of a wall is shown in the right hand panel of Fig. 2.7. To adapt the walls for the TT, in JUNO, new mechanical structure must be added and electronics is redesigned from the OPERA's. This configuration allows the TT to detect muons hits with a spatial resolution of $2.6 \text{ cm} \times 2.6 \text{ cm} \times 1 \text{ cm}$ and reconstruct tracks with a median angular resolution of 0.20° . The TT strips have been produced by extrusion, with a T_iO_2 co-extruded reflective and diffusive coating for better light collection. Lastly, the TT can detect some muons that cross neither the CD nor the WP, but produce fast neutron background in the surrounding rock, so it can be

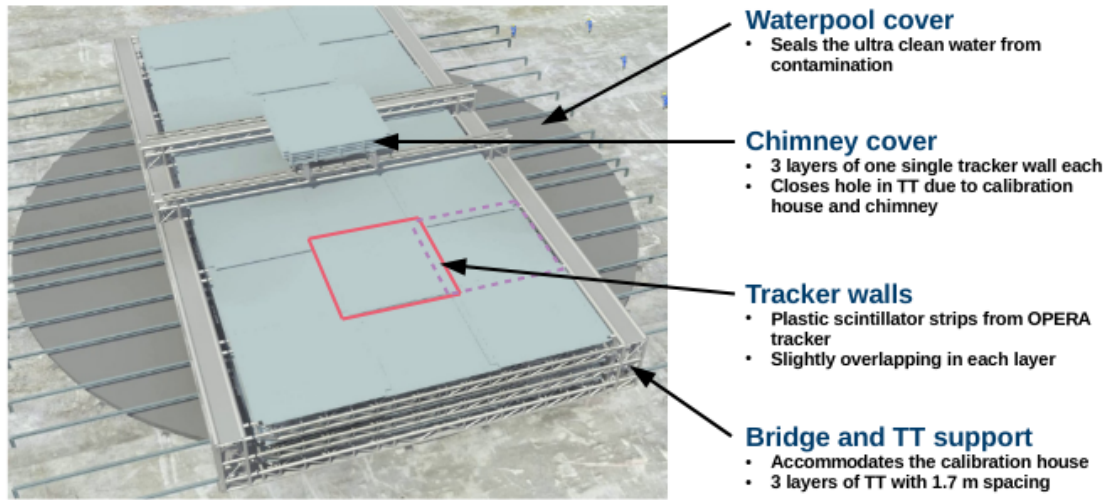


Figure 2.6: Schematic of the bridge over the WP. It will accommodate the TT holding structure as well as the calibration house, which gives access to the chimney into the CD.

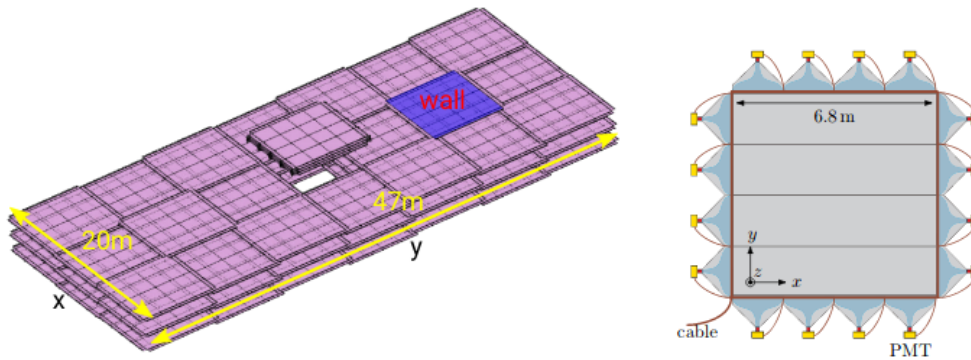


Figure 2.7: Left:schematic view of the TT. Right:schematic view of a TT wall

used to collect a sample of well-reconstructed muon tracks, which can be used to calibrate the reconstruction algorithm for the CD.

2.2.5 OSIRIS

As mentioned before, a crucial aspect for JUNO's success is the radiopurity of its LS. The *Online Scintillator Internal Radioactivity Investigation System* (OSIRIS) is a stand-alone 20-ton pre-detector currently under development to ensure the purity of the LS. It will be installed in the underground lab in the filling line close to the CD. It will act as an independent radiopurity test facility, that will monitor the nominal operation of the purification plants. In addition since it will be taking data during the filling of the CD, it will also give the possibility to act as a test for some JUNO subsystems.

The detector's central part will be a transparent acrylic vessel (AV), exactly like Borexino CTF design [54], and will be able to hold a batch of 21 m^3 of LS. Despite Borexino CTF, the AV of OSIRIS will have a cylindrical shape similar to *DAYA BAY*, with a wall strength of 3-4 cm. It is placed on a pedestal that consists of an acrylic footing and a mechanical support structure made of stainless steel.

There is a PMTs'array of 76 *Hamamatsu* 20-inch PMTs on a stainless steel frame to collect the light in the LS. While four PMTs are placed in a ring on the bottom and at the top, cylinder mantle is covered by five rings of 16 modules each, with a coverage of $\sim 13.4\%$ and $\sim 5-6\%$ at 1 MeV energy resolution. They are placed so that the photocathodes are about 1 m distance from the AV, and the space between the PMTs and the AV is filled by water to act as a shield, similar to the CD of JUNO. This layer of volume extends for another 2 m beyond the array to also shield the detector from the surrounding rock in the lab. The entire volume is contained by a cylindrical steel tank with both 9 m diameter and height. In the same line of JUNO, the water shield will be instrumented with a secondary PMTs'array.

2.2.6 TAO

The *Taishan Antineutrino Observatory* (TAO) [55] will be an additional standalone detector alongside JUNO to produce a high resolution reference spectrum for the electron anti-neutrinos coming from one of the reactors in the Taishan NPP. Modeling the reactor spectrum precisely can be very difficult. In order to keep in check all the variables affecting the good result of the measure in the context of the MO definition for JUNO, a reference spectrum with the same or better resolution is needed [56].

In order to achieve this, TAO is design to give a model-independent reactor antineutrino-spectrum. It will be a Gadolinium-*doped* liquid scintillator (GdLS), hold in a spherical vessel with ~ 90 cm radius, filled with 2.8 ton of GdLS, located very close, ~ 30 m to the above mentioned reactor core.

Photon detection is going to be realized with the use of 10^2 m^2 of *silicon photon-multipliers* (SiPM) with a detection efficiency of 50%, with a light yield of 4500/MeV, corresponding to a energy resolution better than $2\%/\sqrt{E[MeV]}$. The entire system is going to operate at $-50^\circ C$ to reduce the dark noise contribution from the SiPMs. Water Cherenkov and plastic scintillators will also act as a veto for cosmic muons and shield for external radioactivity. Considering the detection efficiency of the coincidence signal, a rate of 2000 IBD events per day is to be expected. The detector is under development and details can change. It is expected to start taking data in 2022.

2.2.7 DAQ and Trigger strategy

The JUNO readout system has to deal with the acquisition of signals from more than 20.000 LPMTs (CD+WP) plus 25.000 SPMTs. The events need to be recorded over the

entire range, ensuring minimum data loss. The trigger plays a special role in selecting events from the great amount of random dark noise recorded by the PMTs. The electronic system must have an excellent resolution over energy and time, with a negligible dead time for high event rate such as Supernova explosions.

In regards to the CD, the electronic system is designed to provide a full LPMTs digitization, with a high speed (1 Gsample/s) and a high resolution ADC (12 bits). At the same time it provides the sampling over the full dynamic range, from 1 up to 4000 NPEs. The SPMTs, on the other side do not require a full waveform acquisition, since they operate primarily in a photon-counting mode.

Both LPMTs and PMTs front-end electronics are placed underwater, into dedicated boxes. Each box will have a Global Control Unit (GCU). For LPMTs, a single box will acquire the signals coming from 3 PMTs (a design also valid for the WP), while for SPMTs a box will acquire 128 signals coming from SPMTs. The output of the GCU is transferred out of water via an asynchronous link to the DAQ system and via a synchronous link to the trigger system, where the information of all the LPMTs are combined to form a global trigger decision. A time acquisition window of $1.2 \mu\text{s}$ is foreseen. More details on the PMTs electronics is in [57]. A global trigger scheme will merge all the information from all the LPMTs. SPMTs and TT feature an independent acquisition system. At the current stage, a majority trigger of LPMTs is planned: if the number of fired PMTs exceeds 350 in a 300 ns time window, the event is recorded in a $1.2 \mu\text{s}$ window. The 350 fired PMTs correspond to roughly 350 KeV of deposited energy.

According to the time and NPE pattern, a fast reconstruction of the event is performed online, for what concerns the estimation of the deposited energy and the interaction vertex. The events are so classified online, so to perform a higher-level selection on the event flow. The raw data are then stored locally in a dedicated farm and then transferred to the IHEP Beijing Computing Centre. The JUNO computing model includes a full mirroring of raw data into some European sites.

CCSNe real monitor The real-time monitor of CCSNe at the DAQ stage is designed to work with the online reconstructed events from multiple sub-detectors of JUNO to check if there are any neutrinos from CCSN, i.e. pre-SN neutrinos and SN burst neutrinos. Once there is a CCSN, the monitor will send out alerts to the data flow manager of DAQ to record as much original data as possible.

Fig. 2.8 shows the data flows (green light) from different sub-detectors to CCSN Monitor at the DAQ stage. In this stage, the filtered events with timestamp, energy, vertex and muon track in central detector (CD) and the muon-tagged events with (Q,T) of fired LPMTs of Water Cherenkov detector (WP) are required by the *CCSN Monitor*, which can be obtained with the trigger-less (T,Q,W) data from the CD LPMTs and the triggered waveforms from WP.

The data stream from CD, WP and TT will be collected into the *Readout Nodes* at

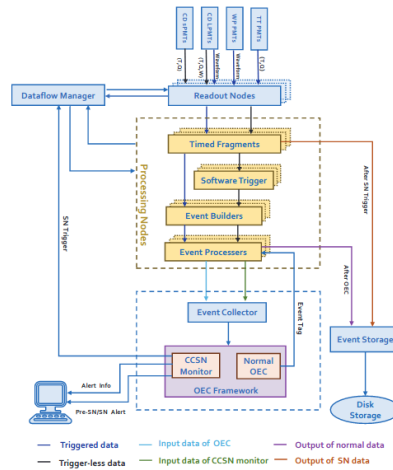


Figure 2.8: The real time monitor for CCSNe at the DAQ stage.

the DAQ stage, as shown in Fig. 2.8. Both the global triggered waveforms and trigger-less (T,Q,W) of CD LPMTs could be read out into the DAQ servers in a time-sharing way, thanks to the 2 GB DDR3 embedded into the GCU [58]. The event rate from the global trigger could be kept below an upper limit, e.g. 1 kHz. The (T,Q,W) extraction from the PMT signal could be realized in real time with the algorithm embedded in the FPGA of the GCU, where "T,Q,W" refers to the timestamp, the integral charge and the width of the PMT waveform above S.P.E threshold, respectively. The width "W" parameter is helpful to employ an offline correction to reduce the energy "non-linearity". At present, 10 bytes are afforded to record (T,W,Q) of one PMT hit, of which 30 bits is for T(time), 22 bits for Q(charge), 8 bits for W(width) and 15 bits for PMT channel ID.

Chapter 3

Software Framework and Data

A software framework for data processing and analysis is a substantial part for the development of a new experiment. The output of the data acquisition (DAQ) after event building are collections of either *waveforms* or hit times and charge, depending on the DAQ design. Low level reconstruction algorithms are necessary to process raw data and determine actual physical events from them.

JUNO implemented a framework called *Software for Non-collider Physics Experiments* (SNiPER) [59], which is tailored to the needs of neutrino experiments, including the possibility to account for time correlation between events. The software interface established standard libraries in particle physics like ROOT and BOOST python library to provide a solid foundation for simulation, reconstruction and analysis needs. SNiPER is implemented with an hybrid programming of C++ and python. With the python's interface a job can be configured through python scripts while the execution efficiency is assured by C++ kernel and functionalities. There is also a data buffer for memory management, which means a sequence of event in a time window, so that is able to analyze the correlation between different events. Alongside the SNiPER framework an *offline* software to allow to generate and analyze data is developed. An offline software is a bridge between detector and physics analysis, which makes it a big part of an experiment. For JUNO, since data taking has not started yet, the studies rely upon JUNO offline software simulation and this consists of several parts and packages:

- Raw data event builder
- Simulation
- Reconstruction
- Calibration
- Analysis

The software completes the full chain including physics generator, detector simulation, electronics simulation, waveform reconstruction and vertex/energy/track reconstruction. The package of algorithms that are exclusive for JUNO is called *offline*.

3.1 MC Simulation

The JUNO simulation package consists as said above, of several parts, and this represents one crucial part of this work, since when data is not available for an experiment yet, *Monte Carlo* (MC) studies are the main source of information before real data is available. The physics generators take care of simulate correct input positions, directions and momentum for all the different channels of detection in the case of a Supernova burst. There will be one or more primary particles, then these and the secondaries ones will be transported and propagated into the detector . The detector system and its response need to be taken into account as well, at this point, including the geometry of all systems and the characteristics of the Liquid Scintillator (LS) and and the PMTs. Their modeling is based on the DAYA-BAY experience but of course redefined to meet JUNO purposes. The secondary particles are then propagated into the detector through GEANT4 tool [60, 61], which takes into account all the possible interactions according to their energy and momentum. In general

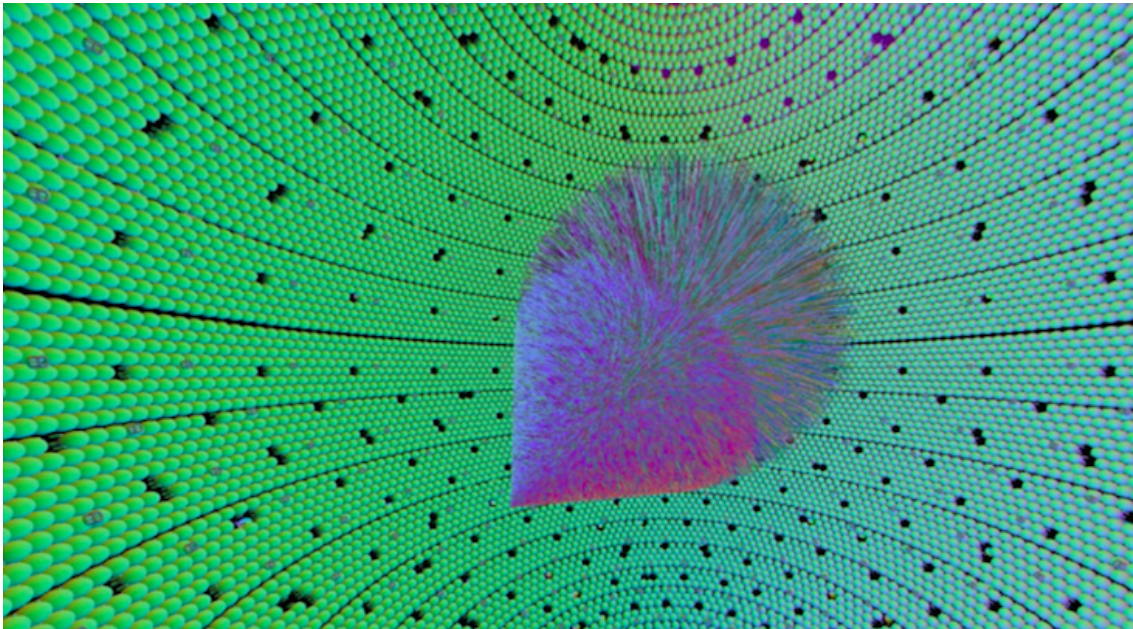


Figure 3.1: Simulated Cerenkov and scintillation photons from a 100 GeV muon travelling across JUNO anti-neutrino detector viewed from inside the spherical scintillator. Figure from [62].

the simulation of a LS detector produces a certain amount of photons that hit a PMT, bringing information about the time, PMT ID of the tube that has been hit and also the charge information. After having taken into account the detector response, the steps beyond the LS have to be simulated as well to evaluate the PMTs response and the subsequent digitization. In due course, the electronic simulation package will evaluate the PMTs effects, and through this step is also possible to mix different signals in a temporal relation. When dealing with real data, the main source of information are the sampled PMT wave-forms, which require specific algorithms to extract hit time and charges.

The Event Data Model (EDM) in JUNO was born to allow a fast browsing and to be able to store a large number of events, like the identification of time coincidences coming from correlated events can not be easy. To keep consistency, JUNO implements a static data model that discriminates between headers and actual events. There are different data structures, so that when browsing an event defined by its RUNID and EventID, only the headers are read in order to decide if the full data is needed. In this case the data can then be loaded from an event object that is derived from a ROOT TObjec.

For many physics cases expected in JUNO, the signal have a time correlation between different events. A time correlation between events is quite important for neutrino LS detectors. For this very reason, JUNO introduces the so-called EvtNavigator [63]. The principles and connection of the EvtNavigator is shown is Fig. 3.2.

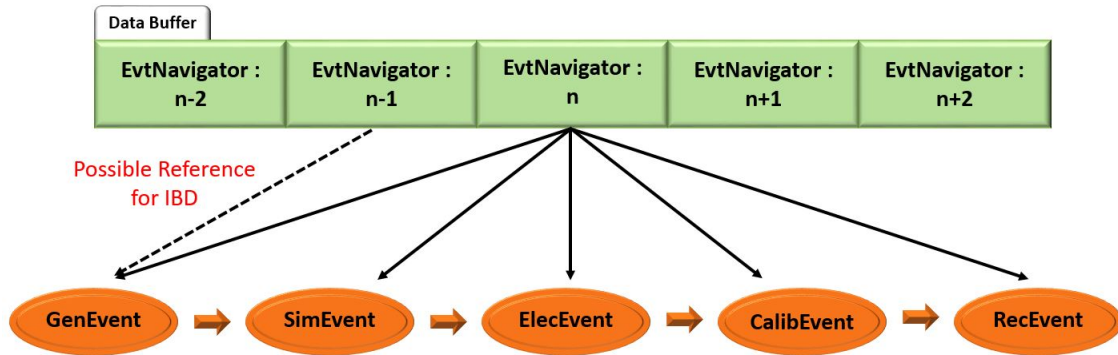


Figure 3.2: Principles of the EvtNavigator in SNIpER. It can read all the events and provide full access to the EDM.

The simulation of the event for the analysis taken into consideration in this work has to start from the generation of suitable CCSN bursts. The statistics for the simulation depends on the analysis that has been carried out. The work consists of two main studies:

- The Unfolding of the Energy Spectrum for a given progenitor mass
- The Reconstruction of the Progenitor Mass from the data detected and the time distribution

For the first study, two of the many models regarding the explosion of supernovae have been taken into account, the *Garching Model* [64] and the *Nakazato Model* [65] and for each, two independent data sample have been generated, so to use one of them as *fake-data*, simulating all the interaction channels expected in JUNO in a time interval of about 20 s. The primary neutrino flavours are $\bar{\nu}_e$, ν_e and ν_x . The energy range for neutrinos coming from a CCSN goes up to 50 MeV. In case of a SN burst, all the possible variables like, for example the Mass progenitor, the equation of state (EoS) and the distance in kpc of the object, have to be considered.

3.2 Supernova neutrino flux

As said before, different supernova models are available to reproduce the expected spectrum in the JUNO framework. For this work, the Garching Model [64] and the Nakazato Model [65] are used to parametrize the neutrino flux. In Fig. 3.3 is shown the fluence of different neutrino flavour for an average supernova at 10 kpc.

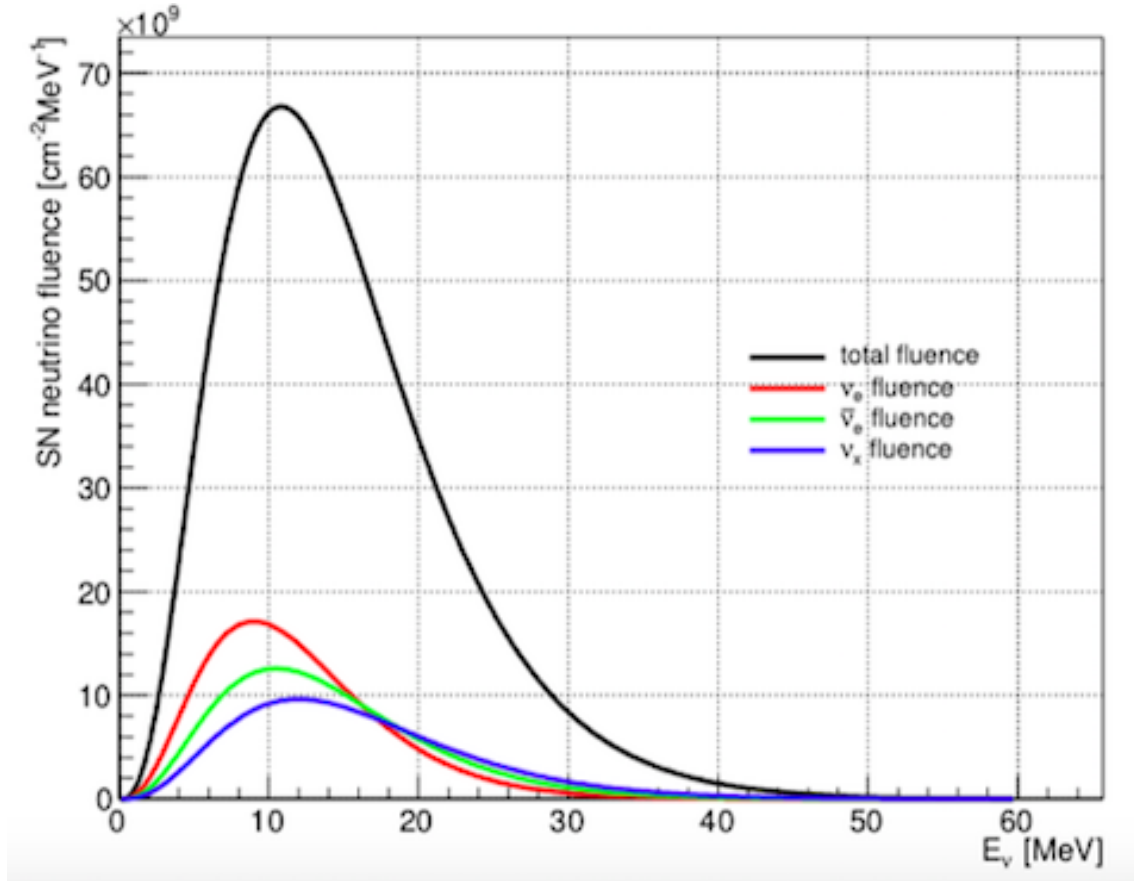


Figure 3.3: The Keil-Raffelt-Jana (KRJ) parametrization of the SN neutrino energy spectra with $\langle E_{\nu_e} \rangle = 12$ MeV, $\langle E_{\bar{\nu}_e} \rangle = 14$ MeV and $\langle E_{\nu_x} \rangle = 16$ MeV for a SN at 10 kpc.

In the above mentioned supernova models, flavour oscillations of the three active neutrino flavours are not self-consistently included. In view of the still incomplete understanding of the complex phenomenons that happen during a SN explosion, it cannot be excluded that neutrinos propagating through the dominant neutrino background outside the neutrino-sphere are important for the detectable neutrino signal and may have an impact of supernova nucleosynthesis, but it is unlikely they have a strong impact on the explosions. However to make the simulations more realistic neutrino flavour conversion has been added to the current work. Currently the supernova burst neutrino models used inside JUNO are spherically symmetric (1D) simulation results. They can provide the neutrino energy and time spectra for all flavour neutrinos emitted from the core of a SN.

The simulation of the two models rely on different characteristics, some of those have

been fixed in this work, respectively for the two models as it follows:

Nakazato Model

Supernova neutrino models from the Nakazato group are calculated by 1D numerical simulations from a variety of progenitor masses ($13M_{\odot}$, $20M_{\odot}$, $30M_{\odot}$, and $50M_{\odot}$) and two different metallicities ($Z=0.02$, and 0.004). An equation of state (EoS) by Shen [66] is utilized in the simulations. In addition, different shock revival time are investigated for each progenitor model ($t_{revive} = 100$ ms, 200 ms and 300 ms). The evolution of the supernova simulation covers the time from -0.05 s to 20 s after the bounce. The Model has 20 energy bins in the range 0 to 300 MeV. Hence after the integral of time or energy, the energy fluence or time distribution of SN neutrinos can be extracted.

Garching Model

In the JUNO Simulation Frameworks there are also 32 1D SN simulation models from the Garching Group, which cover progenitor masses $9.6 M_{\odot}$, $11.2M_{\odot}$, $18.6 M_{\odot}$, $20 M_{\odot}$, $25 M_{\odot}$, $27 M_{\odot}$ and $40 M_{\odot}$, using both Shen EoS as well as LS20 EoS to describe nuclear physics. For each progenitor there are four individual models, which include with or without mixing length convection or with and without the inclusion of nucleon potential effects in the neutrino-nucleon opacities [67]. The time of neutrino emission differs for each model, but cooling stages are all included.

The energy distribution can be described using a normalized Gamma function [68] at t_i :

$$f(\varepsilon) = \frac{\varepsilon^{\alpha}}{\Gamma_{\alpha+1}} \left(\frac{\alpha+1}{\langle E \rangle} \right) \exp \left[- \frac{(\alpha+1)\varepsilon}{\langle E \rangle} \right] \quad (3.1)$$

where Γ is the Gamma function, $\langle E \rangle$ is the average energy and α is a shape parameter, where $\alpha = 2$ corresponds to the Maxwell-Boltzmann distribution. Additionally, the parameters of the energy distribution can be obtained from the following:

$$\alpha = \frac{\langle E^2 \rangle - 2\langle E \rangle^2}{\langle E \rangle^2 - \langle E^2 \rangle} \quad (3.2)$$

In this way the data from the Garching are comparable with the Nakazato models. The neutrino energy fluences from Garching group fluctuate in a larger extend compare to the Nakazato group.

3.3 Flavor Conversion of SN burst neutrinos

After the few-tens MeV SN burst neutrinos are emitted from the core, the flavour conversion of them is complicated due to the high dense matter and large neutrino background. In their way from the core to the detector placed on Earth, neutrino may experience several flavor conversions as shown in Fig. 3.4. Inside the SN core (with R smaller than 10 km), neutrinos are in fact trapped and the lepton flavors are roughly conserved thanks to the frequent scattering of neutrinos with nuclei, hence no oscillations. Subsequently in the travel from the neutrino-sphere to hundreds of kilometers forward, flavor conversion

may although happen, even if it is a process not completely clear. When the radius reach around thousands of kilometers, the MSW effects kicks in, and the resonance flavor conversion in the envelope of SN can be completely adiabatic. Afterwards, wave packets of mass eigenstates spread and separate on the way to Earth [69].

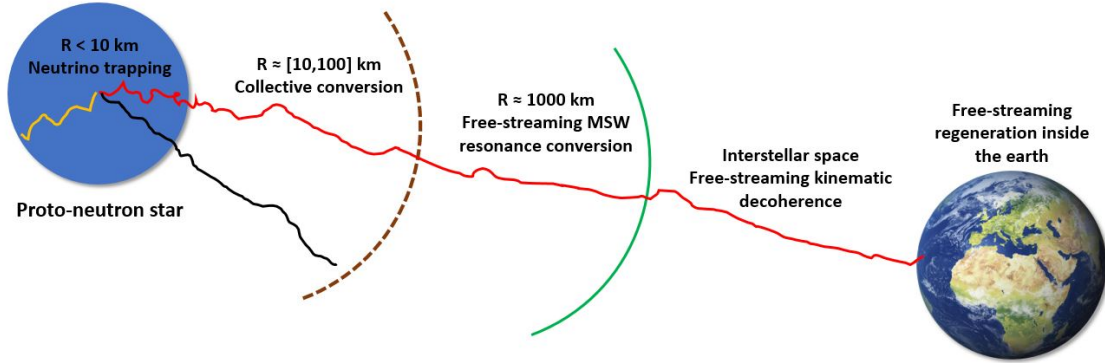


Figure 3.4: Possible flavor conversion of supernova neutrinos during their propagation from the core to the Earth

If just the MSW resonance effect is considered the flavor conversion relations are as follows:

$$\begin{aligned}
 F_{\nu_e}(E, t) &= pF_{\nu_e}^0(E, t) + (1 - p)F_{\nu_x}^0(E, t) \\
 F_{\bar{\nu}_e}(E, t) &= \bar{p}F_{\bar{\nu}_e}^0(E, t) + (1 - \bar{p})F_{\bar{\nu}_x}^0(E, t) \\
 F_{\nu_\mu + \nu_\tau}(E, t) &= (1 - p)F_{\nu_e}^0(E, t) + (1 + p)F_{\nu_x}^0(E, t) \\
 F_{\bar{\nu}_e + \bar{\nu}_\tau}(E, t) &= (1 - \bar{p})F_{\bar{\nu}_e}^0(E, t) + (1 + \bar{p})F_{\bar{\nu}_x}^0(E, t)
 \end{aligned} \tag{3.3}$$

where F_ν^0 are the neutrino flux emitted at the source and x represents μ and τ . The flavor conversion for SN burst neutrinos depend on mass hierarchy. In case of NMO, $p = \sin^2 \theta_{13} \approx 0.022$ and $\bar{p} = \cos^2 \theta_{13} \cos^2 \theta_{12} \approx 0.687$, in case of IMO $p = \sin^2 \theta_{12} \cos^2 \theta_{13} \approx 0.291$ and $\bar{p} = \sin^2 \theta_{13} \approx 0.022$

3.4 Neutrino Interactions

The few-tens MeV SN burst neutrinos, in the LS detector in JUNO, can be detected via multiple channels as shown in Tab. 3.1 below:

Channels	Type	Events for different E_ν values		
		12 MeV	14 MeV	16 MeV
$\bar{\nu}_e + p \rightarrow p + n$	CC	$4.3 \cdot 10^3$	$5.0 \cdot 10^3$	$5.7 \cdot 10^3$
$\nu + p \rightarrow \nu + p$	NC	$0.6 \cdot 10^3$	$1.2 \cdot 10^3$	$2.0 \cdot 10^3$
$\nu + e \rightarrow \nu + e$	ES	$3.6 \cdot 10^2$	$3.6 \cdot 10^2$	$3.6 \cdot 10^2$
$\nu + {}^{12}\text{C} \rightarrow \nu + {}^{12}\text{C}^*$	NC	$1.7 \cdot 10^2$	$3.2 \cdot 10^2$	$5.2 \cdot 10^2$
$\nu_e + {}^{12}\text{C} \rightarrow e^- + {}^{12}\text{N}$	CC	$0.5 \cdot 10^2$	$0.9 \cdot 10^2$	$1.6 \cdot 10^2$
$\bar{\nu}_e + {}^{12}\text{C} \rightarrow e^+ + {}^{12}\text{B}$	CC	$0.6 \cdot 10^2$	$1.1 \cdot 10^2$	$1.6 \cdot 10^2$

Table 3.1: Numbers of neutrino events in JUNO for a SN at typical distance of 10 kpc, where ν collectively stands for neutrinos and anti-neutrinos of all three flavors and their contributions are summed over. Three representative values of the average neutrino energy $\langle E_\nu \rangle = 12$ MeV, 14 MeV and 16 MeV are taken for illustration, where in each case the same average energy is assumed for all flavors and neutrino flavor conversions are not considered. For the elastic neutrino-proton scattering, a threshold of 0.2 MeV for the proton recoil energy is chosen.

3.4.1 Inverse Beta Decay

The inverse beta decay given by $\bar{\nu}_e + p \rightarrow n + e^+$ is the golden channels in LS detector. The total number of IBD events is given by the following relation:

$$N_{IBD} = N_P \int_{E_{\bar{\nu}_e}} \int_t \int_{\cos\theta} F_{\bar{\nu}_e}(E_\nu, t) \sigma(E_\nu, \theta) dE_\nu dt d\cos\theta \quad (3.4)$$

where θ is the angle between the positron and the anti-neutrino and N_P is the number of free protons in the LS. JUNO is assumed to have 20 kton fiducial mass with 12% protons and 88% carbons. The interaction threshold energy of incident $\bar{\nu}_e$ is $E_\nu^{thr} \approx 1.806$ MeV. While the differential IBD cross-section considered with the next-to-leading order (NLO) approximation is :

$$\frac{d\sigma}{d\cos\theta} = (E_\nu, \cos\theta) = \frac{p_e \varepsilon}{1 + \varepsilon(1 - (E_e p_e \cos\theta))} \frac{d\sigma}{dE_e} \quad (3.5)$$

where the positron energy E_e is related to the initial $E_{\bar{\nu}_e}$ through equation:

$$E_e = \frac{(E_\nu - \delta)(1 + \varepsilon) + \varepsilon \cos\theta \sqrt{(E_\nu - \delta)^2 - m_e^2 k}}{k} \quad k = (1 + \varepsilon)^2 - (\varepsilon \cos\theta)^2 \quad (3.6)$$

corresponding to the distribution of $F_{\bar{\nu}_e}(E_\nu, t) \sigma(E_\nu, \theta)$, the time t , energy of the $\bar{\nu}_e$ and the angle θ can be generated randomly, where the distribution of Φ is considered uniform. The positron energy can be calculated thanks to Eq. 3.6 and then the momentum as well. From the conservation of the momentum the information of the final-state neutron can be achieved. The positron and neutron will induce a prompt and delayed signal respectively. The anti-neutrino $\bar{\nu}_e$ interacts with a protons and creates the positron and the neutron. The positron quickly deposits its energy and annihilates into two 511- keV γ -rays, which

is what gives the prompt. The neutron scatters in the detector until being thermalized. It is then capture around 200 μs later and releases a 2.2 MeV γ -ray.

3.4.2 Neutrino-proton elastic scattering

All flavors neutrinos will contribute to the neutrino proton-elastic scattering (pES), $\nu + p \rightarrow \nu + p$. The estimation of total number of pES is analog to the IBD channel, but for all flavor, shown in Eq. 3.7

$$N_{pES} = N_P \sum_{\alpha} \int_{E_{\nu\alpha}} \int_t \int_{\cos\theta} F_{\nu\alpha}(E_{\nu}, t) \sigma_{\alpha}(E_{\nu}, \theta) dE_{\nu} dt d\cos\theta \quad (3.7)$$

where α of course refers to the different neutrino flavors. The cross-section used for the pES in the JUNO software framework is taken from [70]:

$$\frac{d\sigma}{dQ^2} = \frac{G_F^2 M_P^2}{8\pi E_{\nu}^2} \left[A \pm B \frac{(s-u)}{M_P^2} + C \frac{(s-u)^2}{M_P^4} \right] \quad (3.8)$$

Where $Q^2 = 2M_P T_P$, in which T_P is the recoiled energy of the proton, and above the plus sign is for neutrinos and the minus sign is for antiparticles. In the limit $2E_{\nu}^2/M_P \ll E_{\nu}$, the cross sections for neutrinos and anti-neutrinos are almost identical. The direction of the recoiled proton is a two particle decay problem and can be calculated like below:

$$E_{\nu} = \frac{M_P}{\cos\theta p(1 + 2M_P/T_P)^{1/2} - 1}$$

$$T_P^{max} = \frac{2E_{\nu}^2}{M_p + 2E_{\nu}} \quad (3.9)$$

Like the IBD, the time t , the neutrino energy E_{ν} and the angle θ can be generated corresponding to $\sum_{\alpha} F_{\nu\alpha}(E_{\nu}, t) \sigma_{\alpha}(E_{\nu}, \theta)$. Of course for this channel, only one particle is simulated, which is the recoiled proton.

3.4.3 Neutrino-electron elastic scattering

Analogous to pES, the neutrino-electron scattering (eES) uses the same calculation seen in Eq. 3.7, in which N_P is replaced with N_e and produces the random final-state in the same way. Although, the cross-section for this process is different.

eES is a leptonic process where a neutrino scatters off an electron by the exchange of a virtual vector boson. For ν_e and $\bar{\nu}_e$, there are both neutral-current and charge-current interactions. While only neutral-current events exist for ν_x .

$$\frac{d\sigma_{\nu_x}}{dy} = \frac{2G_{\mu}^2 m_e E_{\nu}}{\pi} \left[\varepsilon_-^2 + \varepsilon_+^2 (1+y)^2 - \varepsilon_- \varepsilon_+ \frac{m_e}{E_{\nu}} y \right] \quad (3.10)$$

$$\frac{d\sigma_{\bar{\nu}_x}}{dy} = \frac{2G_{\mu}^2 m_e E_{\nu}}{\pi} \left[\varepsilon_+^2 + \varepsilon_-^2 (1+y)^2 - \varepsilon_- \varepsilon_+ \frac{m_e}{E_{\nu}} y \right] \quad (3.11)$$

in which $\varepsilon_- = \frac{1}{2} - \sin^2 \theta_W$ and $\varepsilon_+ = -\sin^2 \theta_W$, and y is related to the electron recoiled energy E'_e like below:

$$y = \frac{E'_e - m_e}{E_\nu}, \quad 0 < y < y_{max} = \frac{1}{1 + \frac{m_e}{2E_\nu}} \quad (3.12)$$

The cross-section for ν_e and $\bar{\nu}_e$ can be obtained by replacing ε_- with $\varepsilon'_- = -\frac{1}{2} - \sin^2 \theta_W$ and ε_+ with $\varepsilon'_+ = -\sin^2 \theta_W$.

3.4.4 ^{12}C CC and ^{12}C NC

There are both CC and NC interaction on ^{12}C in LS:

$$\nu_e + ^{12}\text{C} \rightarrow e^- + ^{12}\text{N}, \quad ^{12}\text{N}(1^+, gnd) \rightarrow ^{12}\text{C}(0^+, gnd) + e^- + \nu_e \quad (3.13)$$

$$\bar{\nu}_e + ^{12}\text{C} \rightarrow e^+ + ^{12}\text{B}, \quad ^{12}\text{B}(1^+, gnd) \rightarrow ^{12}\text{C}(0^+, gnd) + e^+ + \bar{\nu}_e \quad (3.14)$$

$$\nu + ^{12}\text{C} \rightarrow \nu + ^{12}\text{C}^* \quad (3.15)$$

The CC interaction on ^{12}C will take place for ν_e and $\bar{\nu}_e$. In NC interactions most ^{12}C will transit to the ground state of ^{12}N and ^{12}C , while other indirect processes from other excited states are negligible for SN neutrinos. This appears to be also true for ^{12}C NC interactions. The energy threshold for the process involving the ν_e in ^{12}N CC is approximately 17.34 MeV, while that for $\bar{\nu}_e$ in ^{12}B CC is approximately 14.39 MeV. The momentum for the final state electron in both scenario can be found considering the nuclei at rest in the laboratory frame. Both ^{12}N and ^{12}B states will decay with respectively 11 ms and 20.2 ms half-life, leading to a prompt-delayed signals.

The NC interaction has contributions from all flavor neutrinos. The de-excitation of $^{12}\text{C}^*$ to its ground state will produce a 15.11 MeV γ , and this represents a clear signal for this channel. The cross-section for MeV interactions on ^{12}C can be evaluated by using a direct evaluation of nuclear matrix elements from experimental data.

For the simulation of SN neutrinos from the Nakazato Model we need to define:

- the input flux file of the neutrino model
- the distance of the SN to the Earth. For a galactic CCSN, 10 kpc is a typical choice for SN burst neutrino
- whether the mass hierarchy is normal or inverted
- set a metallicity value
- The value of the shock revival time

While when taking into consideration neutrinos generated from the Garching Model:

- the input flux of the neutrino model;

- the distance of the SN to the Earth;
- whether the mass hierarchy is normal or inverted;
- The EoS, which to keep consistency with the comparison with the Nakazato Model , has been set to Shen;
- the convective motion; for this work the full set of opacities has been used, but convection and nucleon potentials have not been considered.

Once the events are generated, they get sorted in a time sequence according to the first visible particle time. With the information provided by the simulation the energy distribution of the final-state particle can be illustrated. The full simulation of neutrino interactions

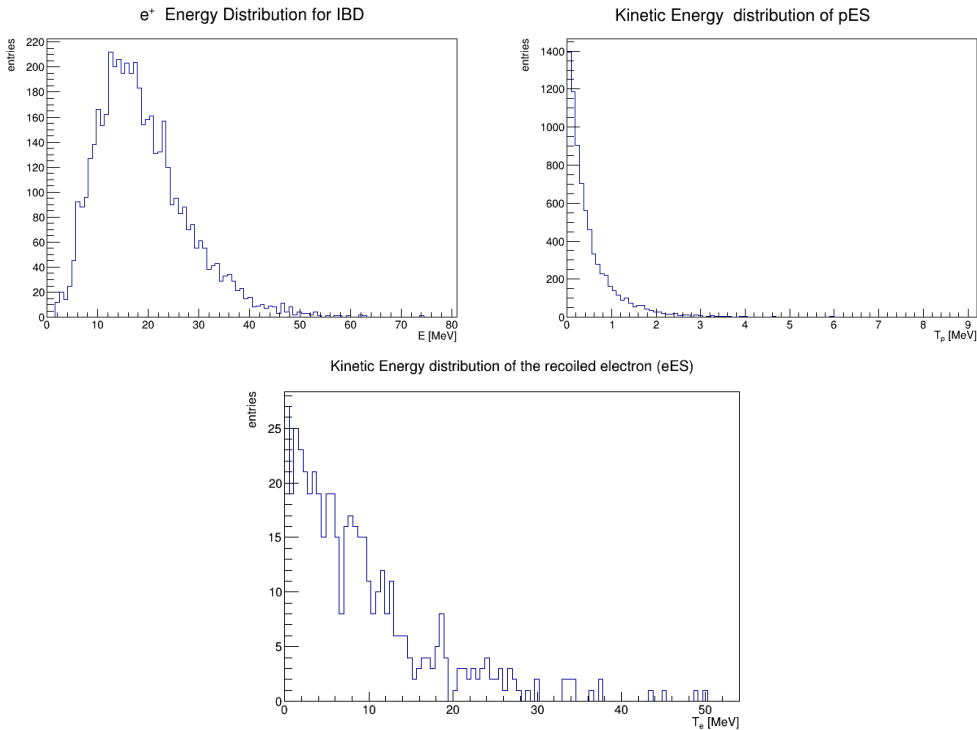


Figure 3.5: Energy distribution for the three main channels in a SN neutrino burst. First row, the plot on the left shows the energy distribution for e^+ on IBD; the plot on the right shows the final state kinetic energy distribution of the recoiled proton of pES, and eES (bottom plot).

and particularly the propagation of secondaries requires quite some computational time.

3.5 Detector Simulation

The JUNO detector simulation, as partially anticipated above, is developed under the SNiPER framework, based on GEANT4 [60, 61]. The detector simulation takes the interaction vertices coming from the generator and propagates them inside the detector. The GEANT4 libraries are able to recreate all the processes related to energy loss and

scintillation. Also several physics processes are implemented like electromagnetic interactions, decays, elastic and inelastic interactions, and scintillation, including re-emission, Cherenkov emission and optical absorption.

After the neutrino interactions and production of secondaries particles, the output scintillation photons can undergo absorption, re-emission, scattering, all according to the optical model implemented in the simulation. All the processes include the propagation of the photons to the PMTs, the interactions with the photo-cathode and in the end the production of the photo-electrons (PEs), by embedding the PMTs QE. The PE production after a photon interaction with the photo-cathode is referred to as a *hit*.

The fake data for this work have been generated from an independent MC simulation. For an average SN of $20M_{\odot}$ at the center of the Galaxy (i.e. 10 kpc) the expected event rate is roughly 15000 events in the space of 20 s.

3.6 Electronic Simulation

The hits of the photons on the PMTs produce a cascade of electrons, which is digitized by an analog-to-digital converter (ADC). This is reproduced in the electronic simulation algorithm, while at the same time properly considering the response from the read-out system. Further aspects, like trigger and the dark noise are taken into account as well. The waveforms for each event are generated and saved [63, 71].

3.7 Calibration

As the last step, the number of P.E. that contributed to a single waveform, is reconstructed for each hit. This is achieved by a waveform deconvolution using calibration data that was evaluated before hand for each PMT [63]. After the deconvolution the integrated charge and time is retrieved. The calibration data level coming from this step is used for event reconstruction in this work.

Chapter 4

Neutrino Identification and sample selection

The signal from a SN contains as mentioned in Section 3.4, different detection channels in the JUNO detector. These events have to be classified and assigned to their respective underlying interactions in order to do further analysis. As for now, the event selection only identifies the three main channels for supernova neutrinos. These are the inverse beta decay (IBD), the proton elastic scattering (pES) and the electron elastic scattering (eES). The visible energy spectra of all the detectable processes in JUNO are shown in Fig. 4.1.

The selection of the above mentioned channels can be done through a time window and thanks to the deposited energy in the CD, and therefore through the integrated charge registered by the PMT systems. For this analysis only the LPMT system is taken under consideration. The selection criteria applied to the events is done through a vertex fiducial cut, as a first step to remove all the edge events which may be badly reconstructed and then through a charge fiducial cut which corresponds to the deposited energy of the particles in the CD. Below in Figs. 4.2, 4.3 and 4.4, the observable distributions at the end of the full simulation chain is reported for all three channels, before any cut.

The distributions in Fig. 4.2, Fig. 4.3 and Fig. 4.4 are the result of a SN explosion of a $20M_{\odot}$ at 10 kpc. In Fig. 4.2 there is a visible peak, at around 2000/3000 p.e which corresponds at 2.2 MeV which is generated by the neutron capture characteristic of an IBD event. The same distributions have been built for a $20 M_{\odot}$ at 10 kpc for the Nakazato model. From the comparison of the three distributions we can notice that with a fiducial cut we can isolate each channel with a residual contamination from the others to be evaluated. In case of the IBD channel a fiducial cut on the charge will eliminate any contamination from the pES scattering, which are peaked in the very low MeV range as shown also in Fig. 4.1. As it is noticeable, the distribution concerning the Garching Group is showing the trend of the different processes looking at the reconstructed integrated charge at the end of the chain, while the one for the Nakazato Model is showing the total charge collected by the PMTs, not yet reconstructed. This is due to the fact that when dealing with the two different models the simulation framework encounters some

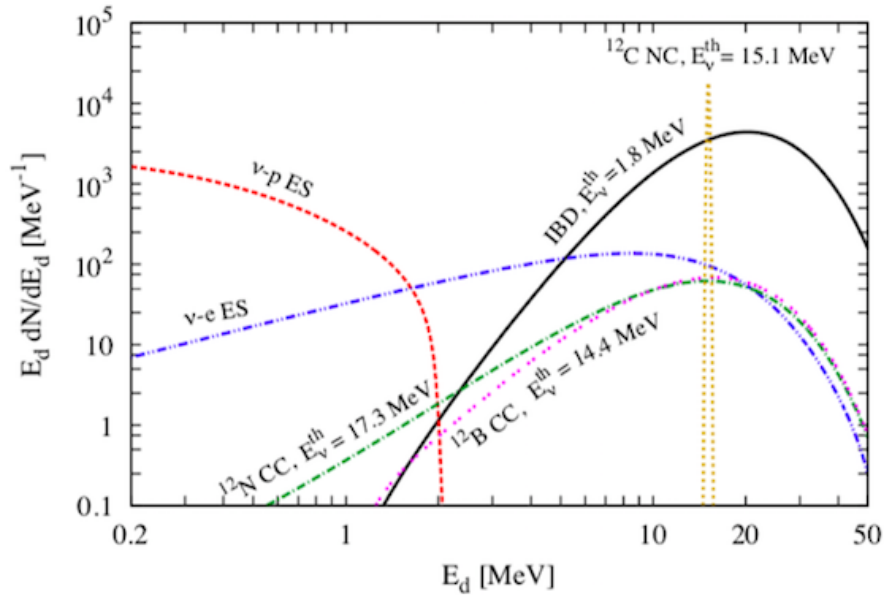


Figure 4.1: The neutrino event spectra with respect of the visible energy E_d in the JUNO detector for a SN at 10 kpc, where no flavor conversions are assumed and the average neutrino energies are $\langle E_{\nu_e} \rangle = 12$ MeV, $\langle E_{\bar{\nu}_e} \rangle = 14$ MeV, and $\langle E_{\nu_x} \rangle = 16$ MeV. The main reaction channels are shown with the relative threshold of the neutrino energies: for the IBD: $E_d = E_\nu - 0.8$; elastic ν -p scattering, for which the E_d represents the recoiled energy of the proton; ν -e elastic scattering, for which E_d is the recoiled energy of the electron; the neutral current reaction $^{12}\text{C}(\nu, \nu')\text{C}^*$, for which $E_d \approx 15.11$ MeV; Charged-current reaction $^{12}\text{C}(\nu_e, e^-)^{12}\text{N}$, for which $E_d = E_\nu - 17.3$ MeV; and Charged-current reaction $^{12}\text{C}(\bar{\nu}_e, e^+)^{12}\text{B}$, for which $E_d = E_\nu - 13.9$ MeV

difficulties, due to the different format of the models and characteristics. Both have been adapted to work inside the JUNO framework, but the latter has some aspects to be defined yet. So on the data coming from this has been applied a smearing when performing the analysis.

4.1 Fiducial cuts

As a first step to remove edge events a fiducial cut on the vertex has been applied, then to separate the three different channel a fiducial cut on the charge as a number of reconstructed p.e. has been set, so to eliminate as much contamination as possible between the three channels when studying them separately:

$R_{\text{VERTEX}} < 16$ m. The cut on the vertex position has been set uniquely to remove events that release their energy at the edge of the acrylic sphere. This class of events typically show a deviation from the linearity between the true energy and the reconstructed one. First of all, because part of the energy is released in the acrylic sphere rather than in the LS and second of all, the PMTs collect so much light that can go in saturation mode. In case of a SN burst this can be very plausible, because the event rate in a limited time is quite high, so even with more reason those events have been not considered. The

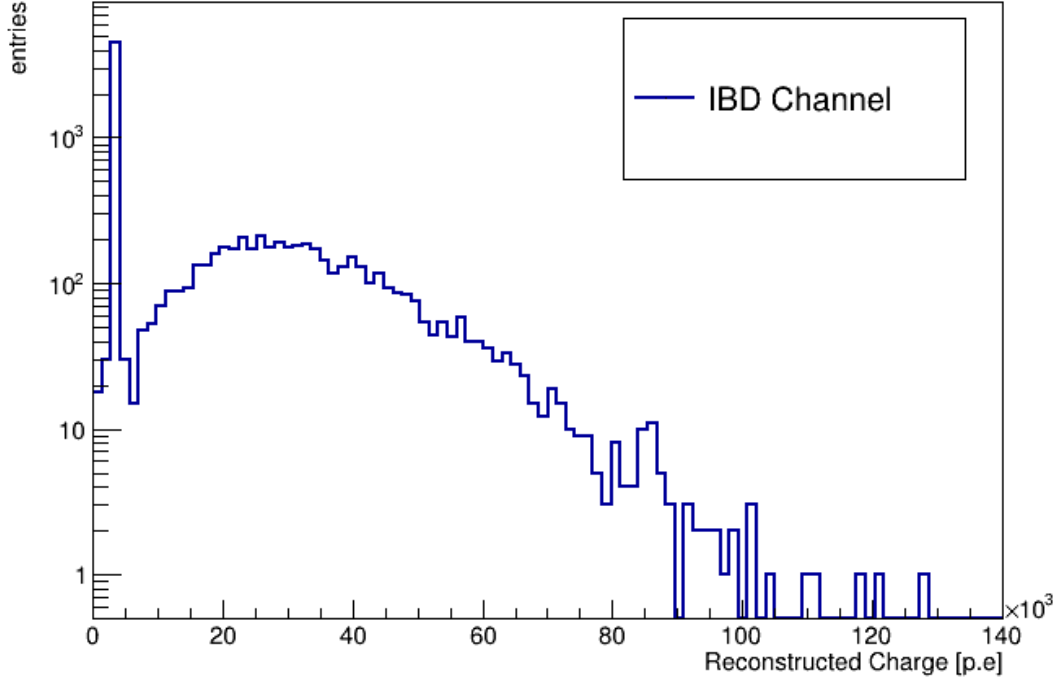


Figure 4.2: Charge distribution as a fraction of the number of photoelectrons (p.e.) for the IBD sub-sample

R_{VERTEX} is the vertex radius, i.e. the distance between the vertex and the center of the sphere.

To represent reality as better as possible and reproduce the uncertainty on the reconstruction of the vertex position, the true MC position has been slightly modified as it follows:

$$\vec{\rho}_{RECO}(x', y', z') = \vec{\rho}_{TRUE}(x, y, z) \oplus f_{GAUS}(\sigma = 1m) \quad (4.1)$$

where f_{GAUS} is a gaussian function with a variance σ of 1 meter. The estimated performance of JUNO on $\mathcal{O}(\text{MeV})$ is a little as few cm. The main fiducial cut also used to discriminate between the channels, is the one on the integrated charge.

- $20 \times 10^3 < \mathbf{Q}[\mathbf{p.e}] < 90 \times 10^3$ for the **IBD** golden channel. This cut is performed with the scope to isolate the current process and eliminate the contamination from the other channels;
- $0 < \mathbf{Q}[\mathbf{p.e}] < 3 \times 10^3$ for the **pES**;
- $1 \times 10^3 < \mathbf{Q}[\mathbf{p.e}] < 20 \times 10^3$ for the **eES**.

The efficiency of these cuts can be reported to assure the quality of it and the not degradation of the data after it. All of the above is applied for the Garching Model and similarly

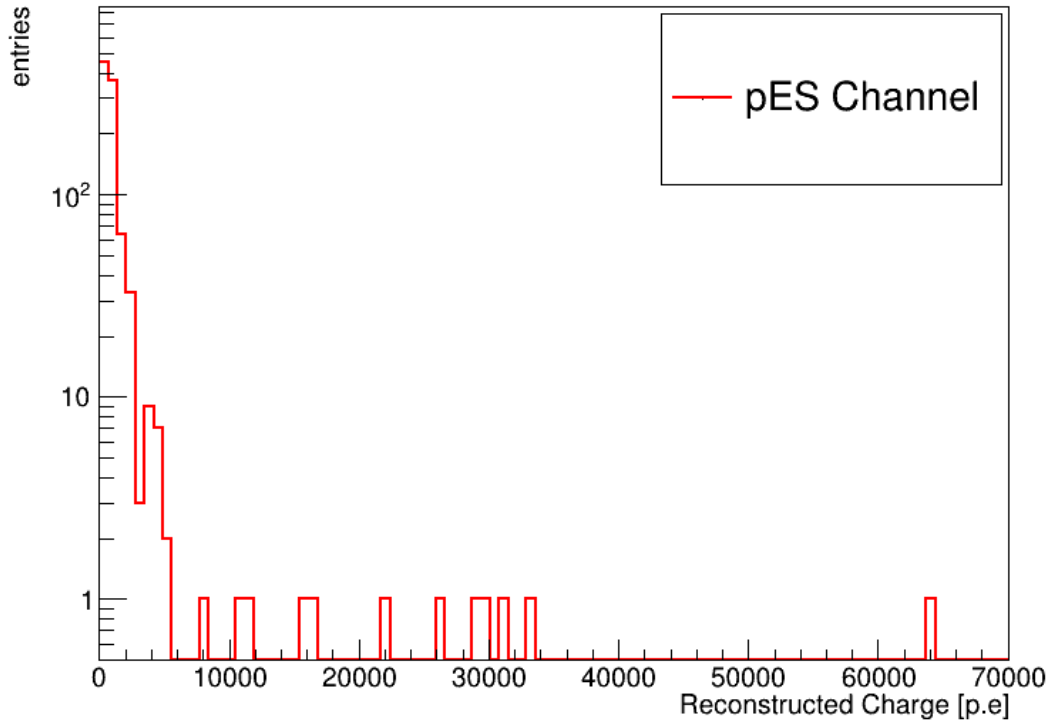


Figure 4.3: Charge distribution as a fraction of the number of photoelectrons (p.e.) for the pES sub-sample

to the Nakazato Model on the NPEs. Fiducial cuts are classified as quality cuts, because they remove the poorly reconstructed events. The efficiency of the fiducial cuts is reported in Tab. 4.1 singularly and combined together, while Fig. 4.7, Fig. 4.8, Fig. 4.9 and Fig. 4.10 show the effects of the two fiducial cuts combined together on the three different detectable processes. The last channel is clearly the one more contaminated by the main two channels, both because of less number of events and visible energy spectrum.

IBD selection

In order to isolate the inverse beta decay channel, a cut on the reconstructed charge of $20 \times 10^3 < Q < 90 \times 10^3$ p.e. is required. This translates in an efficiency on the detection of

Selection	IBD	pES	eES
$R_{VERTEX} < 16$ m	89 %	84 %	60 %
$min_{cut} < Q[p.e] < max_{cut}$	41%	97%	89 %
Total	40 %	81 %	60 %

Table 4.1: Summary of efficiency of the fiducial cuts alone and combined together. The efficiency are presented for each processes, and the cut on the observable is variable depending on the selection of the channel as seen before.

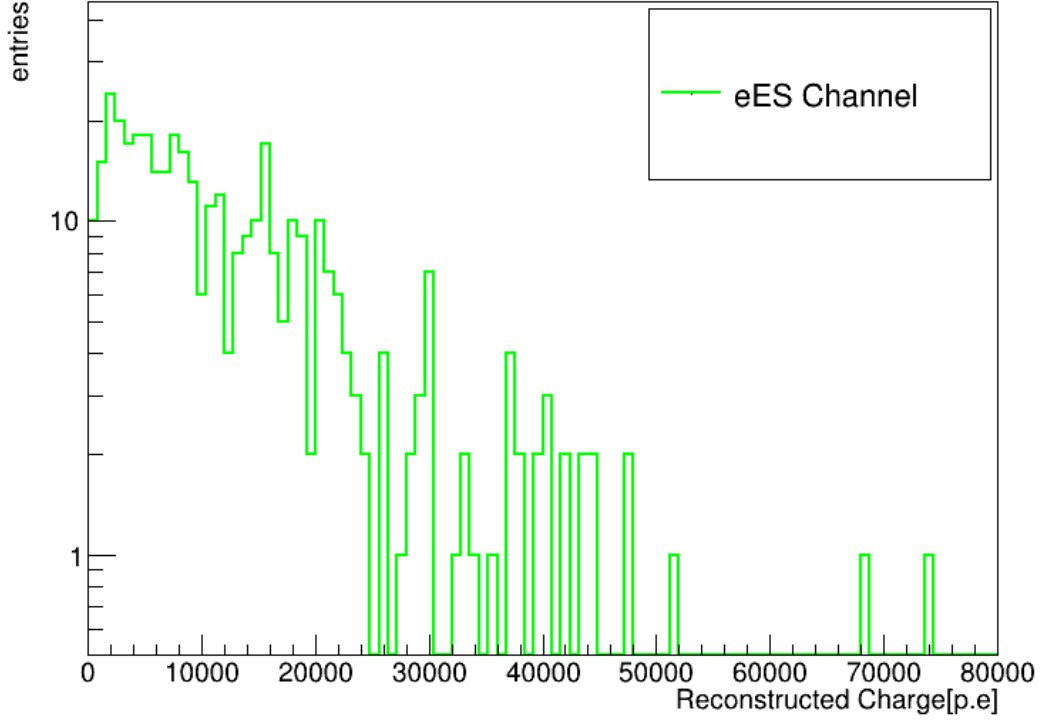


Figure 4.4: Charge distribution as a fraction of the number of photoelectrons (p.e.) for the eES sub-sample

the $\bar{\nu}_e$ of 74 % with respect to the sample after all the cuts, with a residual contamination of 7 % from ν_e and ν_x and $\bar{\nu}_x$ coming from the elastic scattering.

pES selection

For the ν coming from the proton elastic scattering the same procedure has been followed, with a fiducial cut of $Q < 3 \times 10^3$ p.e. , an efficiency of 84 % on the signal is reached, with a residual contamination of 0.6% from the ν_e and ν that undergo the other processes.

eES selection

The signal efficiency for the electron elastic scattering is about 60 % , but the contamination on this signal is the highest of all.

This is due to the lack of events detectable and to the range of the energy spectrum of this channel. This, as can be seen from Fig. 4.1, is dominated by the IBD energy spectrum and the proton elastic scattering energy spectrum, a part from a small part of the visible energy spectrum in the range of few MeV, but with cost on the event number. The result is a residual contamination of 50 % from other neutrinos. A pulse shape discrimination

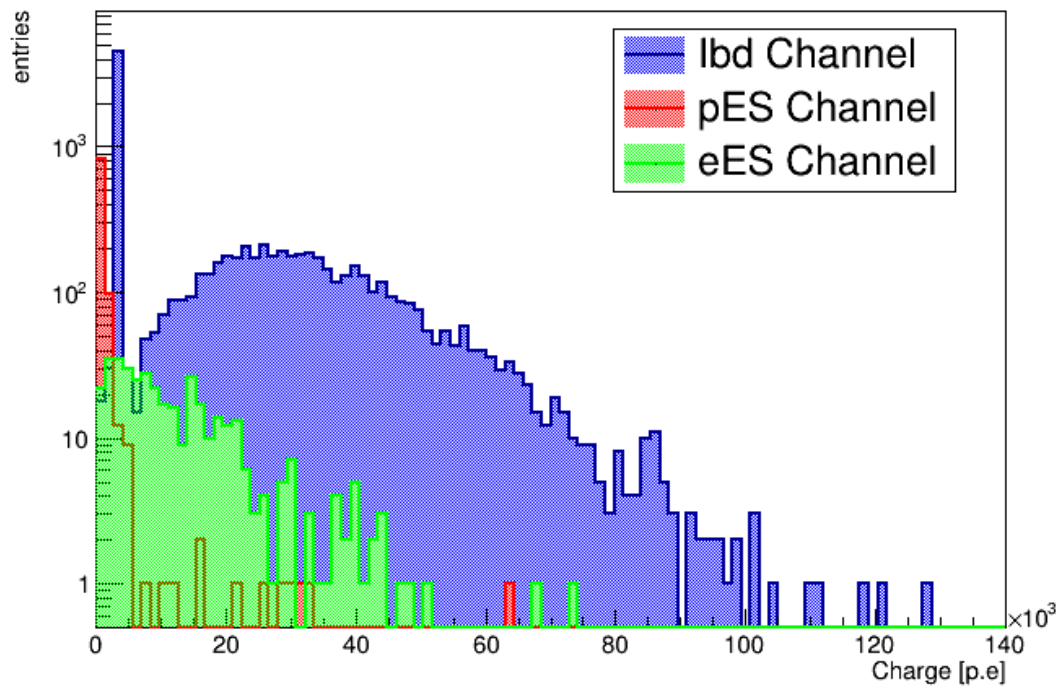


Figure 4.5: Charge observable distribution for the three main channel under investigation for the Garching model before any fiducial cuts

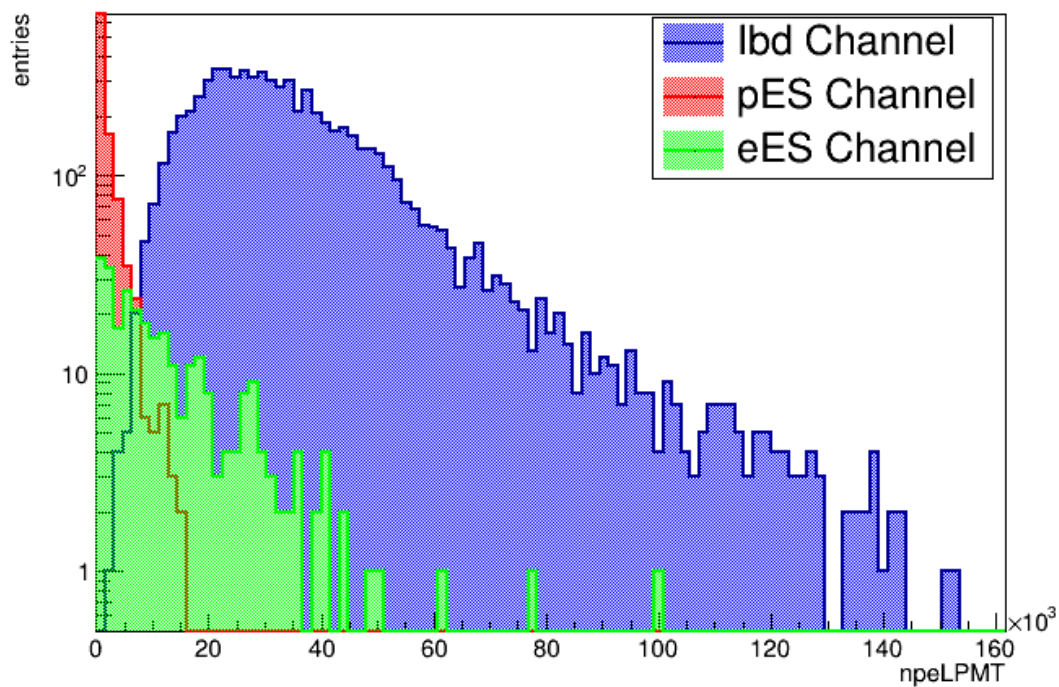


Figure 4.6: Number of photoelectrons distribution for the three main channel under investigation for the Nakazato Model before any fiducial cuts

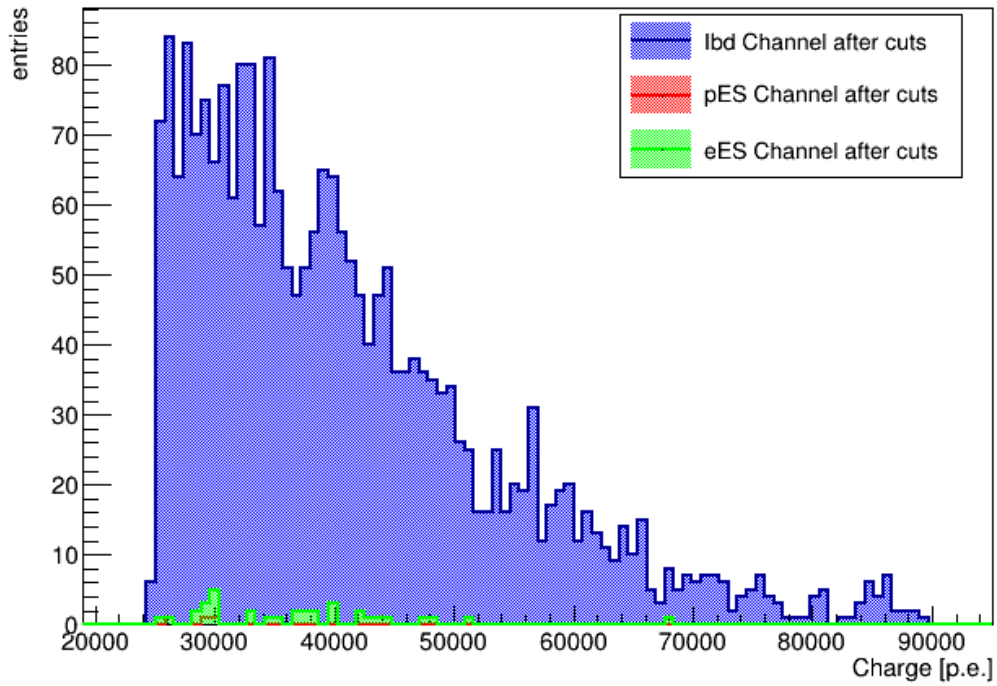


Figure 4.7: Effects of the fiducial cuts on the observable visible spectrum for the Garching model, applying the IBD cut

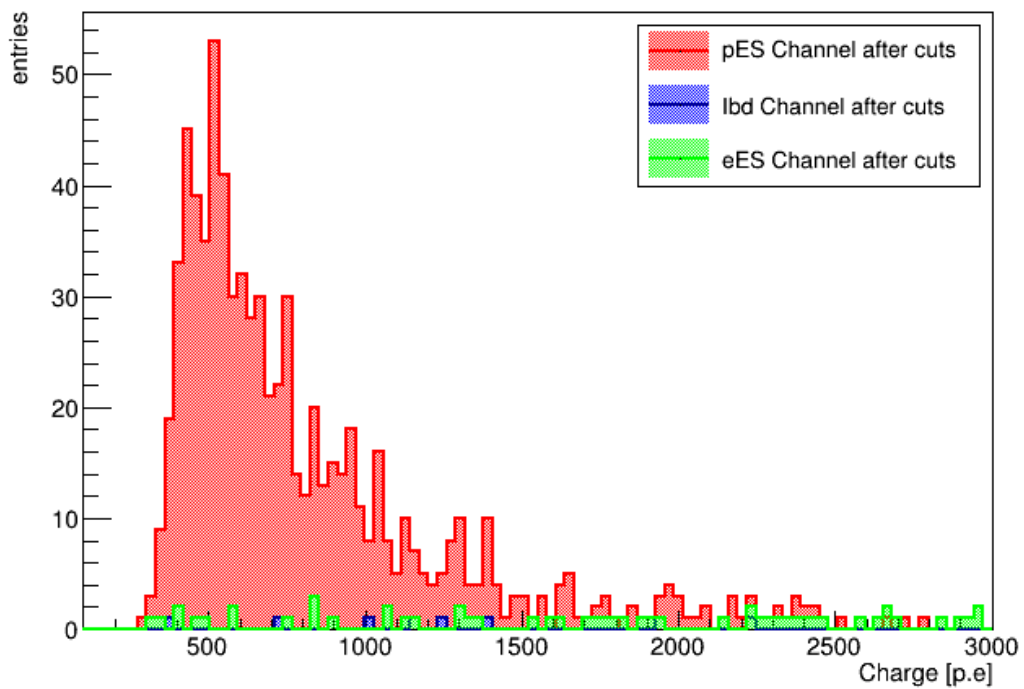


Figure 4.8: Effects of the fiducial cuts on the observable visible spectrum for the Garching model, applying the pES cut

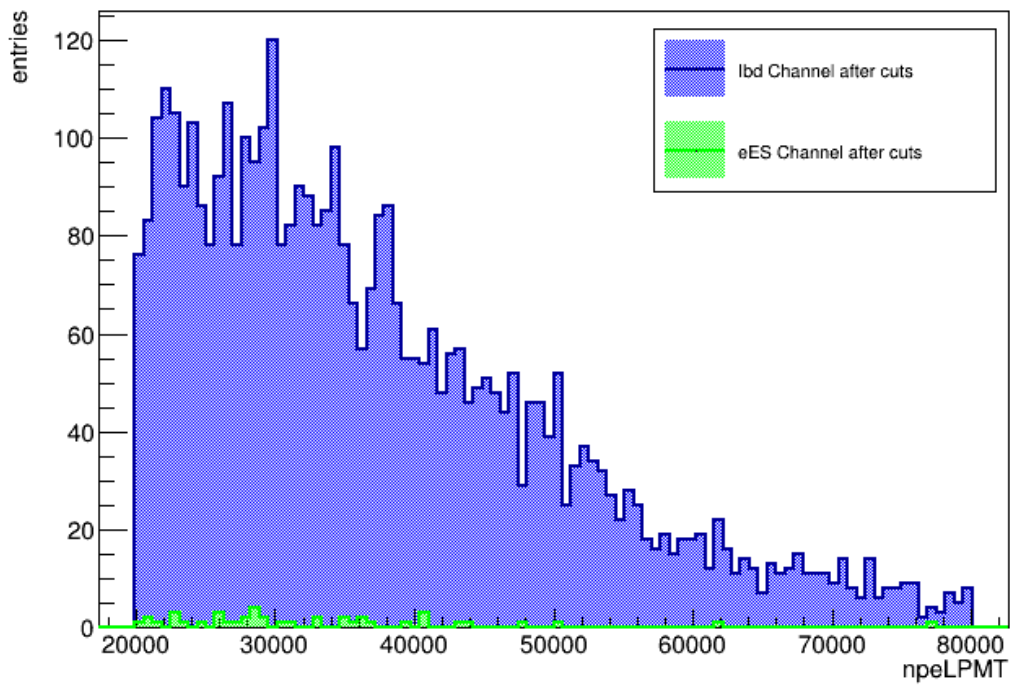


Figure 4.9: Effects of the fiducial cuts on the observable visible spectrum applying the IBD cut for the Nakazato Model

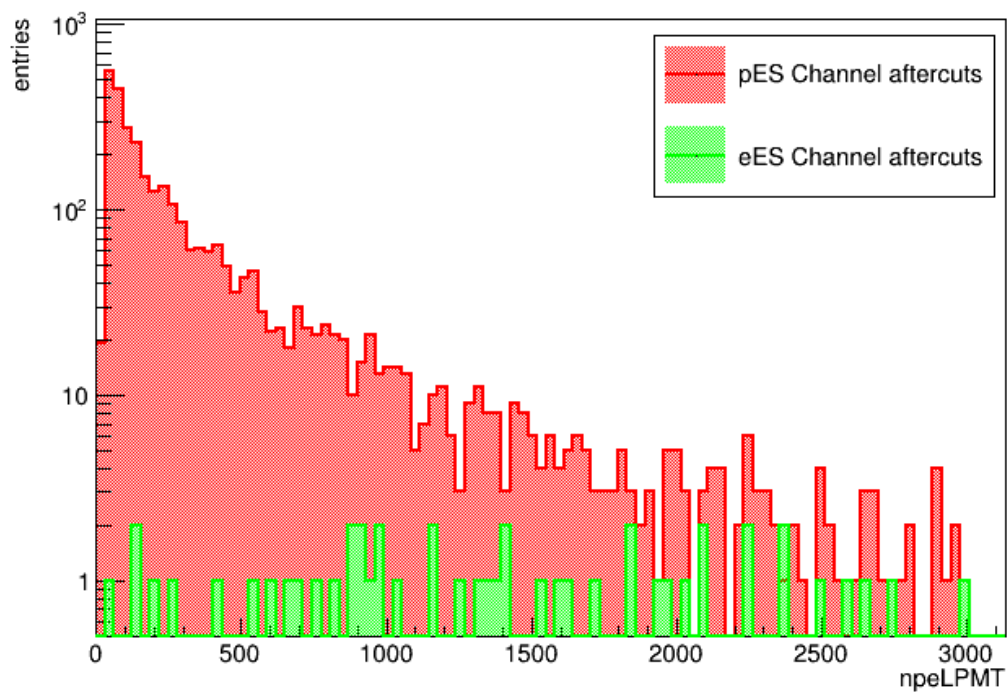


Figure 4.10: Effects of the fiducial cuts on the observable visible spectrum for the Nakazato model, applying the pES cut

could help to improve the efficiency of the chosen cut and it will be object of further studies.

Chapter 5

Supernova neutrino energy spectrum

The supernova neutrino energy spectrum can be inferred starting from the detection of detector observables. The gain from the reconstruction of the neutrino energy spectrum of a SN burst will be conspicuous.

The 1987A neutrino signal both in water and scintillator detectors led to the best limits on the absolute mass scale of neutrino. These limits were soon exceeded, but other limits on other neutrino properties still stands as the most stringent [72]. For the SN1987A just a few dozen events were recorded, nearly all likely to be electron antineutrinos. The next observed core collapse burst will have much higher statistics and greater flavour sensitivity, which it also means will advance our progress in understanding the internal mechanisms and remnants.

Since the SN1987A burst a lot has been learnt about neutrinos. There are still unknown however, and a future supernova burst may tell us a lot about these unknown. While laboratories measurements will give us all the informations we may need in due time, a timely supernova burst may be the first one to give us some of the answers.

Thanks to experimental measurements of neutrino flavour transition over the past few decades using different detectors and sources we now have a robust model of neutrinos. The three-flavour neutrino model comprises three massive neutrino states connected to the three flavour states by a 3 x 3 unitary mixing matrix,

$$|\nu_f\rangle = \sum_{i=1}^N U_{fi}^* |\nu_i\rangle \quad (5.1)$$

where:

$$U = \begin{pmatrix} 1 & 0 & 0 \\ 0 & c_{23} & s_{23} \\ 0 & -s_{23} & c_{23} \end{pmatrix} \begin{pmatrix} c_{13} & 0 & s_{13}e^{-i\delta} \\ 0 & 1 & 0 \\ -s_{13}e^{-i\delta} & 0 & c_{13} \end{pmatrix} \begin{pmatrix} c_{12} & s_{12} & 0 \\ -s_{12} & c_{12} & 0 \\ 0 & 0 & 1 \end{pmatrix} \quad (5.2)$$

in which s_{ij} is considered the sine of the mixing angle θ_{ij} and c_{ij} is the cosine of it. The

Parameters	Value, 3σ range, any MO	Experimental Information
θ_{12} ($^\circ$)	31.29 \rightarrow 35.91	Solar, Reactor
θ_{23} ($^\circ$)	38.3 \rightarrow 53.3	Atmospheric, beam
θ_{13} ($^\circ$)	7.87 \rightarrow 9.11	Reactor, beam
δ	0 \rightarrow 360	Beam
Δm_{21}^2 (eV^2)	$(7.02 \rightarrow 8.09) \times 10^{-5}$	Solar, reactor
Δm_{3l}^2 (eV^2)	$(2.325 \rightarrow 2.599) \times 10^{-3}$ (NMO) $(-2.590 \rightarrow -2.307) \times 10^{-3}$ (IMO)	Multiple, including supernova

Table 5.1: Three-flavor neutrino oscillation parameter status, from [73].

parameter of interest are the three mixing angles θ_{12} , θ_{23} and θ_{13} and a complex phase δ associated with a CP-violating observables, together with the three masses m_1 , m_2 and m_3 . The mass information is available thanks to oscillation experiments as mass-squared difference $\Delta m_{ij}^2 \equiv m_i^2 - m_j^2$.

Tab. 5.1 summarizes our knowledge of the mixing parameters from the global fit described in [73]. While an improvement of all neutrino mixing parameters will be very welcomed, there are still two quantities that are largely unknown, and only some statistically-weak information are provided about them from beam and reactor data. The first big question in neutrino field, is the 'mass ordering' (MO) or 'mass hierarchy', equivalent to the signs of the mass differences. For 'normal mass ordering' (NMO), is considered m_3 much larger than m_1, m_2 , or two light and one heavy state. For 'inverted ordering' (IMO), it is m_1, m_2 much larger than m_3 . The overall absolute mass scale is also unknown (although it is known to be less than a few eV/c^2), but this parameter cannot be addressed by oscillation experiments. Another quantity largely unknown at the current time is the δ parameter associated with CP-violation observables. This information will be difficult to get from a supernova burst observation.

There are different way to investigate the mass ordering experimentally. In long-baseline experiments is to look at neutrino and antineutrino muon to electron flavor information. JUNO approach is to look for subtle spectral modulations in reactor neutrino spectra [50].

A core-collapse supernova observation is a possibility that with any chance of good luck, could yield knowledge of the mass ordering. There is some model dependency, but there are also model-independent signatures.

The neutrino spectrum at a given time can be reasonably well approximated for each flavor by the following 'pinched thermal' functional form:

$$\Phi(E_\nu) = N_0 \frac{(\alpha + 1)^{\alpha+1}}{\langle E_\nu \rangle \Gamma(\alpha + 1)} \left(\frac{E_\nu}{\langle E_\nu \rangle} \right)^\alpha \exp \left[-(\alpha + 1) \frac{E_\nu}{\langle E_\nu \rangle} \right] \quad (5.3)$$

where E_ν is the neutrino energy, $\langle E_\nu \rangle$ is the mean neutrino energy, α is a "pinching" parameter, Γ is the gamma function and N_0 is the total number of neutrino emitted. The

flavor time evolution of the emitted fluxes can be effectively described by specifying the three parameters, L , $\langle E_\nu \rangle$ and α as a function of time for $\nu_e, \bar{\nu}_e$, and ν_x .

5.1 Neutrino flavour transition in supernovae

Neutrino flavor transitions are now well established and in supernovae will have the occurrence of flavor-transition driven by three-flavor mixing. Neutrino flavor transition in general depend on both the matter density and the flavor-dependent neutrino number densities, which change with time as the supernova evolves.

Matter effects When neutrinos propagate in matter, we have a regular Mikheyev-Smirnov-Wolfenstein (MSW) effect, or matter effect [74] from neutrino propagation through Sun and Earth. The neutrinos feel a matter potential as a function of radial distance r , $\lambda = \sqrt{2}G_F n_e(r)$, where G_F is the Fermi constant and n_e is the electron density.

The adiabatic case For a slowly varying density and matter potential, a neutrino born in a high density region will propagate adiabatically as a matter eigenstate and exit the supernova in a different mass eigenstate.

Adiabatic conversion in the supernova will result in the following flavor transformation of neutrino exiting the supernova at zero matter density :

$$F_{\nu_e} = F_{\nu_x}^0 \quad (NMO) \quad (5.4)$$

$$F_{\nu_e} = \sin^2 \theta_{12} F_{\nu_e}^0 + \cos^2 \theta_{12} F_{\nu_x}^0 \quad (IMO) \quad (5.5)$$

and,

$$F_{\bar{\nu}_e} = \cos^2 \theta_{12} F_{\bar{\nu}_e}^0 + \sin^2 \theta_{12} F_{\bar{\nu}_x}^0 \quad (NMO) \quad (5.6)$$

$$F_{\bar{\nu}_e} = F_{\bar{\nu}_x}^0 \quad (IMO) \quad (5.7)$$

where $F(\nu_i)$ is the flux of a given flavor ($F(\nu_x)$ represents either way ν_μ or ν_τ and similarly for antineutrinos). From the above equations it can be seen that in the NMO case, the ν_e flavor component of the flux will have a spectrum (typically hotter) corresponding to that of the original ν_x flavor; the $\bar{\nu}_e$ flux will be partially transformed. For the IMO case, the antineutrinos will be fully transformed and the neutrino will be partially transformed.

Non-adiabatic case Neutrino propagation can occur adiabatically in a supernova. However matter transition can also occur non-adiabatically, as the matter potential can exhibit discontinuities associated with shock fronts. If a propagating neutrino meets a matter discontinuity, a neutrino energy dependent level-crossing probability P_H applies [75]. The computation of this probability requires detailed knowledge of the supernova mass density profile. Due to the fact that matter discontinuities travel in space as the shock wave propagates, time and energy-dependent signatures of the shock can be seen in the observed signal, so one could in principle see the shock propagation in the neutrino signal as a time and energy-dependent flavor content modulation.

5.2 Neutrino mass physics from Supernova neutrinos

The burst of neutrinos from a supernova bears information about the neutrino absolute mass scale, given the fact that neutrinos have non-zero masses and hence suffer an energy-dependent time delay. The arrival delay due to the fact that they have to travel from a distance D with respect to the time of arrival of a particle with velocity c for a neutrino of energy E_ν and mass m_ν is:

$$\Delta t = 5.14 \text{ ms} \left(\frac{m_\nu}{\text{eV}} \right)^2 \left(\frac{10 \text{ MeV}}{E_\nu} \right)^2 \frac{D}{10 \text{ kpc}}. \quad (5.8)$$

At the time, roughly $20 \text{ eV}/c^2$ neutrino mass limits based on observed time spread of the SN1987A burst neutrino [72] were competitive with laboratory limits. However, the current best limits from the tritium beta decay endpoint experiments are now about $2 \text{ eV}/c^2$ [76]. For few-tens of MeV massive neutrinos, the delay will be less than tens of milliseconds for a travel distance of 10 kpc. The emission time scale of the burst, which is 10 seconds or so, exceeds the typical delay by a large factor, so one must look for signatures of mass scale in the subtle energy-dependent timing of the arrival pattern. The lower the observed energies are going to be, the longer will be the delay, which also means better sensitivity. Nevertheless sensitivity has a small dependence on distance; as the distance increases, delay increase linearly with D , but observed counts decrease as the inverse squared of D . This is the reason why large statistic, good energy resolution and low threshold are needed.

One of the most promising prospect for determining the MO via a supernova burst is the observation of the neutronization burst in the energy spectrum. This kind of process stands almost like a standard candle; the time dependence of its luminosity is almost model independent [77]: see Fig. 5.1. Its flavor is strongly dominated by ν_e . Because the electron neutrinos escape from regions for which the lepton asymmetry is such that self-interaction has a negligible effect, one expects the burst to be processed by MSW effects only, in a MO-dependent way. This simplifies the interpretation of the signal.

According to Eq. 5.4 and Eq. 5.5, the ν_e flux will swap completely in ν_x in case of NMO. Since there is very little ν_x presence for the entire duration of the neutronization burst, there will be very little ν_e to observe. On the other hand, in case of the IMO the ν_e component will be only partially swapped as it can be seen in Eq. 5.6 and Eq. 5.7. This means the neutronization burst is suppressed in both scenario, but even more strongly in the NMO case. Hence, the signature of NMO is an absent or highly suppressed neutronization burst in a ν_e -sensitive detector, while the signature of IMO is an observable neutronization burst. In Fig. 5.2 is shown an example of neutronization burst (or its absence) in scintillator detector like JUNO.

In this section, the technique adopted to reconstruct the supernova energy spectrum is described. The analysis is performed on the three main supernova burst channels, IBD, proton elastic scattering (pES) and electron elastic scattering (eES) separately. It is also

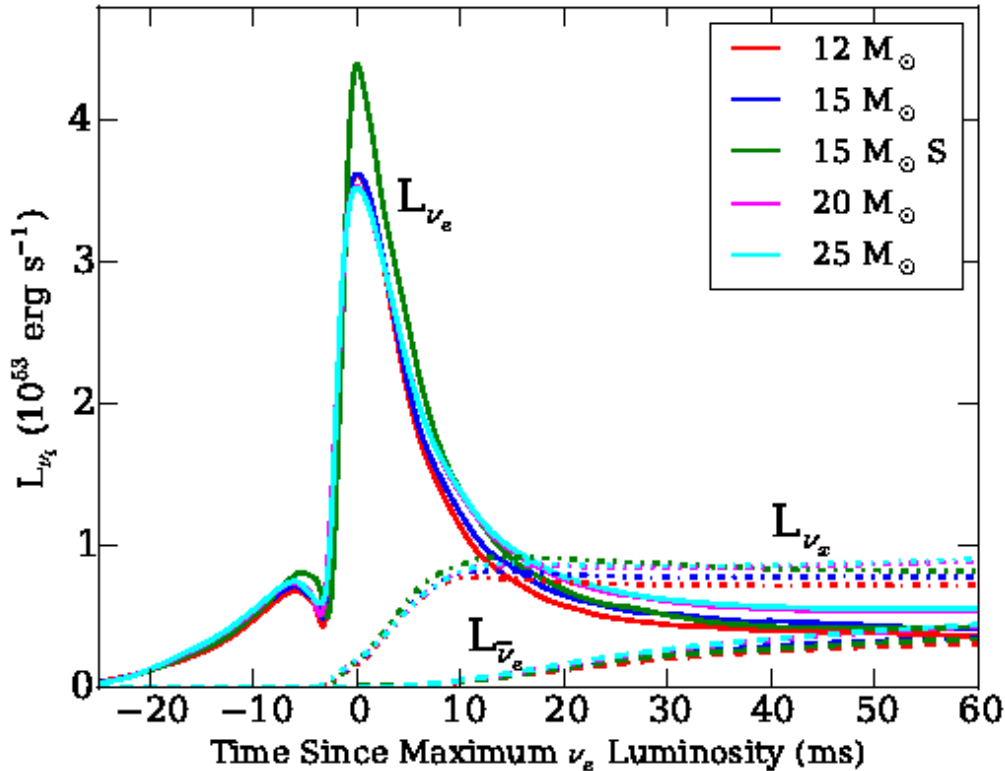


Figure 5.1: Energy luminosity as a function of time for all the three main neutrino channels ($\nu_e, \bar{\nu}_e$, and ν_x) for different progenitors and different equations of state [78]. The solid lines represent the ν_e luminosity, the dashed lines represent the $\bar{\nu}_e$ luminosity and the dot-dashed lines represent the ν_x luminosity

reported an estimation of the uncertainties on the final energy spectrum. The reconstruction first relies on finding a reasonable relationship between the experimental observable and the energy of the neutrinos that interacted inside the detector. The problem is not trivial since the observable are affected by large fluctuations, result of the probabilistic nature of the processes, which regulates the development of the secondary particles. The reconstruction process also has to take into account the efficiency of the detector. In general, the issue of correlating two quantities that do not have a direct relationship but rather a statistical one is expressed through *unfolding* procedures.

5.3 Spectrum Unfolding

The JUNO electronic image of a neutrino events produces different quantities: among those, a fundamental role in case of a supernova burst is played by the integrated charge spectrum of the PMT systems, which can give an estimation of the total energy released by secondary particles. In this study, the charge (Q) as a fraction of the number of photoelectrons (p.e) of the LPMT system is used as a deposited energy estimator. In order to match the effective distribution which is acquired by the DAQ system, the hits in the first

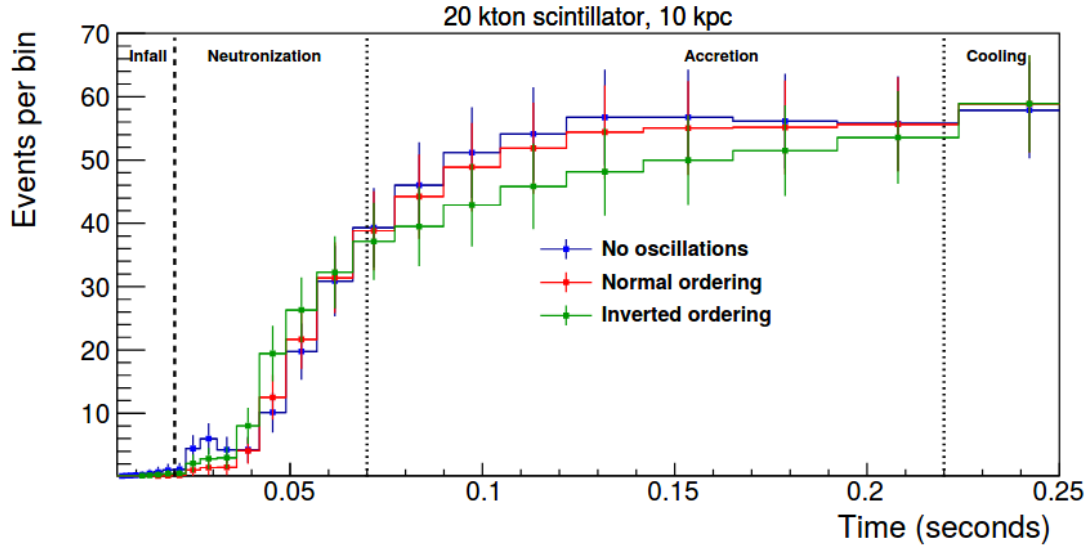


Figure 5.2: Expected event rate from [79] as a function of time for the electron-capture supernova model for 20 kilo-tonnes of scintillator (JUNO-like) during early stages of the event. Shown are the event rate for the case of no flavor transitions (blue), the event rate including the effect of MSW transitions for normal (red) and inverted (green) hierarchies. Error bars are statistical.

$1.2\mu\text{s}$ are considered. From a set of data, the charge distribution spectrum is produced and can be expressed as it follows:

$$N(Q(p.e.)) = \int \Phi(E_\nu) A_{eff}(E_\nu, Q(p.e.), \Omega, T, ..) \varepsilon(T, Q(p.e.)) dE d\Omega dT, \quad (5.9)$$

where T is the acquisition time, Ω is the solid angle which defines the detector acceptance, ε is the detector efficiency and A_{eff} is the effective area for the event detection. The value of primary neutrino flux $\Phi(E_\nu)$ is evaluated according to the hypothesis above, by comparing the measured spectrum with theoretical predictions which undergo the same reconstruction process. An unfolding method is adopted in this study to reconstruct the primary energy spectrum. The advantage of this kind of method is that the unfolded flux is directly comparable to the observable one, without any assumptions on the primary distribution. The observable spectrum M_j is therefore unfolded into the true neutrino energy spectrum N_i , where the indexes i and j denote respectively the binning of the n_E causes ($i=1, \dots, n_E$) and the n_M effects ($j=1, \dots, n_M$). Concerning the observable distribution the binning has been defined as it follows:

- **IBD** sample: 7 bins equally spaced in $Q(p.e.)$, from 20×10^3 to 90×10^3 .
- **pES** sample : 5 bins equally spaced in $Q(p.e.)$ from 0. to 3×10^3 .
- **eES** sample: 7 bins equally spaced in $Q(p.e.)$ from 1×10^3 to 20×10^3 .

while the unfolded spectrum binning is defined :

- **IBD** sample: 6 bins equally spaced in $E(E_\nu/\text{MeV})$, from 10.0 to 40.0
- **pES** sample : 5 bins equally spaced in $E(E_\nu/\text{MeV})$, from 25.0 to 50.0
- **eES** sample : 5 bins equally sapced in $E(E_\nu/\text{MeV})$, from 2.0 to 15.0

Analysing the problem under its probabilistic nature, will bring us to try to rank in probability all possible spectra that might have caused the observed one. The observable spectrum can be expressed in terms of the primary spectrum which originated the events:

$$M_j = \sum_i L_{ji} N_i \quad (5.10)$$

where L_{ji} is the detector likelihood matrix, which can also be identified as the conditional probability that when a neutrino with a certain energy arrives a certain amount of charge Q will be collected : $L_{ji} = P(Q(p.e)|E_{\nu_i})$. The L_{ji} matrix is estimated from the MC and represents the detector response. Eq. 5.3 can be inverted so to express the primary energy spectrum as below:

$$N_i = \sum_j U_{ij} M_j \quad (5.11)$$

where the U_{ij} is the so-called unfolding matrix, which can also be expressed in terms of conditional probability that an event which brought to collect a certain amount of charge Q , originated from a neutrino with a certain energy E_{ν_i} : $U_{ij} = P(E_{\nu_i}|Q(p.e.))$. There are quite different ways to retrieve the unfolding matrix and in doing so the original spectrum; in this case thou, since we are taking into account a probabilistic relationship within the causes and the effects, a linear and algebraic inversion will not fit the purposes.

5.4 Bayes Unfolding

The iteration in question is based on an iterative application of the Bayes' Theorem. So if the Bayes'theorem is written in terms of independent *causes* ($C_i, i=1,2,\dots,n_c$), which can produce n_E possible effects, it will then be:

$$P(C_i|E_j) = \frac{P(E_j|C_i)P_0(C_i)}{\sum_{l=1}^{n_c} P(E_j|C_l)P_0(C_l)} \quad (5.12)$$

Once this has been established, the unfolding matrix U can be evaluated [80, 81]. The detector response matrix is evaluated using a full MC sample and it can be normalized as $\sum_j L_{ji} = 1 - \varepsilon$, where ε takes into account the inefficiency due to the reduced phase considered by the matrix and the wrong-flavor are included in L_{ji} . The result will be bringing the following expression for the unfolding matrix:

$$U_{ij} = \frac{L_{ji}P(E_{\nu_i})}{P(Q_{LPM}^{CD})} = \frac{L_{ji}P(E_{\nu_i})}{\sum_{k=1}^{n_E} L_{jk}P(E_{\nu_k})} \quad (5.13)$$

where $P(E_{\nu_i})$ is the probability to observe a neutrino with energy E_{ν_i} , which is exactly the quantity to be measured. Once the initial prior is defined, $P_0(E_{\nu_i})$, the estimation of the neutrino flux can be carried out through Eq. 5.3.

A minimum effect is carried by the shape of the prior distribution. Possible bias effects are taken into account into the evaluation of the uncertainties. Despite everything, the prior should, of course reflect the best knowledge of the primary spectrum, so that the minimum bias is achieved by adopting the true MC distribution. A little point to stress out is that as prior a particular flat spectrum is used, and the posterior probability could be affected from it. To solve this problem and improve if necessary the estimation of the energy distribution, a series of iterations can be implemented: through these the initial unfolded distribution is used to build a new prior, which generates new conditional probabilities, to eventually update the unfolded spectrum. Of course a high number of iterations enhances the statistical fluctuations on the data sample and may affect the shape of the unfolded spectrum [81]. The effect of the particular shape of the prior distribution is in general small and can influence the number of iterations needed [81].

The iterative Bayesian method is strongly data-driven and in this work is performed one iteration. As prior distribution, the one dimensional Garching Model for CCSN is used [64]. The fluxes values at the i -th bin center are obtained by interpolation and the prior is normalized to unity, according to probability laws. In Fig. 5.3, Fig. 5.4 and Fig. 5.5 are shown the unfolding matrices for each of the three main channel for a SN burst in JUNO, IBD, pES and eES.

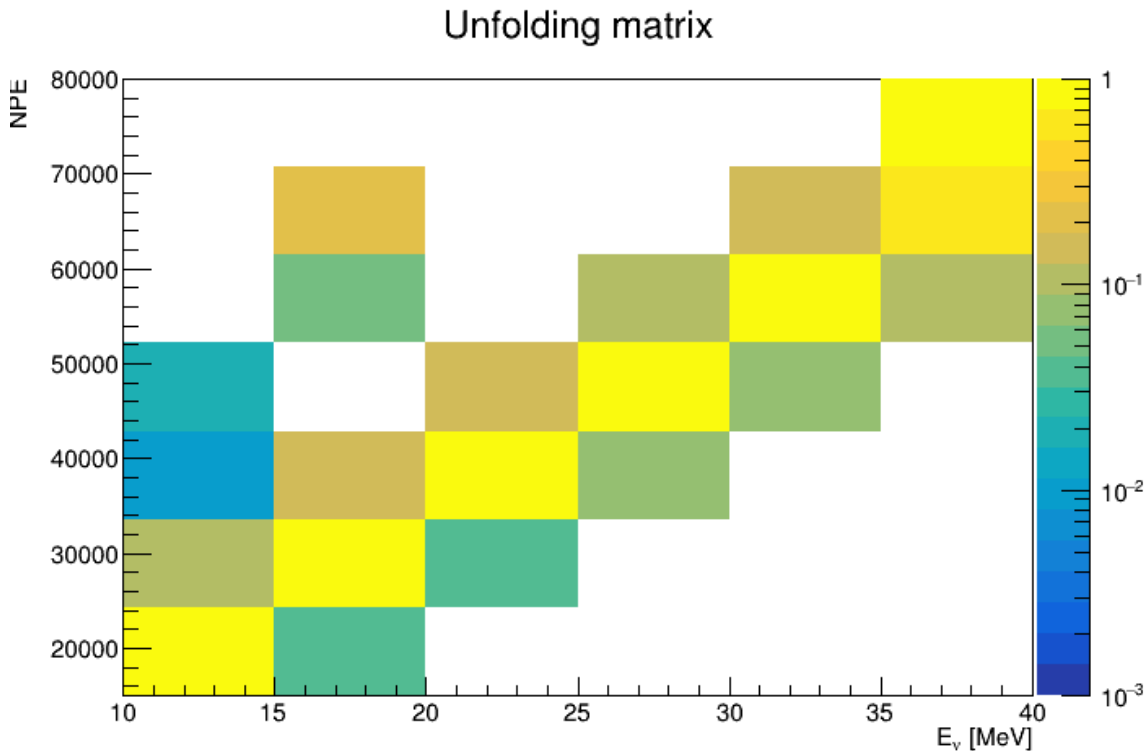


Figure 5.3: Detector response matrix for the IBD channel of the Garching Model

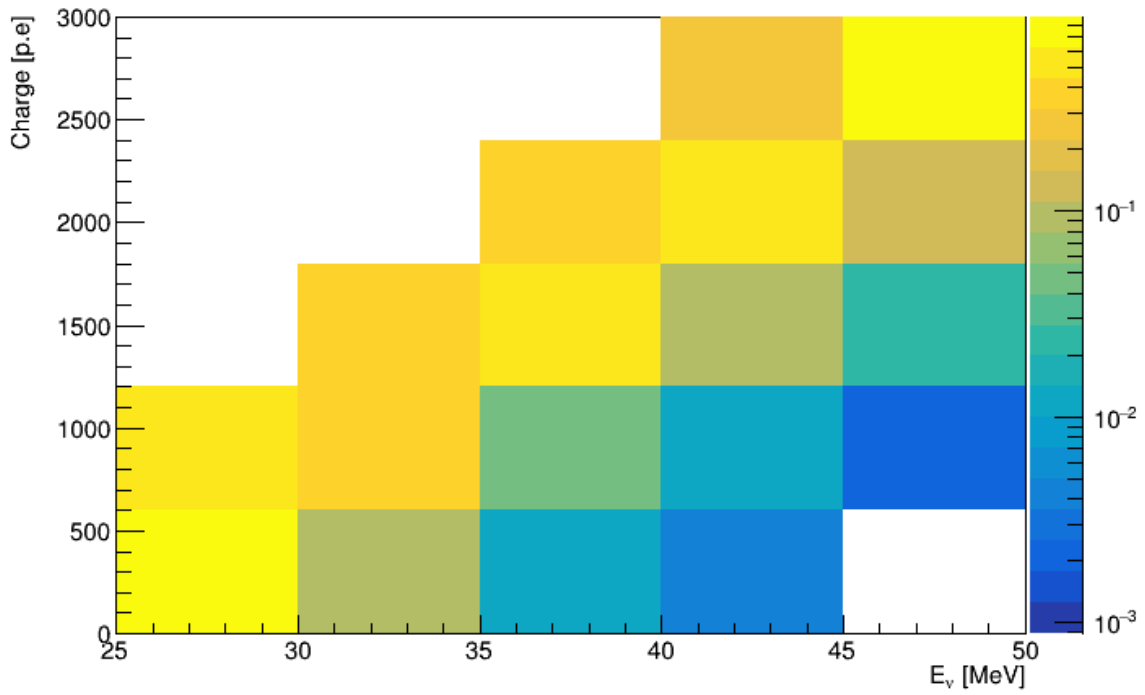


Figure 5.4: Detector response matrix for the pES channel of the Garching Model

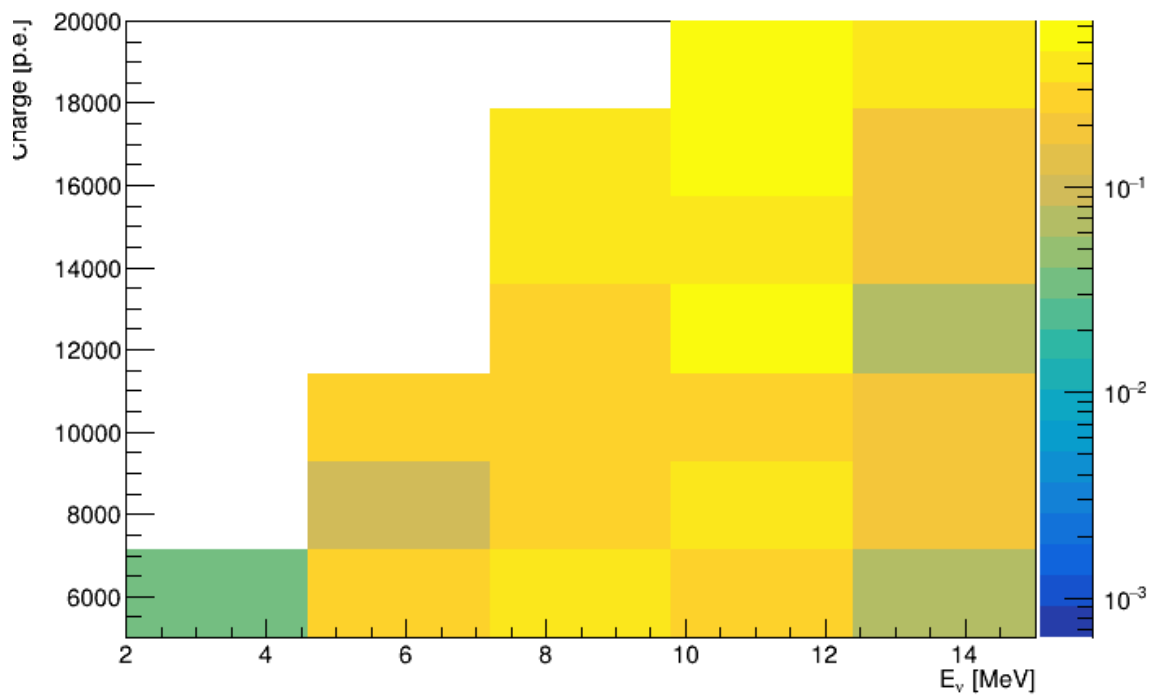


Figure 5.5: Detector response matrix for the eES channel of the Garching Model

5.4.1 Simulated data sample

As already clarified, to prove the JUNO performances in reconstructing the SN neutrino flux, the fake data come from an independent MC sample, as preempted in Section. 3. The sample represents a CCSN burst of a $20M_{\odot}$ at 10 kpc following NMO and with full set of opacities for the Garching Group Model, and a $13 M_{\odot}$ at 10 kpc, with a metallicity of 0.02 and with 300 ms of shock revival time for the Nakazato Model. For illustration in here is reported the Garching Model, the Nakazato distributions can be found in the **Appendix**. The sample has been selected and separated in the three main detection channels, as described in Section 3. Tab. 5.2 summarize the population for each flavor and for cuts, while the event distribution of the sample after the full selection chain is reported as a function of the observable, Charge[p.e], in Fig. 5.6, Fig. 5.7 and Fig. 5.8. In case of the elastic scattering on electrons the residual background from other flavors is quite high, so the application of the same cut of the first two channel has to be improved with some other discrimination tool, such a pulse shape discrimination to distinguish between positron and electrons. Nevertheless, despite this quite high contribution from other neutrino flavors, the strength of the bayesian method is proved. In fact thanks to the proper definition of the probabilities, the Bayes theorem allows the spectrum unfolding even in presence of a disadvantageous signal-to-noise ratio.

# events	IBD	pES	eES
Before Selection	9493	1155	374
After Selection	4368	1104	208
Residual Background	583	103	1084

Table 5.2: Summary of the selected sample for IBD, pES and eES before and after the fiducial and selection cuts in terms of number of events. Also the number of events of the wrong flavour is reported.

With all the cuts the signal efficiency for the IBD events is about 89.1% with a residual background of about 4%. The signal efficiency for the pES is order of 80 % with a residual contamination of about 1%. Due to their nature instead, the eES channel is high contaminated by other flavors, as expected.

5.5 Reconstructed Flux

In this section the reconstructed flux for IBD, pES and eES obtain from the *fake-data* sample is reported. The predicted Garching flux is also reported in the chosen bins, including the flavor conversion effects.

For illustration the unfolding procedure on the IBD channel is hereby presented in Fig 5.12 for each of the progenitor masses present in the Garching Model in the JUNO framework. The uncertainties here considered are both statistical and a first evaluation of

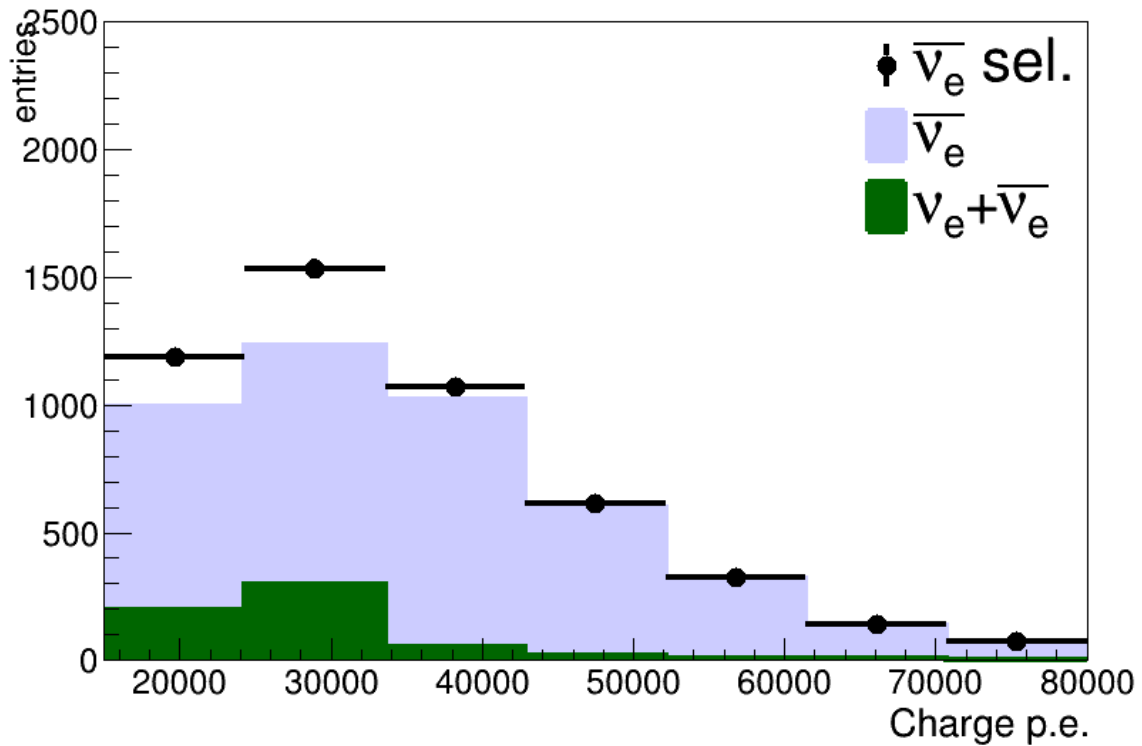


Figure 5.6: Distribution of the reconstructed Charge observed, as a function of the p.e. in each selection bin, for the IBD channel. The black dots are the selected event in every bin, with statistical errors. The histograms represent the bin composition in terms of correct flavor (light blue) and wrong one (green)

the systematic uncertainties, which dominates the contributions and bring a contribution not larger than 20 %. As final result it is reported the whole flux reconstruction with all three main interaction channels included and their statistical contributions, for the three different energy ranges in Fig. 5.13

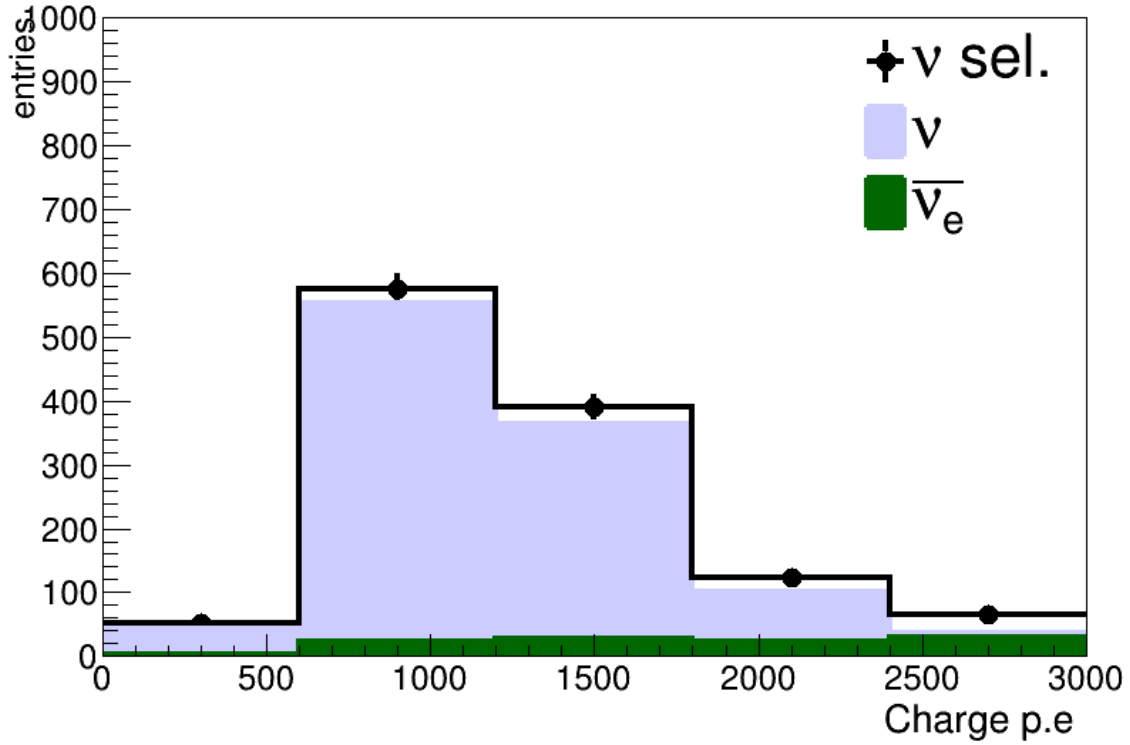


Figure 5.7: Distribution of the reconstructed Charge observed, as a function of the p.e. in each selection bin, for the pES channel. The black dots are the selected event in every bin, with statistical errors. The histograms represent the bin composition in terms of correct flavor (light blue) and wrong one (green)

5.6 Uncertainties evaluation

In order to evaluate the total uncertainties several contributions have to be taken into account in each measured bin. Both statistical and systematic uncertainties have to be evaluated. For what concerns the systematic, the contribution coming from the analysis cuts has been evaluated.

Statistical Uncertainties

The statistical uncertainties are due to stochastic fluctuations which occur in data bins. The result of this fluctuations is shown in Fig. 5.6, 5.7 and 5.8 for each observable bin. In order to evaluate their contribution on the final unfolded spectrum, 1000 toy pseudo-data have been generated, changing the bin content each time according to the Poissonian distribution. The final distribution in the unfolded spectrum (Fig. 5.14, Fig. 5.15 and Fig. 5.16) is then fitted with a gaussian function, whose σ is used to quote the statistical uncertainties.

The contribution goes from 5% in the bins with highest statistics to 10% in the highest-energy bins.

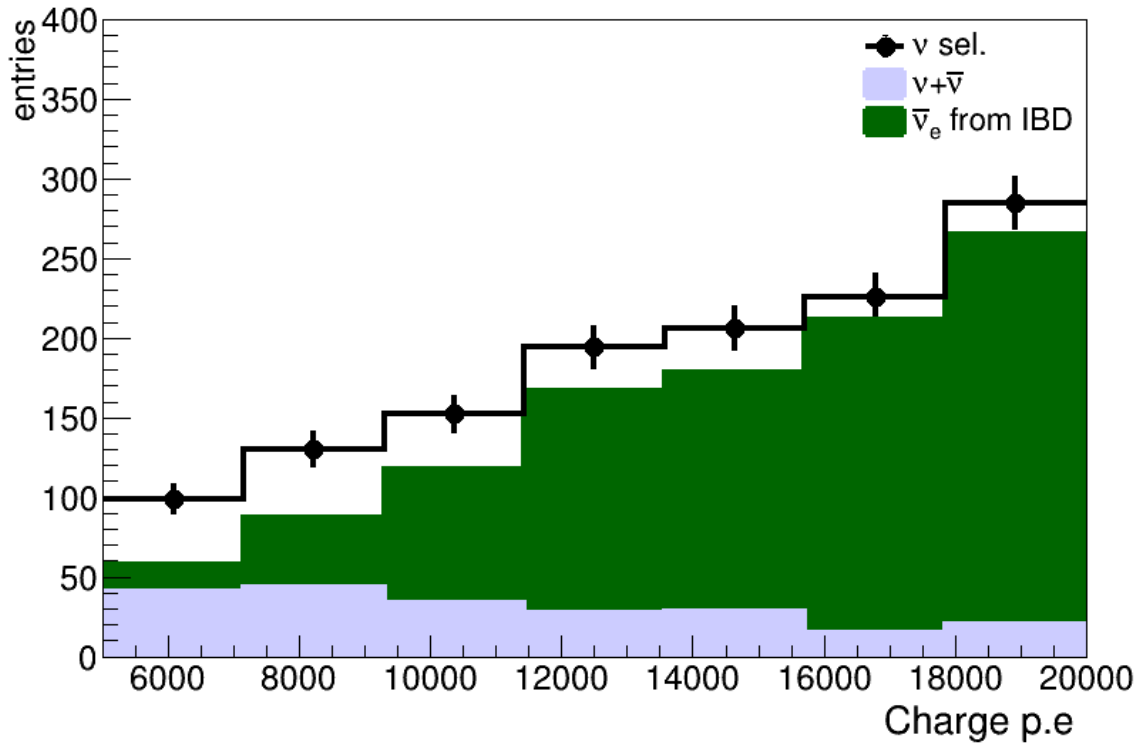


Figure 5.8: Distribution of the reconstructed Charge observed, as a function of the p.e. in each selection bin, respectively for the eES channel. The black dots are the selected event in every bin, with statistical errors. The histograms represent the bin composition, respectively in terms of the correct flavour (light blue) and the wrong one (green).

Effects of the selection criteria The selection procedure on the detection channel is in general produced not to produced any bias on the final sample. As already explained before, fiducial cuts consist on quality selections applied on the neutrino sample. Their effects can be seen in Fig. 4.7, 4.8. This means the final selected spectra reflects well those cuts and it is well contained into the interval, so that those do not affect the reconstruction of the flux. Although the vertex cuts does not affect the reconstruction, the cut on the integrated charge could introduce some inaccuracies in those bins in which the statistical becomes low. The analysis has been performed by varying each time the nominal cut value in a range $[20 \times 10^3 - 90 \times 10^3]$ for the IBD, $[0. - 3 \times 10^3]$ for pES and $[1 \times 10^3 - 20 \times 10^3]$ for the eES. Due to the high uncertainties already coming from the provided models for a SN explosion, a confidence level of a 1σ has been identified to express the systematic coming from this procedure. The results is shown in Fig. 5.17, Fig. 5.18. The major differences in the unfolded flux are relevant in the bins with less statistics for the reasons already explained.

Uncertainties Summary As it is noticeable the uncertainties are quite significant in both statistical and systematic contribution on the edge bins, which represents the ones with less statistics. The fiducial cuts inflict a repercussion on both statistics and systematic, setting up bigger uncertainties. Especially in the last bin, a fiducial cut on the

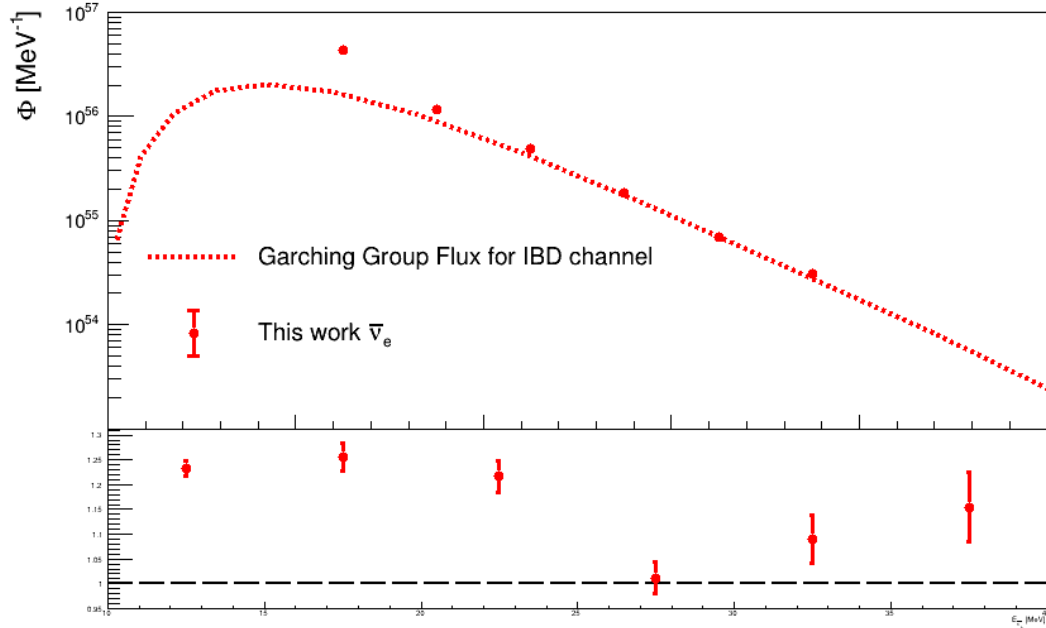


Figure 5.9: Reconstructed energy spectra for IBD channel. The error bars represent statistical contributions discussed in Section 5.6. Also the flux prediction from the model is reported

observable reduce abundantly the number of events, making difficult to evaluate the first and the last bin completely. On top of that, in respect of the original flux, the last bin is on the tail of the distribution, where the rate is decreasing. The total flux uncertainties here considered ranges from 10-15% in the middle region of the spectrum (\mathcal{O} 15- 30 MeV) up to 50 % in the edge bins.

5.6.1 Background

The background rated estimated for supernova neutrino events can vary in species and can vary because of the detector location and type, as well as the signal channel. Generally speaking background are not a very high concern for SN neutrino burst, because it lasts only around 10 s. Possible background for a given signal are natural radioactive sources, which is less than 10 Hz at energy larger than 0.7 MeV, cosmic backgrounds (roughly 3 Hz of muon rate in JUNO LS), the SN neutrino themselves. IBD Reactor neutrinos and geo-neutrinos also contribute as backgrounds. In a 10 s range there will be 0.01 IBD from reactors and 0.0002 IBD from geo-neutrinos, which is completely negligible for any detectable SN. Other source like low-energy atmospheric neutrinos, natural radioactivities and cosmogenic are even smaller. It has to be considered with more care the background for the elastic neutrino-proton scattering, since they are the singles of low-visible energy

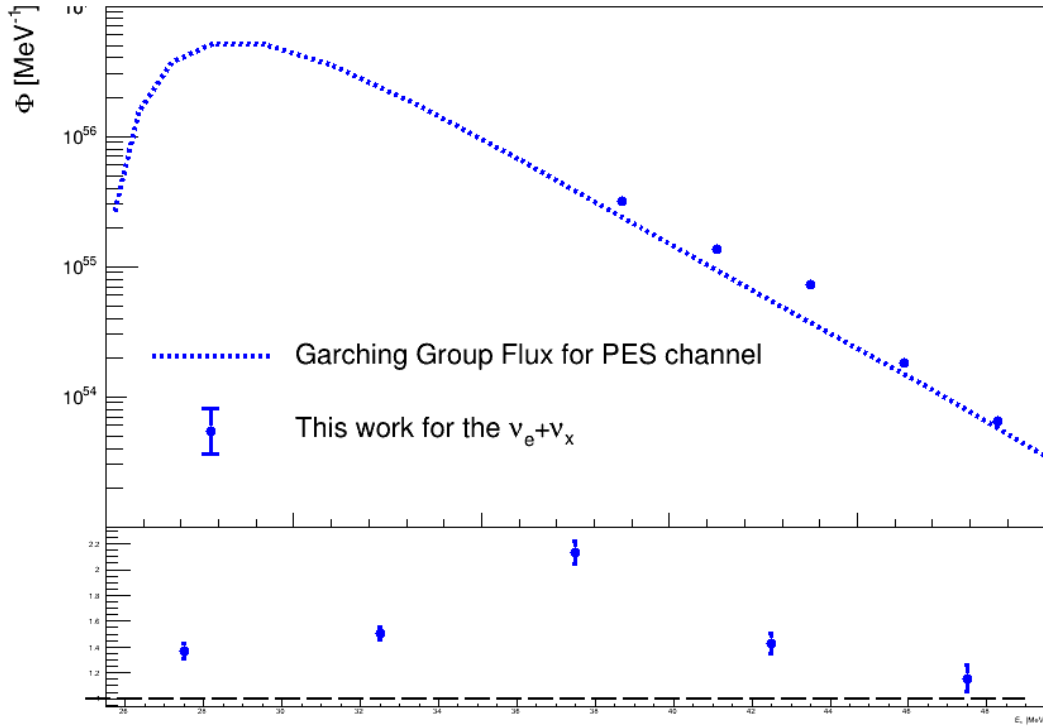


Figure 5.10: Reconstructed energy spectrum for pES channel. The error bars include all statistical contributions further discussed in Section 5.6. Also the flux prediction from the model is reported [64].

and the quenching factor is JUNO LS is about 0.2 MeV. The background rates of β decays arising from ^{85}Kr and the lead-daughter are respectively about 10 events for the first one and around 70 events for the latter. Even assuming low spectral energy range for SN neutrinos, the proton recoil signal would be dominating by at least one order of magnitude. The neutrino-electron scattering has similar contributions to the previous elastic scattering already considered, but has higher visible energy since the quenching effect for electrons is small. This background can be therefore reduced by selecting an appropriate range of energy for the events.

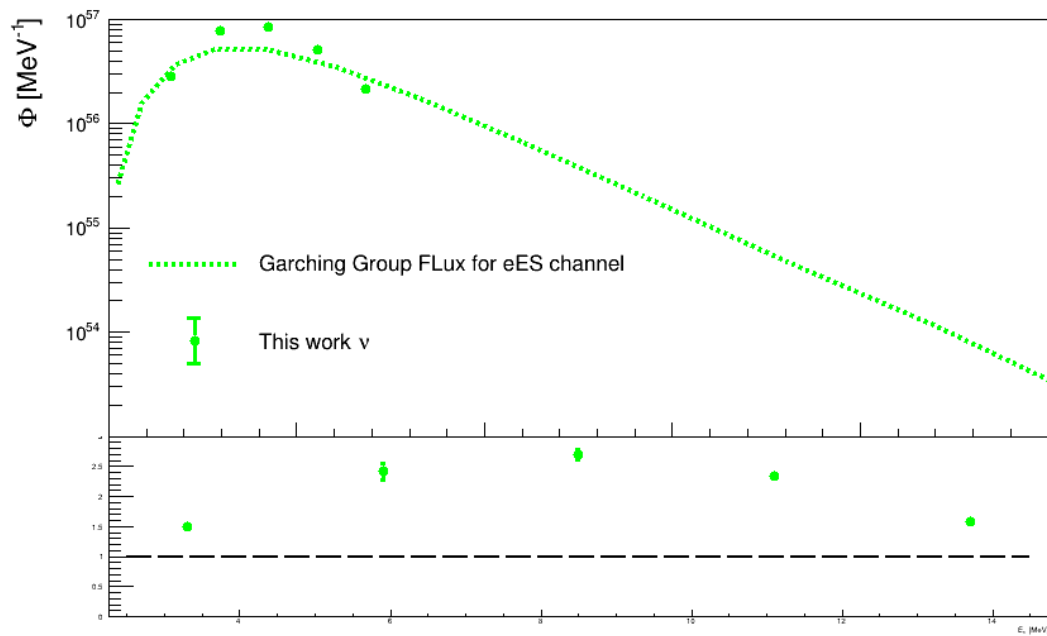


Figure 5.11: Reconstructed energy spectra for eES channel. The error bars represent statistical contributions discussed in Section 5.6. Also the flux prediction from the model is reported

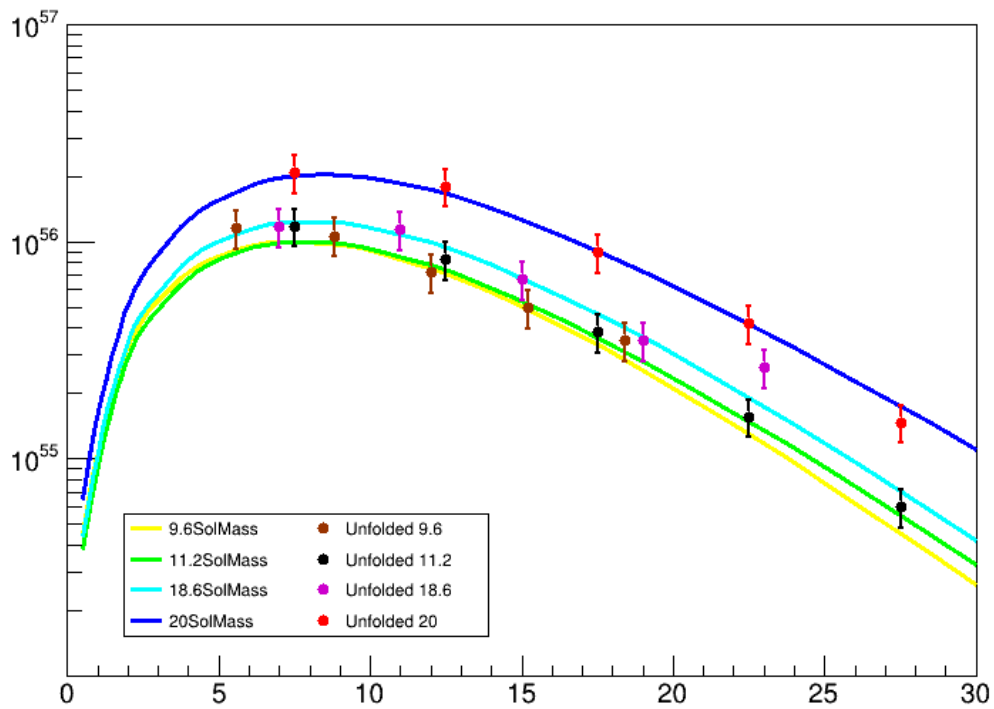


Figure 5.12: Unfolded energy spectrum for each mass progenitor present in the Garching Model for the IBD channel. The dots represent the simulated data sample with the statistical uncertainty associated. The lines are the theoretical flux provided by the model. The yellow line is the $9.6 M_{\odot}$ flux, and brown dots, its data sample; the green line is the $11.2 M_{\odot}$ and the black dots its data sample; the light blue line the $18.6 M_{\odot}$ with its magenta data points and at last the blue line is the $20 M_{\odot}$ with the red dots representing its data sample.

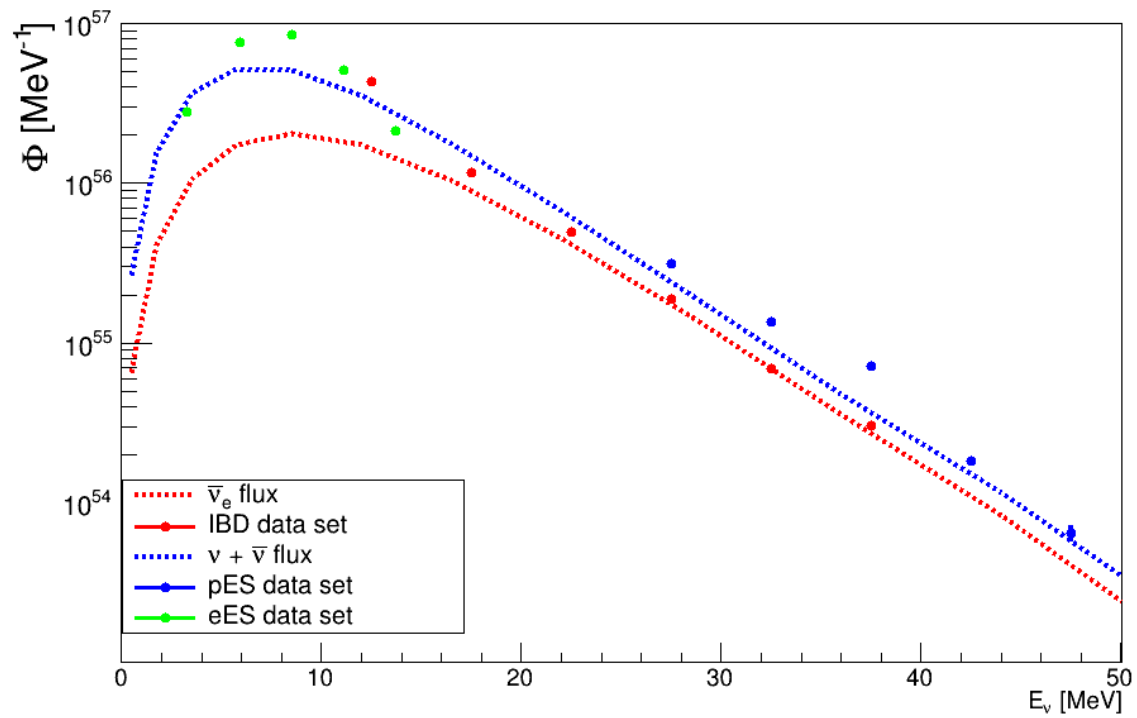


Figure 5.13: Unfolding of the whole supernova energy spectrum for a $20 M_\odot$ at 10 kpc for the Garching model with all three main channels included: in red the IBD data set and the corresponding $\bar{\nu}_e$ flux in dashed red line; in blu the pES data set and in green the eES data set unfolded and the dashed blu lines is the $\nu + \bar{\nu}$ flux, excluding the $\bar{\nu}_e$ flux treated separately.

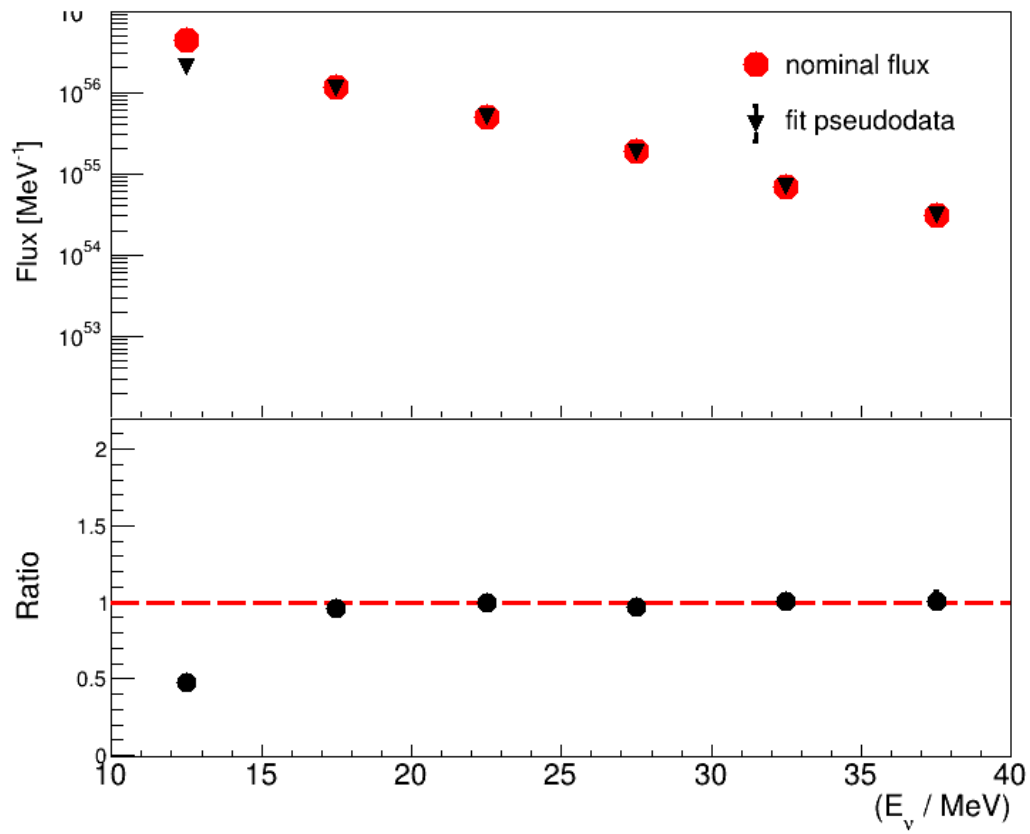


Figure 5.14: *Upper panel:* Unfolded spectrum and gaussian fit on pseudo data from stochastic fluctuation (black triangle); *Bottom panel:* fit-unfolded spectrum ratio, with corresponding uncertainties, for the IBD channel.

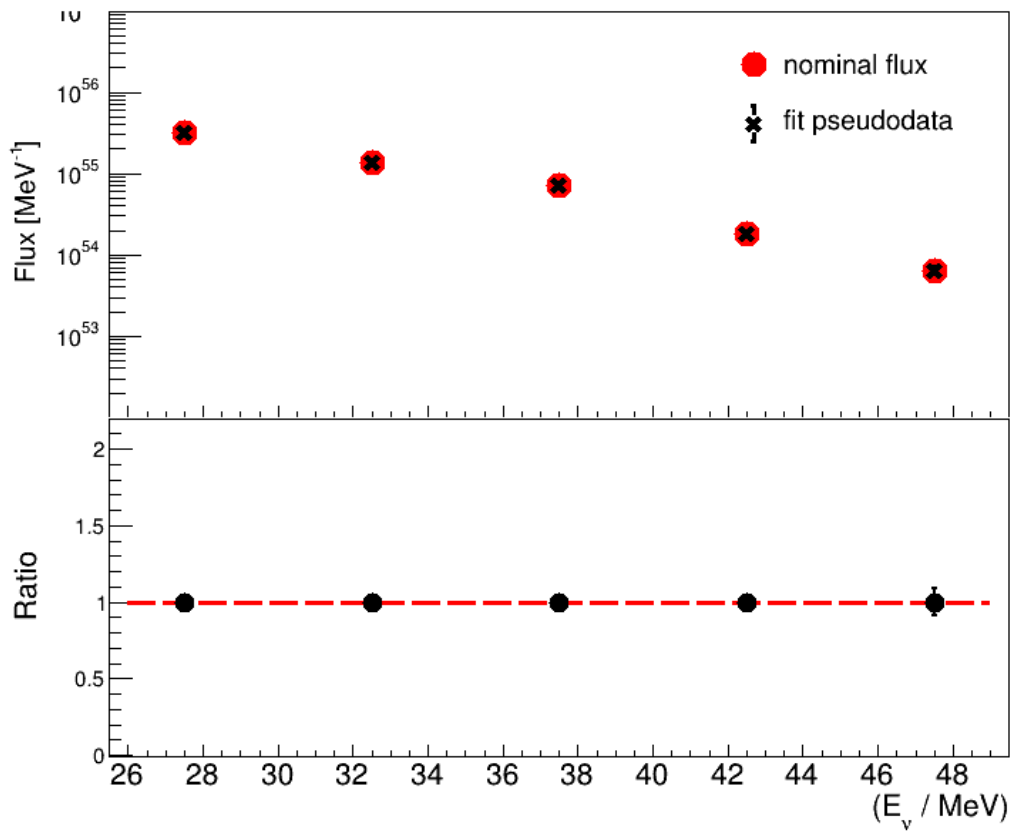


Figure 5.15: *Upper panel:* Unfolded spectrum and gaussian fit on pseudo data from stochastic fluctuation (black crosses); *Bottom panel:* fit-unfolded spectrum ratio, with corresponding uncertainties, for the pES channel.

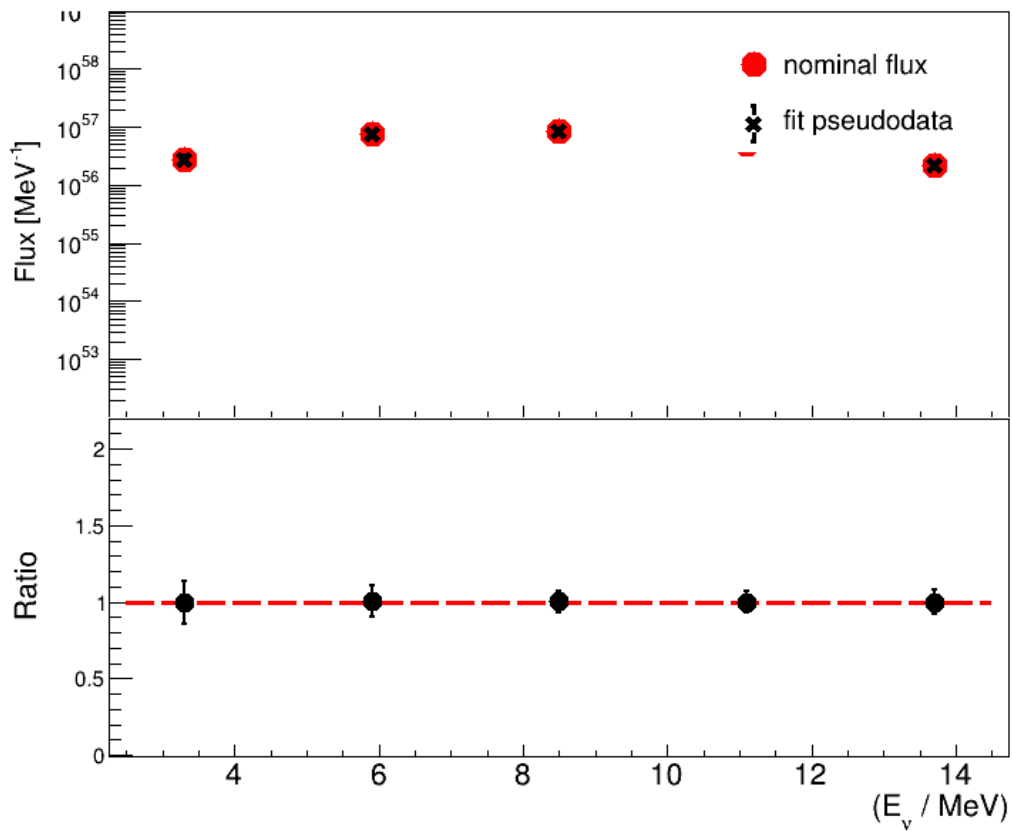


Figure 5.16: *Upper panel:* Unfolded spectrum and gaussian fit on pseudo data from stochastic fluctuation (black crosses); *Bottom panel:* fit-unfolded spectrum ratio, with corresponding uncertainties, for the eES channel.

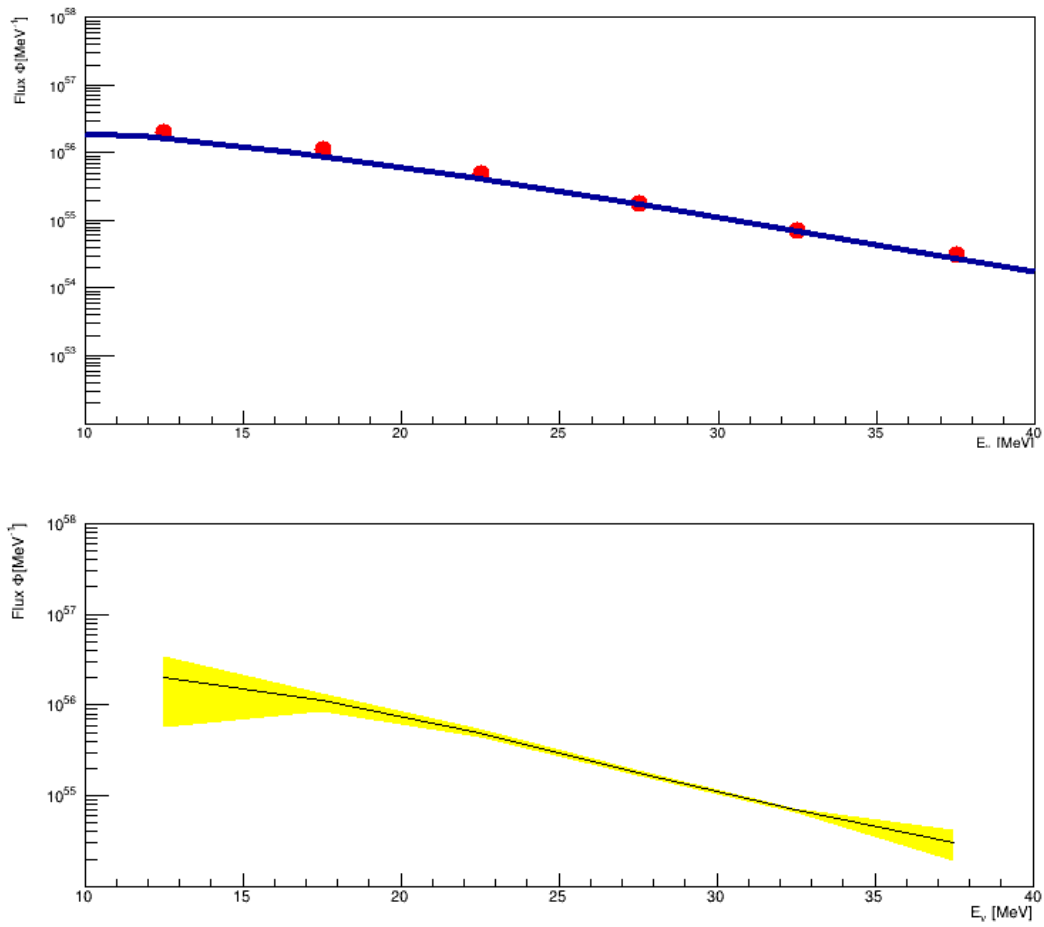


Figure 5.17: *Upper panel:* Unfolded spectrum for the nominal cut value; *Bottom panel:* 68 % confidence level, within which is lie the maximum possible variation of the unfolded flux for the IBD channel

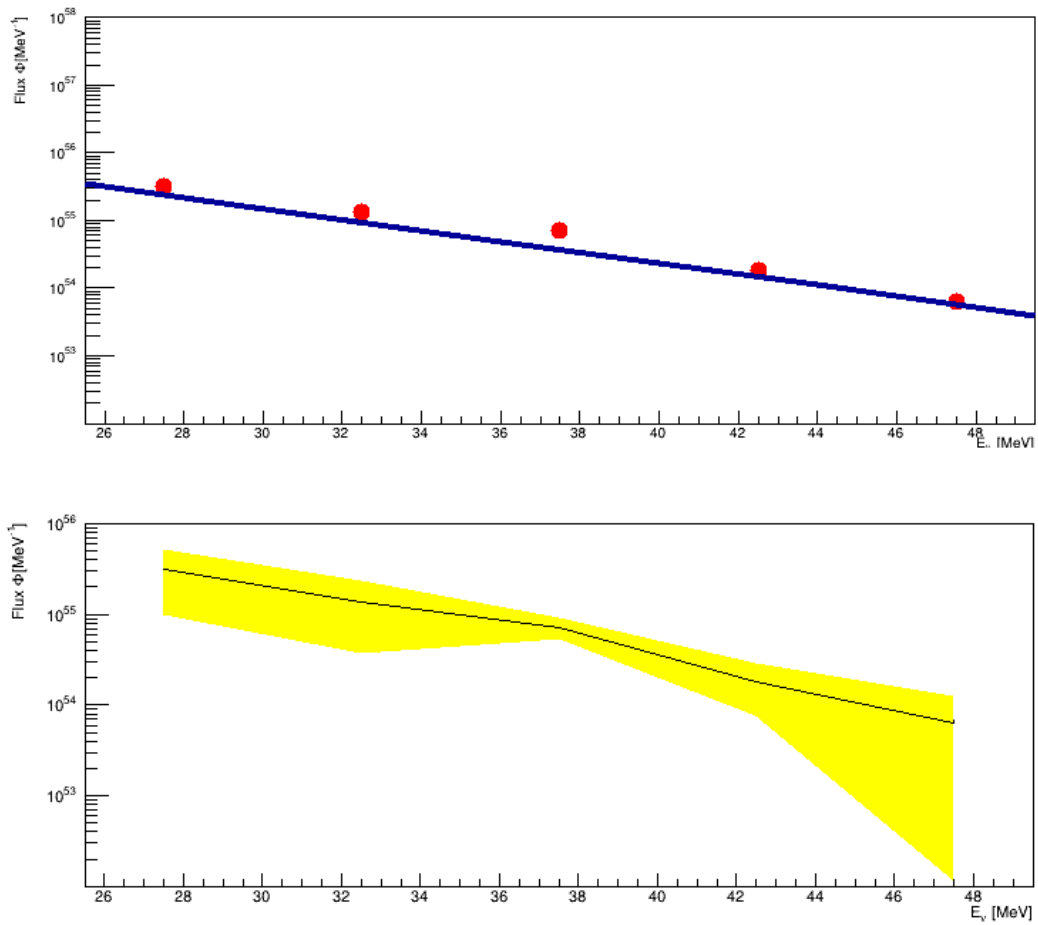


Figure 5.18: *Upper panel:* Unfolded spectra for the nominal cut value; *Bottom panel:* 68% confidence level, that indicates the maximum possible variation of the unfolded flux for the pES channel

Chapter 6

Progenitor Mass Reconstruction

CCSNe have significant impact in different areas of astrophysics including chemical enrichment of the interstellar medium and galaxies, triggering of star formation and release of energy into their surroundings, and in addition in some areas of particle physics through neutrino emission. With the amount of data that JUNO will be able to collect from a SN explosion, it will, have as said in other chapters, great capabilities in the number of events recorded and the analysis it can be done with it. In this chapter we present a probabilistic analysis done thanks to a chosen observable to retrieve the progenitor Mass star. In order to do this, the time distributions of the events in the detector have been studied for each supernova explosion, which depends on the events rate, with the purpose of identifying a proper observable for the analysis. This observable has been identified with the peak time of the distribution, in which the majority of the events are concentrated. Having a look at the Energy Integrated neutrino flux (ENF), for both models in this study, the distributions in Fig. 6.1 and Fig. 6.2

The distributions under studying represent the first 4 seconds of the ENF, in Fig. 6.1 the Garching Model, in purple the $27 M_{\odot}$, in light blue the $25 M_{\odot}$, in green the $18.6 M_{\odot}$, in red the $11.2 M_{\odot}$ and in blue the $9.6 M_{\odot}$; in Fig. 6.2 the Nakazato Model, for the only three Mass progenitors available in the JUNO simulation framework, in red the $30 M_{\odot}$, in blue the $20 M_{\odot}$ and in green the $13 M_{\odot}$. All the SN are simulated at a fixed distance of 10 kpc. From those plot it can be noticed that they all differ from the peak of the distribution, since the event rate changes accordingly with the SN progenitor mass. The time of the peak has been set out as the observable for the probabilistic analysis. Once the observable has been set, the first step is to look for a relationship between the time of the peak and the progenitor mass. This has been found thanks to several different independent simulation of the same SN to look at the variation of the peak time for each SN burst. 20 SN burst have been simulated for each mass progenitor for each model.

By averaging over all the peak times obtained for each simulation, it was possible to obtain a functional form of the mass as a function of the time, and fit it with a logarithmic function.

Considering that in case of a SN explosion only one time corresponding to the peak

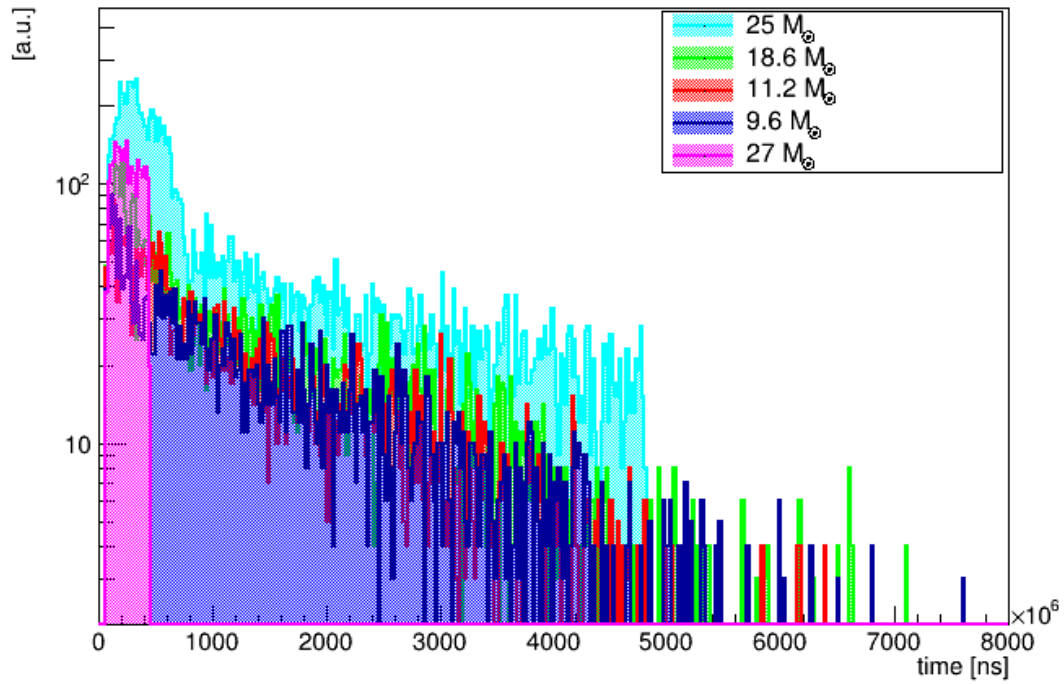


Figure 6.1: Energy Integrated neutrino flux for all the Mass progenitors provided by the Garching group

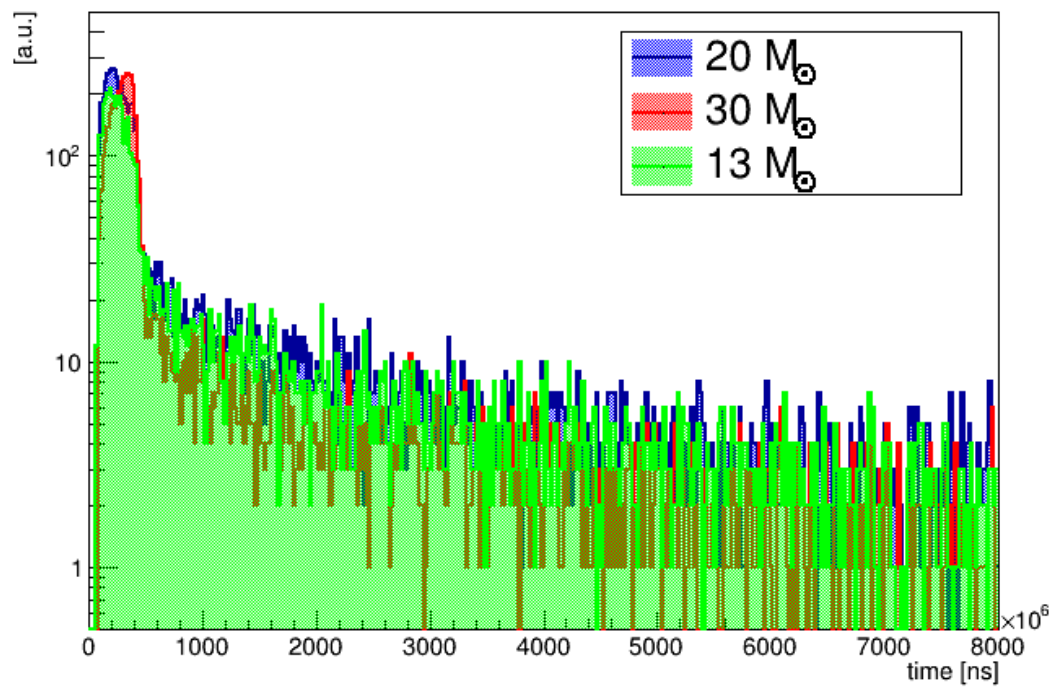


Figure 6.2: Energy Integrated neutrino flux for all the Mass progenitors provided by the Nakazato model

of the ENF will be available, for a probabilistic evaluation, a TOY Model has been built, based on the found functional form.

As expected for the Nakazato model the fit is less indicative due to the lack of points

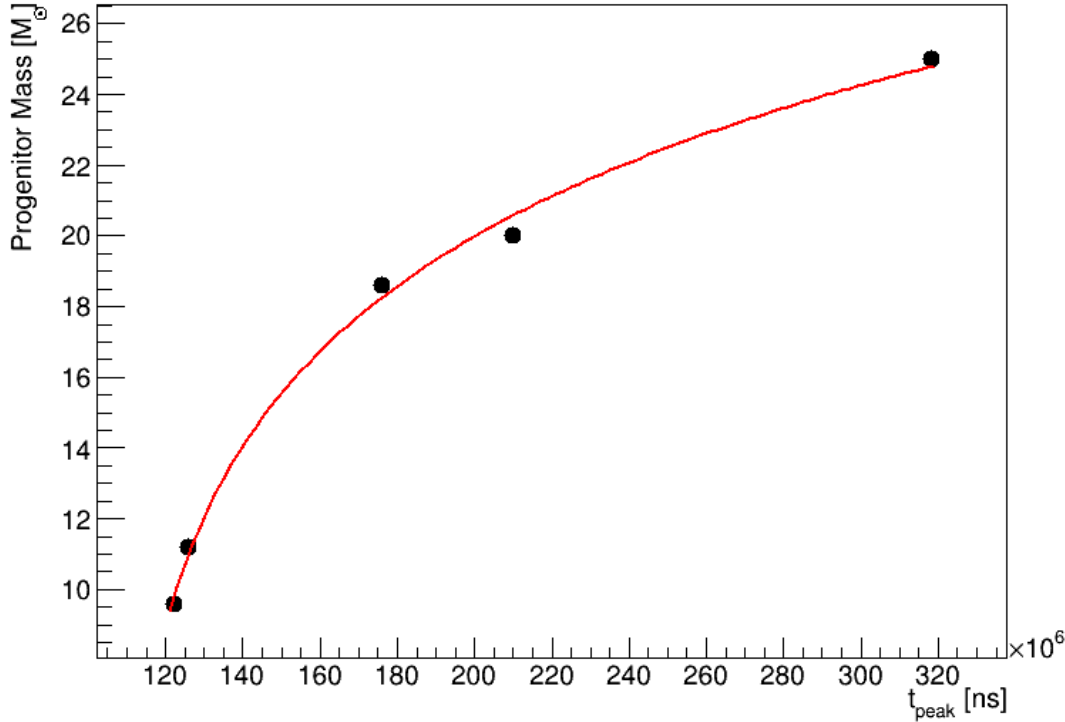


Figure 6.3: Fit on the correlation between the progenitor mass and the time peak to find a functional form for the Garching Model

in the function. The fit in the two cases returns the following two functions:

$$M(t) = 6.0[\text{Log}(t - 1 \cdot 10^8) - 15.0] \quad (6.1)$$

$$M(t) = 27.8[\text{Log}(t - 0.0005) - 19.0] \quad (6.2)$$

Thanks to this relationship is now possible to build a correlation matrix and the Toy Model linking the two variables. A un-normalized likelihood is generated from this relationship extracting 100000 values randomly following a uniform distribution, within the range of the sigmas extracted from the fit. The likelihood is then normalized to 1 to build the correlation matrix. The correlation matrix is shown in Fig. 6.5 and Fig. 6.6 for both cases.

The aforementioned unfolding matrices have been obtained with the same probabilistic procedure described in Section 5.3.

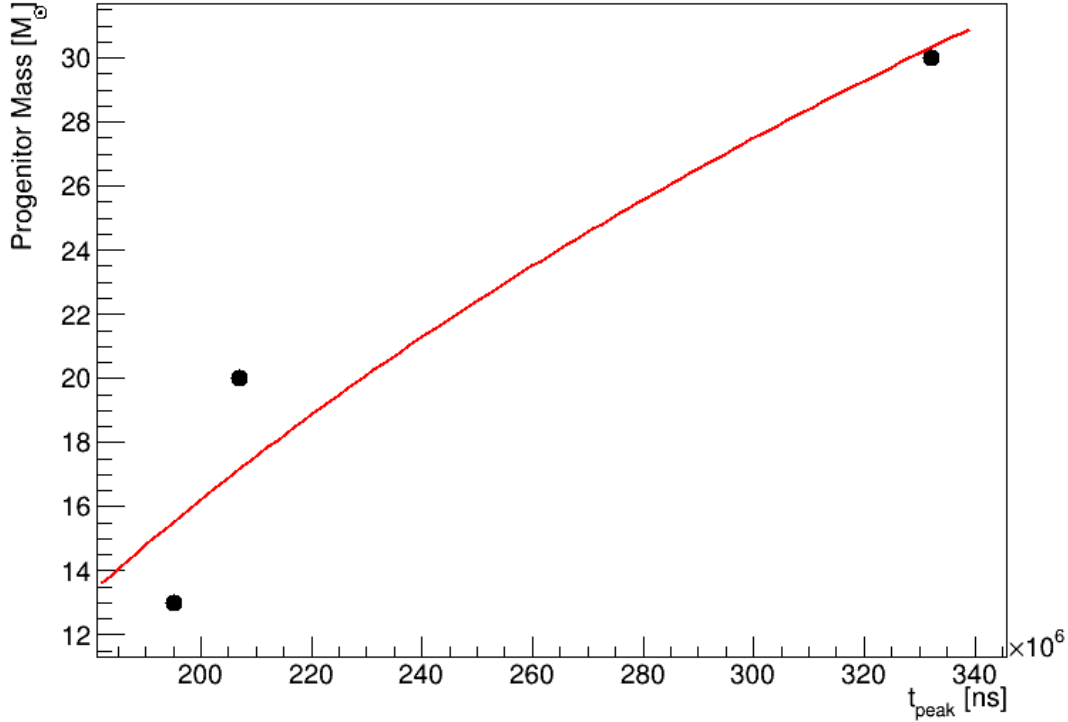


Figure 6.4: Fit on the correlation between the progenitor Mass and the time peak for the Nakazato Model.

6.1 Mass Reconstruction

Once the unfolding matrix has been built, an independent SN burst can be simulated and unfolded. At first a single burst has been generated for each model. A $20 M_{\odot}$ for the Garching Model and a $13 M_{\odot}$ for the Nakazato Model. The respective ENF profile are shown in Fig. 6.7, and in Fig. 6.8, from which the peak time for the two can be extracted, resulting respectively in:

- $20 M_{\odot}$ $t_{peak} = 1.9 \cdot 10^8$ ns
- $13 M_{\odot}$ $t_{peak} = 1.5 \cdot 10^8$ ns

From the unfolding matrix is possible to extract a Mass distribution as a projection on the X axis of the Masses. So identifying the bin in which the peak time falls into to, will provide the corresponding mass distribution. Such distribution can be fitted by mean of a gaussian function to retrieve the mean value for the reconstructed Mass Progenitor. An example for two representative masses is shown in Fig. 6.9 and Fig. 6.10

The same procedure has been applied to all the available masses in both models, building a 68 % confidence level within which the progenitor mass can be given to the aforementioned probability. The result of the reconstructing algorithm is shown in Fig. 6.11.

The trend followed by the functional form shows that reconstructing a progenitor mass

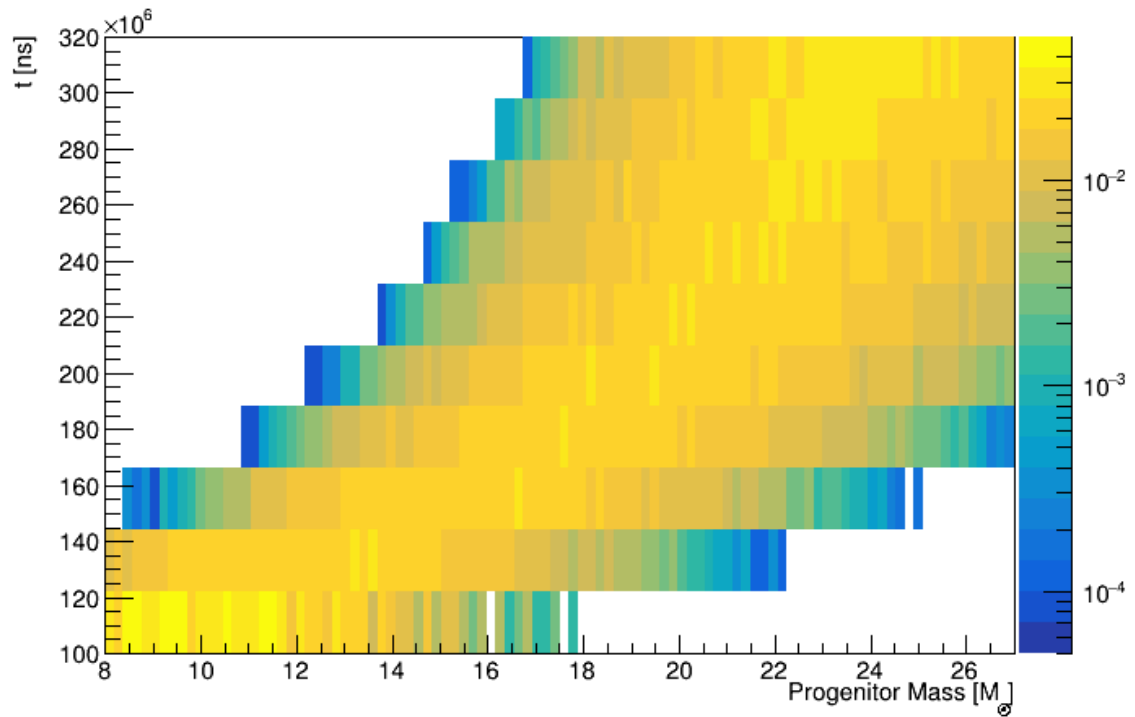


Figure 6.5: Correlation matrix between the peak time and mass progenitors for the Garching model

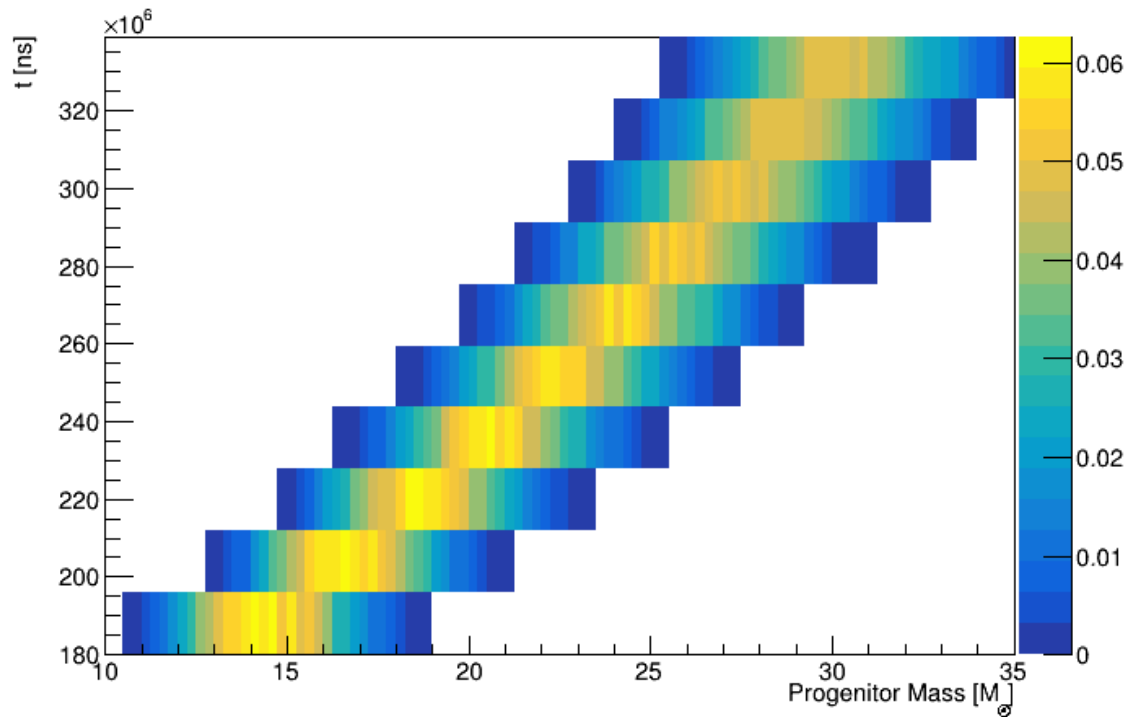


Figure 6.6: Correlation matrix between the peak time and Mass Progenitors for the Nakazato Model.

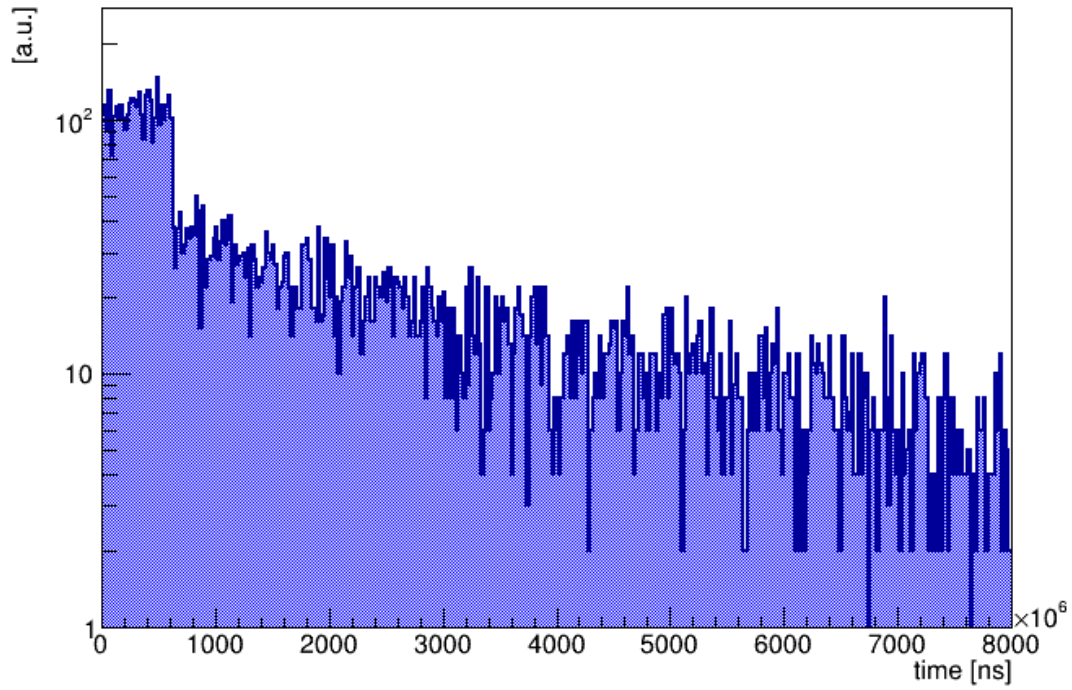


Figure 6.7: Hit-time profile for the 20 M_{\odot} for the Garching Model

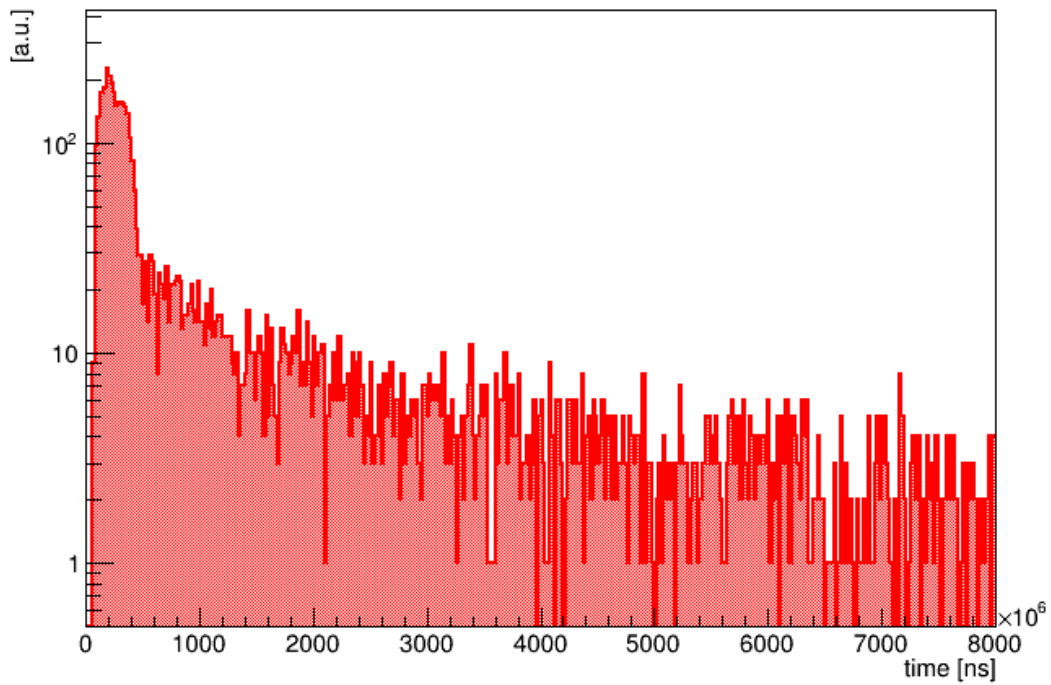


Figure 6.8: Hit-time profile for the 13 Nakazato M_{\odot}

will allow to identify a band within which at 68 % confidence level is the actual progenitor

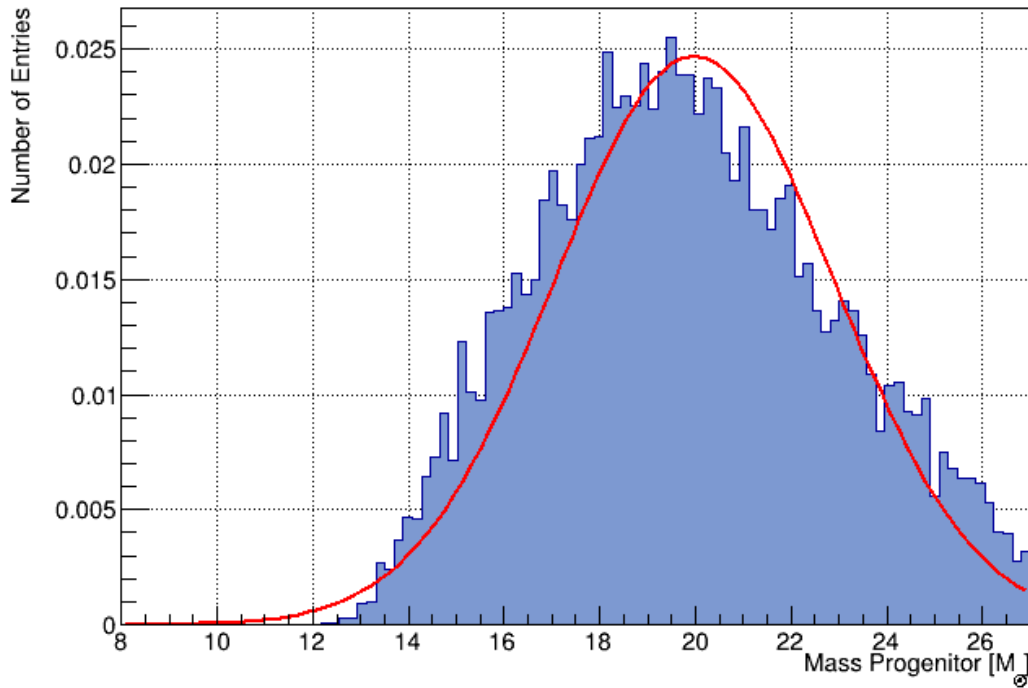


Figure 6.9: $20 M_{\odot}$ mass distribution extracted from the correlation matrix, corresponding to the 5th bin of the matrix

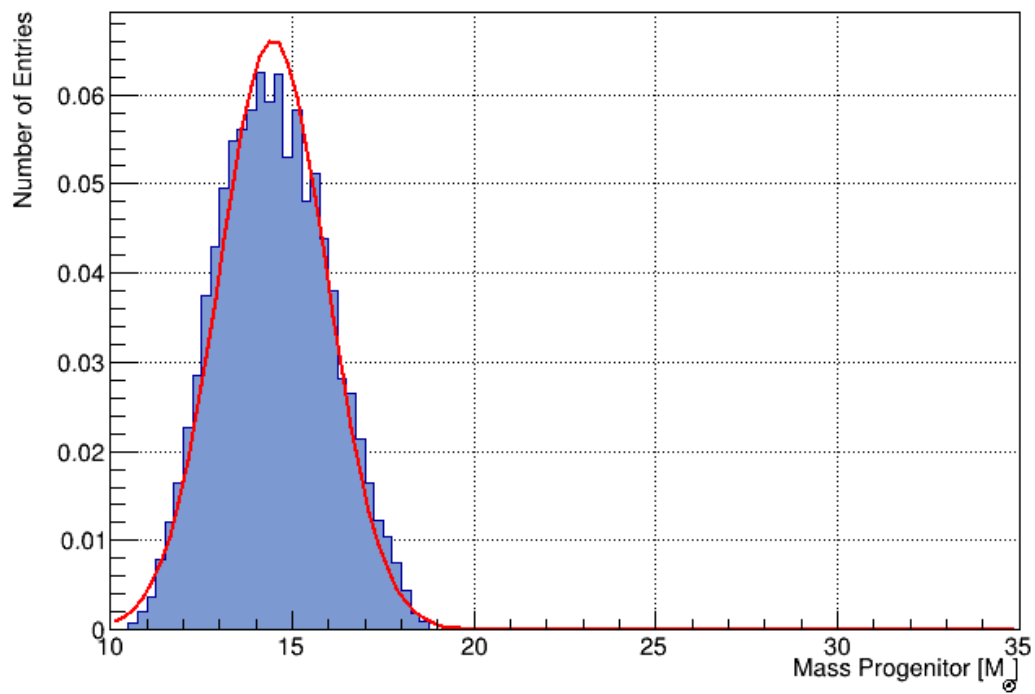


Figure 6.10: $13 M_{\odot}$ distribution extracted from the correlation matrix, corresponding to the 1st bin of the matrix

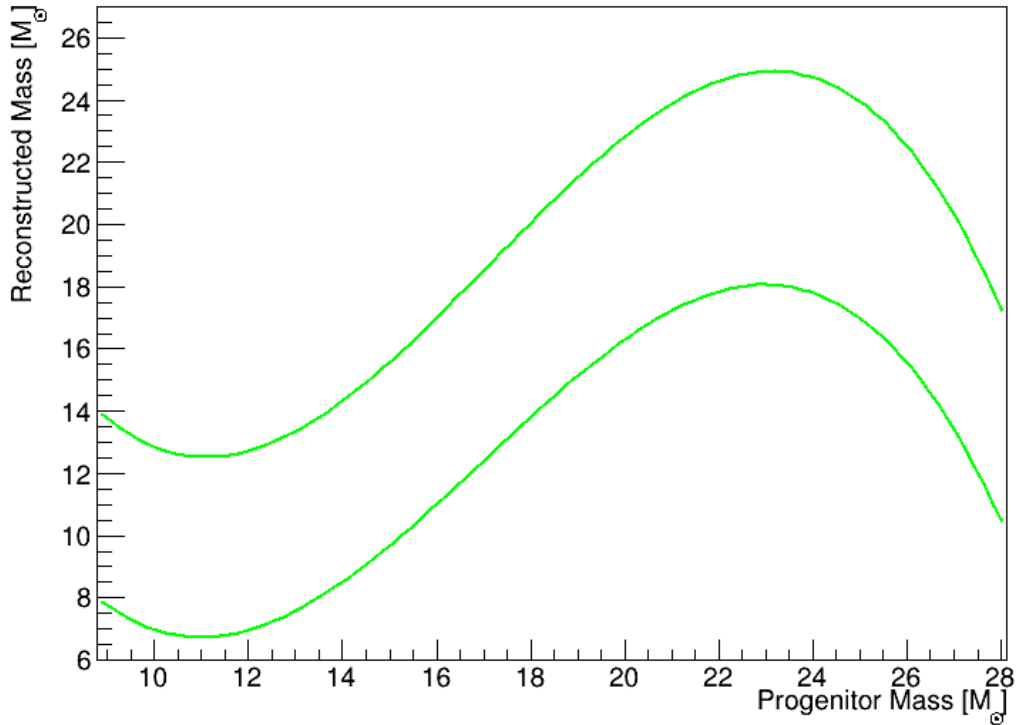


Figure 6.11: Mass Reconstruction at 68% confidence level. The trend followed by the functional form shows that reconstructing a progenitor mass will allow to identify a band within which at 68 % confidence level is the actual progenitor mass of the SN explosion. The trend shows that after the 24-25 M_{\odot} the function starts decreasing again, which is not surprising since this is, the theoretical limit for which a SN goes into a black hole formation, rather than a neutron-proton star; this means that more material gets burn in the explosion because much more powerful, and the event rate will decrease as well, becoming comparable to the low masses range. With comparable number of events between two different class of SN mass progenitor, the integrated number of them within the first 100 ms differs enough to distinguish the two classes and place the reconstructed mass within the right range. For example for the 11.2 M_{\odot} is on average about 88 events, while for a 27 M_{\odot} is on average about 170 events.

mass of the SN burst. The trend shows that after the 24 M_{\odot} the function starts decreasing again, which is not surprising since this is, the theoretical limit for which a SN goes into a black hole formation; this means that more material gets burn in the explosion and the event rate decreases as well, becoming comparable to the low masses range. With comparable number of events between two different class of SN mass progenitor, the integrated number of them within the first 100 ms differs enough to distinguish the two classes and place the reconstructed mass within the low range class, rather than in the high range class, for example the number of events in the first few 100 ms for a 11.2 M_{\odot} is averaged on 10 SN simulation about 88 events, while for a 27 M_{\odot} is averaged on 10 SN simulation 170 events The method has given a very promising way to extract the mass distribution of the original progenitor from the study of the time distribution of a SN burst. Due to

the difficulties and ambiguities at the present time in inferring a SN mass progenitor due to differences in models and simulations, this probabilistic approach can open new possibilities to learn important information about the initial star that caused the explosion, starting from the detection of the neutrinos released by it.

Despite the efficiency of the observable used for this analysis, the plan moving forward is to investigate and identify other possible variables in combination with the peak time that will allow a *ENF shape* discrimination to strengthen the methodology.

Summary and Conclusions

The observation of a galactic supernova is a rare event and it is therefore a rare opportunity to learn more about the last stage of a star's evolution and with that important neutrino properties can be inferred. The last ones in fact, play a crucial role in the process of a supernova. An explosion releases a conspicuous number of them in the space of just a few seconds. Characteristics, like their flavors or distribution depend on the properties of the progenitor star like its mass. Next generation of neutrino detectors will have a great opportunity to detect a full amount of neutrinos coming from a galactic supernova. The Jiangmen Neutrino Underground Observatory, with its 20 kton liquid scintillator, and its high energy resolution has great potential to observe neutrinos from a core-collapse supernova.

Supernova events are detectable in JUNO through different interaction channels, which have to be discriminated. A first discriminating algorithm has been presented in this work, through fiducial cuts that could help isolate single channels, thanks to a vertex reconstruction and a cut on the reconstructed charge for each channel. Method is implemented for the three main interaction channels, inverse beta decay, elastic scattering on protons and elastic scattering on electrons. A basic algorithm has been hereby presented to identify IBD with an efficiency of 74 % with a residual contamination of 7 % from protons and electrons, and 84 % detection efficiency on protons, with around 1 % residual contamination from anti-neutrinos and neutrinos from electrons.

Furthermore the unfolding of the supernova energy spectrum has been investigated by the use of a probabilistic Bayesian procedure. The reconstructed spectra closely match the true data, especially for the IBD event and the pES. The goodness of the reconstruction of the neutrino spectra is shown in this work, with a total uncertainty lower than 20 % mainly dominated by systematic uncertainties, in the range from a few MeV up to 50 MeV, including all the three main channels investigated. The physical thresholds as well as the additional detector effect on the threshold of the processes have been considered. The evaluation of systematic uncertainties was just a first assessment and it could use further studies to complete the estimation of the full set of systematic involved. The unfolding of the eES channel leaves room for more improvement and further investigations.

At last, similar to the case of the unfolding of the spectrum, retrieved by the use of a probabilistic procedure, a probabilistic approach was applied to reconstruct the mass progenitor range from which the data was generated. The procedure was implemented finding

a correlation between the right observable and the true mass of the SN, and building a TOY Model to extract the probability of having a low range class, a middle range class and a high range class of mass progenitor reconstructed within a 68 % confidence level. Much controversy surrounds the inferred progenitor masses. The debate is nourished by discrepant results from different simulation models. Nevertheless the method hereby presented provides excellent premises, allowing the possibility to investigate new relationship between detectable observable in a neutrino detector and initial parameters of massive stars that undergo the process of SN explosion.

This work shows the capability of the JUNO detector to act as a optimum detector for supernova neutrino. Despite the strong results there is still room for improvements. Further studies on the variability of the distance have to be carried out, a first preliminary study has been done proving the ability of JUNO to still being able to detect around 1500 total events from a small mass progenitor such as $9.6 M_{\odot}$ up to 20 kpc with successful unfolding results with the methodology hereby presented.

Appendix A

Additional Unfolding Results

A.1 Additional Unfolding Results for the Nakazato Model

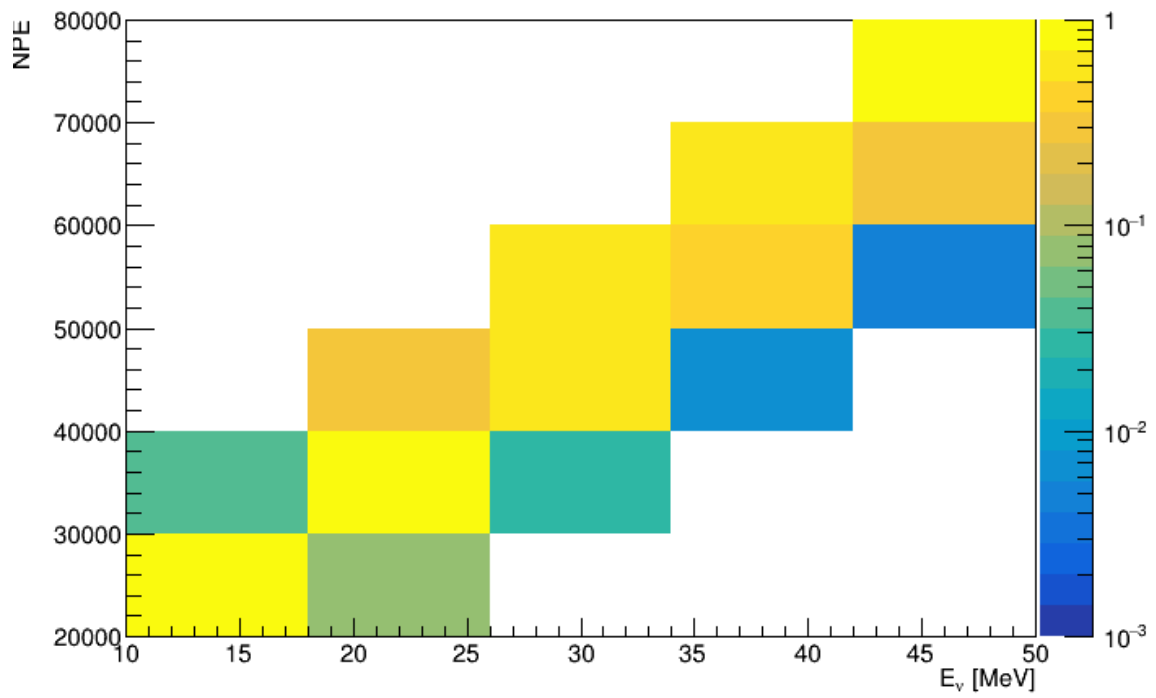


Figure A.1: Unfolding matrix for the IBD channel for the Nakazato Model for a $13 M_\odot$ mass progenitor.

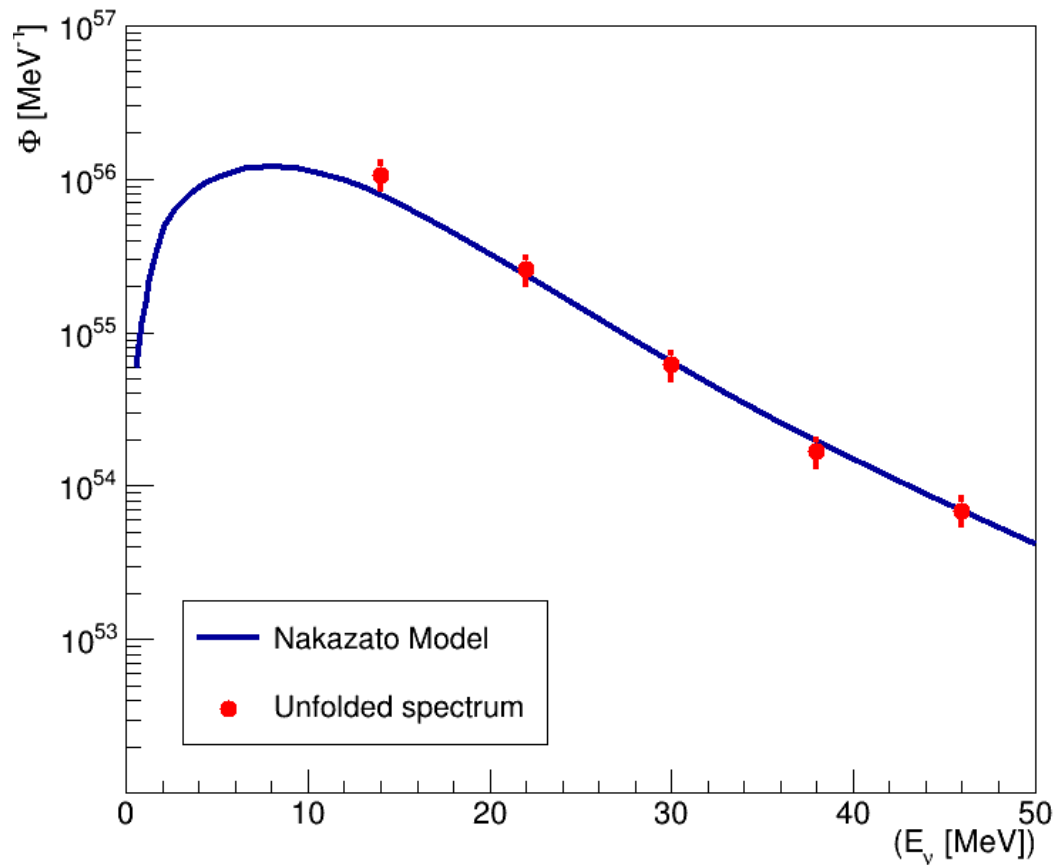


Figure A.2: The Unfolding result of a model with $13 M_\odot$ progenitor mass and Shen EoS at 10 kpc for IBD channel. The prior used is the one with metallicity equal to 0.02 and 300 ms of shock revival time building the prior from all the events. The uncertainties are evaluated to be around 30% between statistical one (10 %) and systematics due to the models (25%)

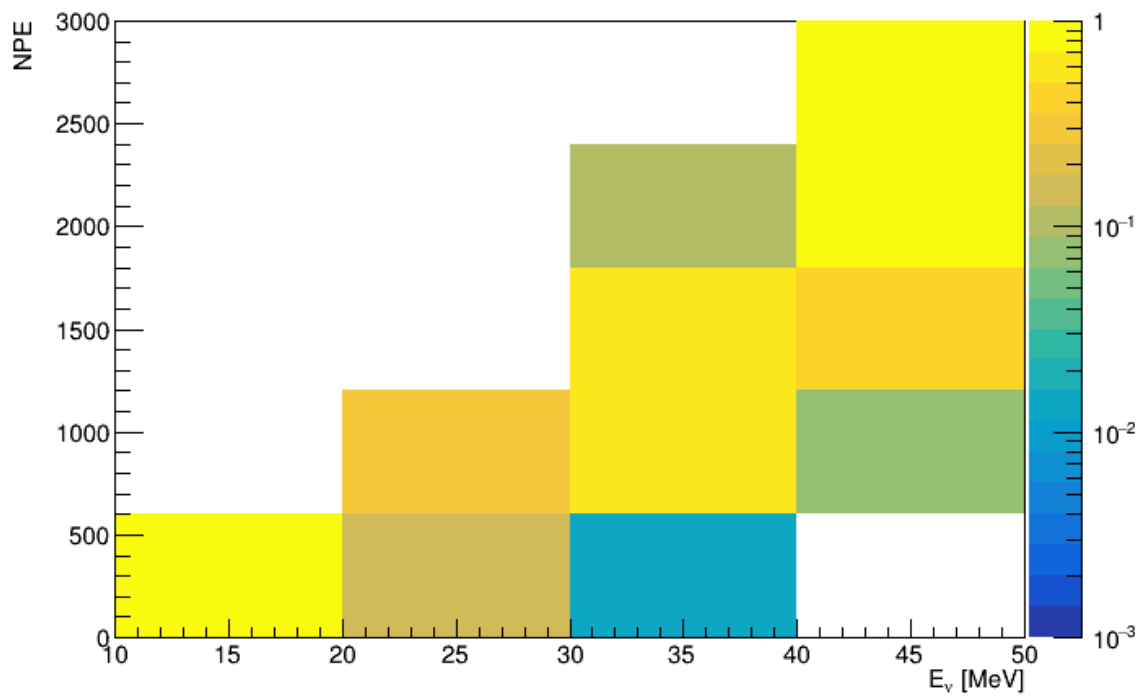


Figure A.3: Unfolding matrix for the pES channel for the Nakazato Model for a $13 M_{\odot}$ mass progenitor.

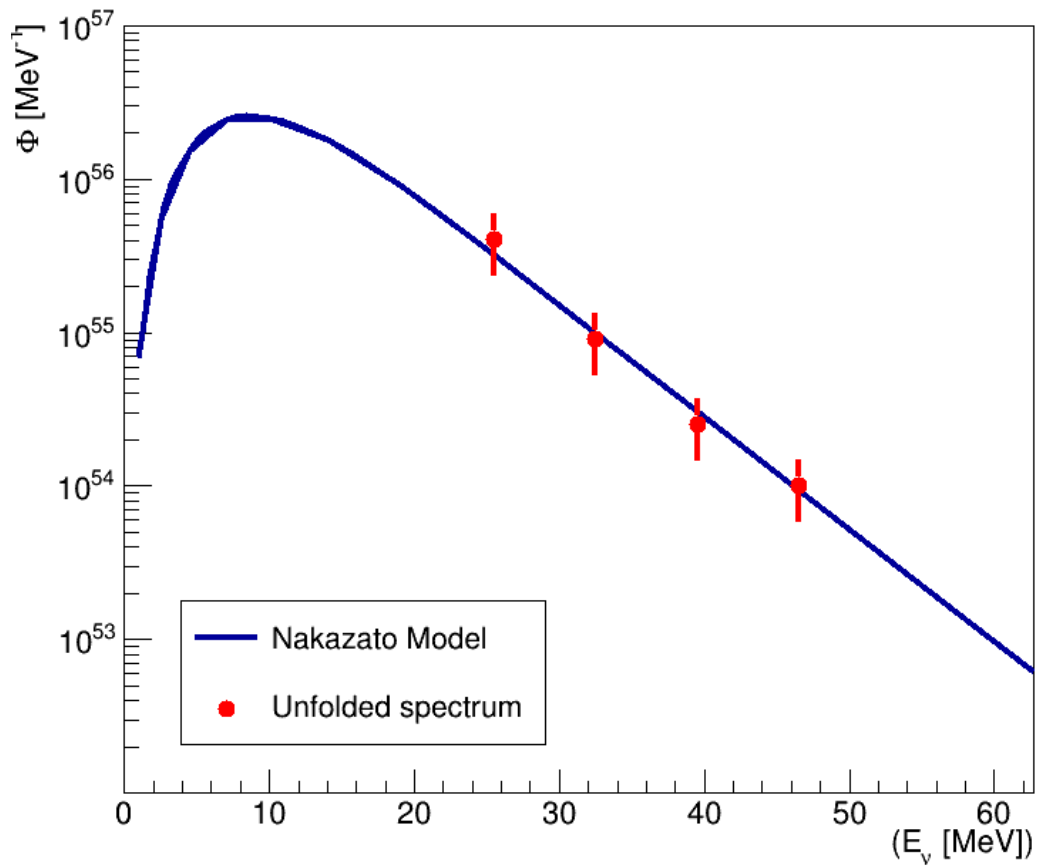


Figure A.4: The Unfolding result of a model with $13 M_\odot$ progenitor mass and Shen EoS at 10 kpc for pES channel. The prior used is the one with metallicity equal to 0.02 and 300 ms of shock revival time building the prior from all the events. As done for the IBD spectrum the uncertainties have been evaluated to be about 30 % between statistical (10 %) and systematics (25 %) due to the models.

Bibliography

- [1] W. D. Arnett, J. N. Bahcall, R. P. Kirshner, and S. E. Woosley, *Supernova 1987A*, Annual Review of Astronomy and Astrophysics **27** (1989) no. 1, 629–700.
- [2] H.-T. Janka, *Neutrino Emission from Supernovae*, pp. 1575–1604. Springer International Publishing, 2017.
- [3] V. Trimble, *Supernovae. Part I: the events*, Rev. Mod. Phys. **54** (1982) 1183–1224.
- [4] D. A. Green and F. R. Stephenson, *Historical Supernovae*, pp. 7–19. Springer Berlin Heidelberg, 2003.
- [5] B. E. K. Sugerman, *Discovery of a Light Echo from SN 2003gd*, The Astrophysical Journal **632** (2005) no. 1, L17–L20.
- [6] R. N. Manchester, B. M. Gaensler, L. Staveley-Smith, M. J. Kesteven, and A. K. Tzioumis, *Imaging of the Radio Remnant of SN 1987A at 12 mm Wavelength*, The Astrophysical Journal **628** (2005) no. 2, L131–L134.
- [7] S. Park, S. A. Zhekov, D. N. Burrows, and R. McCray, *SNR 1987A: Opening the Future by Reaching the Past*, The Astrophysical Journal **634** (2005) no. 1, L73–L76.
- [8] S. L. Shapiro and S. A. Teukolsky, *Black Holes, White Dwarfs, and Neutron Stars: The Physics of Compact Objects*, pp. 1–542. John Wiley & Sons, Ltd, 1983.
- [9] S. E. Woosley and T. A. Weaver, *The Physics of supernova explosions*, Annual Review of Astronomy and Astrophysics **24** (1986) 205–253.
- [10] M. M. Phillips, *The Absolute Magnitudes of Type IA Supernovae*, Astrophysical Journal Letters **413** (1993) L105.
- [11] M. Signore and D. Puy, *Supernovae and cosmology*, New Astronomy Reviews **45** (2001) no. 4, 409 – 423.
- [12] E. Cappellaro and M. Turatto, *Supernova Types and Rates*, pp. 199–214. Springer Netherlands, 2001.
- [13] F. Mannucci, M. Della Valle, N. Panagia, E. Cappellaro, G. Cresci, R. Maiolino, A. Petrosian, and M. Turatto, *The Supernova rate per unit mass*, Astronomy & Astrophysics **433** (2005) 807–814.

-
- [14] G. A. Tammann, *Supernova Statistics and Related Problems*, pp. 371–403. Springer Netherlands, 1982.
- [15] K. U. Ratnatunga and S. van den Bergh, *The Rate of Stellar Collapses in the Galaxy*, *Astrophysical Journal* **343** (1989) 713.
- [16] R. G. Strom, *Supernova Remnants I: Historical Events*, pp. 253–262. Springer Netherlands, 1990.
- [17] R. A. Muller, H. J. M. Newberg, C. R. Pennypacker, S. Perlmutter, T. P. Sasseen, and C. K. Smith, *High Rate for Type IC Supernovae*, *Astrophysical Journal Letters* **384** (1992) L9.
- [18] E. Cappellaro, M. Turatto, S. Benetti, D. Y. Tsvetkov, O. S. Bartunov, and I. N. Makarova, *The rate of supernovae. II. The selection effects and the frequencies per unit blue luminosity.*, *Astronomy & Astrophysics* **273** (1993) 383–392.
- [19] S. van den Bergh, *How rare are supernovae?*, *Comments on Astrophysics* **17** (1993) 125–130.
- [20] G. A. Tammann, W. Loeffler, and A. Schroeder, *The Galactic Supernova Rate*, *Astrophysical Journal Supplement* **92** (1994) 487.
- [21] R. G. Strom, “*Guest stars*”, *sample of completeness and the local supernova rate.*, vol. 288. 1994.
- [22] E. Cappellaro, M. Turatto, D. Tsvetkov, O. Bartunov, C. Pollas, R. Evans, and M. Hamuy, *The Rate of supernovae from the combined sample of five searches*, *Astronomy & Astrophysics* **322** (1997) 431–441.
- [23] F. X. Timmes, R. Diehl, and D. H. Hartmann, *Constraints from ^{26}Al Measurements on the Galaxy’s Recent Global Star Formation Rate and Core-Collapse Supernovae Rate*, *The Astrophysical Journal* **479** (1997) no. 2, 760–763.
- [24] P. M. Dragicovich, D. G. Blair, and R. R. Burman, *Why are supernovae in our Galaxy so frequent?*, *Monthly Notices of the Royal Astronomical Society* **302** (1999) no. 4, 693–699.
- [25] E. Cappellaro and M. Turatto, *Supernova Types and Rates*, pp. 199–214. Springer Netherlands, 2001.
- [26] B. C. Reed, *New Estimates of the Solar-Neighborhood Massive Star Birthrate and the Galactic Supernova Rate*, *The Astronomical Journal* **130** (2005) no. 4, 1652–1657.
- [27] S. Ando and K. Sato, *Relic neutrino background from cosmological supernovae*, *New Journal of Physics* **6** (2004) 170–170.

- [28] M. Malek et al., Super-Kamiokande Collaboration, *Search for Supernova Relic Neutrinos at Super-Kamiokande*, Phys. Rev. Lett. **90** (2003) 061101.
- [29] A. Burrows, D. Klein, and R. Gandhi, *The Future of supernova neutrino detection*, Phys. Rev. D **45** (1992) 3361–3385.
- [30] E. G. Jilinski, V. N. Frolov, J. K. Ananjevskaja, J. Straume, and N. A. Drake, *Memberships and CM diagrams of the open cluster NGC 7243*, Astronomy & Astrophysics **401** (2003) no. 2, 531—541.
- [31] S. A. Colgate and R. H. White, *The Hydrodynamic Behavior of Supernovae Explosions*, The Astrophysical Journal **143** (1966) 626.
- [32] S. Woosley and J. Thomas, *The physics of core-collapse supernovae*, Nature Physics **1** (2005) 147–154.
- [33] T. Totani, K. Sato, H. E. Dalhed, and J. R. Wilson, *Future Detection of Supernova Neutrino Burst and Explosion Mechanism*, The Astrophysical Journal **496** (1998) no. 1, 216–225.
- [34] T. A. Thompson, A. Burrows, and P. A. Pinto, *Shock Breakout in Core-Collapse Supernovae and Its Neutrino Signature*, The Astrophysical Journal **592** (2003) no. 1, 434–456.
- [35] M. T. Keil, G. G. Raffelt, and H.-T. Janka, *Monte Carlo Study of Supernova Neutrino Spectra Formation*, The Astrophysical Journal **590** (2003) no. 2, 971–991.
- [36] A. Burrows and T. A. Thompson, *The Mechanism of Core-Collapse Supernova Explosions: A Status Report*, pp. 53–62. Springer Berlin Heidelberg, 2003.
- [37] V. Trimble, *1987A: The greatest supernova since Kepler*, Rev. Mod. Phys. **60** (1988) 859–871.
- [38] J. C. Wheeler, *Resource Letter: OTS-1: Observations and theory of supernovae*, American Journal of Physics **71** (2003) no. 1, 11–22.
- [39] K. Hirata et al., *Observation of a neutrino burst from the supernova SN1987A*, Phys. Rev. Lett. **58** (1987) 1490–1493.
- [40] K. S. Hirata et al., *Observation in the Kamiokande-II detector of the neutrino burst from supernova SN1987A*, Phys. Rev. D **38** (1988) 448–458.
- [41] R. M. Bionta et al., *Observation of a neutrino burst in coincidence with supernova 1987A in the Large Magellanic Cloud*, Phys. Rev. Lett. **58** (1987) 1494–1496.
- [42] C. B. Bratton et al., *Angular distribution of events from SN1987A*, Phys. Rev. D **37** (1988) 3361–3363.

-
- [43] T. Haines et al., *Neutrinos from SN1987a in the IMB detector*, Nuclear Instruments and Methods in Physics Research Section A: Accelerators, Spectrometers, Detectors and Associated Equipment **264** (1988) no. 1, 28–31.
- [44] E. Alexeyev, L. Alexeyeva, I. Krivosheina, and V. Volchenko, *Detection of the neutrino signal from SN 1987A in the LMC using the INR Baksan underground scintillation telescope*, Physics Letters B **205** (1988) no. 2, 209–214.
- [45] V. L. Dadykin, G. T. Zatsepin, V. B. Korchagin, P. V. Korchagin, and A. S. Mal'Gin, *Detection of a rare event with a neutrino detector under Mont Blanc on February 23, 1987*, Pisma v Zhurnal Eksperimentalnoi i Teoreticheskoi Fiziki **45** (1987) 464–466.
- [46] J. Middleditch et al., *A 2.14 ms candidate optical pulsar in SN1987A*, in *5th CTIO / ESO Workshop and 1st CTIO / ESO / LCO Workshop: SN 1987A: Ten Years After*. 2000. arXiv:astro-ph/0010044.
- [47] D. Wilkinson, *Analysis of neutron β -decay*, Nuclear Physics A **377** (1982) no. 2, 474–504.
- [48] T. J. Loredo and D. Q. Lamb, *Bayesian analysis of neutrinos observed from supernova SN 1987A*, Phys. Rev. D **65** (2002) 063002.
- [49] R. Cowsik, *Neutrino masses and flavors emitted in the supernova SN1987A*, Phys. Rev. D **37** (1988) 1685–1687.
- [50] F. An et al., *Neutrino physics with JUNO*, Journal of Physics G: Nuclear and Particle Physics **43** (2016) no. 3, 030401.
- [51] P. Lombardi et al., *Distillation and stripping pilot plants for the JUNO neutrino detector: Design, operations and reliability*, Nuclear Instruments and Methods in Physics Research Section A: Accelerators, Spectrometers, Detectors and Associated Equipment **925** (2019) 6–17.
- [52] R. Wang, H. Lu, and C. Yang, *Water Cherenkov detector of the JUNO Veto System*, Poster presented at the 2019 EPS Conference on High Energy Physics, 2019.
- [53] T. Adam et al., *The OPERA experiment Target Tracker*, Nuclear Instruments and Methods in Physics Research Section A: Accelerators, Spectrometers, Detectors and Associated Equipment **577** (2007) no. 3, 523–539.
- [54] G. Ranucci and E. Meroni, *Counting test facility for the Borexino experiment*, International Journal of Modern Physics A **29** (2014) 1442001.
- [55] A. Abusleme et al., JUNO Collaboration, *TAO Conceptual Design Report: A Precision Measurement of the Reactor Antineutrino Spectrum with Sub-percent Energy Resolution*, arXiv:2005.08745 [physics.ins-det].

- [56] D. V. Forero, R. Hawkins, and P. Huber, *The benefits of a near detector for JUNO*, arXiv:1710.07378 [hep-ph].
- [57] F. Marini, *The JUNO large PMT readout electronics*, Poster presented at the 2019 International Workshop on Weak Interactions and Neutrinos, 2019.
- [58] M. Bellato et al., *Embedded readout electronics R&D for the large PMTs in the JUNO experiment*, Nuclear Instruments and Methods in Physics Research Section A: Accelerators, Spectrometers, Detectors and Associated Equipment **985** (2021) 164600.
- [59] J. H. Zou, X. T. Huang, W. D. Li, T. Lin, T. Li, K. Zhang, Z. Y. Deng, and G. F. Cao, *SNiPER: an offline software framework for non-collider physics experiments*, Journal of Physics: Conference Series **664** (2015) no. 7, 072053.
- [60] S. Agostinelli et al., GEANT4 Collaboration, *Geant4 – a simulation toolkit*, Nuclear Instruments and Methods in Physics Research Section A: Accelerators, Spectrometers, Detectors and Associated Equipment **506** (2003) no. 3, 250–303.
- [61] V. Ivanchenko et al., *Recent Improvements in Geant4 Electromagnetic Physics Models and Interfaces*, Progress in Nuclear Science and Technology **2** (2011) 898–903.
- [62] S. C. Blyth, *Opticks : GPU Optical Photon Simulation for Particle Physics using NVIDIA® OptiX™*, Journal of Physics: Conference Series **898** (2017) 042001.
- [63] Z. Djurcic et al., JUNO Collaboration, *JUNO Conceptual Design Report*, arXiv:1508.07166 [physics.ins-det].
- [64] G. Group, *The Garching Core-Collapse Supernova Research*.
<https://wwwmpa.mpa-garching.mpg.de/ccsnarchive/>.
- [65] K. Nakazato, K. Sumiyoshi, H. Suzuki, T. Totani, H. Umeda, and S. Yamada, *Supernova Neutrino Light Curves and Spectra for Various Progenitor Stars: From Core Collapse to Proto-Neutron Star Cooling*, The Astrophysical Journal Supplement Series **205** (2013) 2.
- [66] S. Furusawa, K. Sumiyoshi, S. Yamada, and H. Suzuki, *Supernova equations of state including full nuclear ensemble with in-medium effects*, Nuclear Physics A **957** (2017) 188–207.
- [67] L. Hüdepohl, *Neutrinos from the Formation, Cooling, and Black Hole Collapse of Neutron Stars*. Dissertation, Technische Universität München, München, 2014.
- [68] I. Tamborra, G. Raffelt, F. Hanke, H.-T. Janka, and B. Müller, *Neutrino emission characteristics and detection opportunities based on three-dimensional supernova simulations*, Phys. Rev. D **90** (2014) 045032.

-
- [69] J. Kersten and A. Y. Smirnov, *Decoherence and oscillations of supernova neutrinos*, Eur. Phys. J. C **76** (2016) no. 6, 339.
- [70] L. A. Ahrens et al., *Measurement of neutrino-proton and antineutrino-proton elastic scattering*, Phys. Rev. D **35** (1987) 785–809.
- [71] T. Lin, J. Zou, W. Li, Z. Deng, X. Fang, G. Cao, X. Huang, and Z. Y. and, *The Application of SNI_{PER} to the JUNO Simulation*, Journal of Physics: Conference Series **898** (2017) 042029.
- [72] D. N. Schramm and J. W. Truran, *New physics from supernova 1987A*, Physics Reports **189** (1990) no. 2, 89 – 126.
- [73] M. Gonzalez-Garcia, M. Maltoni, and T. Schwetz, *Global analyses of neutrino oscillation experiments*, Nuclear Physics B **908** (2016) 199–217.
- [74] S. P. Mikheyev and A. Y. Smirnov, *Resonance Amplification of Oscillations in Matter and Spectroscopy of Solar Neutrinos*, Sov. J. Nucl. Phys. **42** (1985) 913–917.
- [75] A. Mirizzi, I. Tamborra, H.-T. Janka, N. Saviano, K. Scholberg, R. Bollig, L. Hudepohl, and S. Chakraborty, *Supernova Neutrinos: Production, Oscillations and Detection*, Rivista del Nuovo Cimento **39** (2016) no. 1–2, 1–112.
- [76] C. Patrignani et al., Particle Data Group, *Review of Particle Physics*, Chin. Phys. C **40** (2016) no. 10, 100001.
- [77] M. Kachelrieß, R. Tomàs, R. Buras, H.-T. Janka, A. Marek, and M. Rampp, *Exploiting the neutronization burst of a galactic supernova*, Phys. Rev. D **71** (2005) 063003.
- [78] J. Wallace, A. Burrows, and J. C. Dolence, *Detecting the Supernova Breakout Burst in Terrestrial Neutrino Detectors*, The Astrophysical Journal **817** (2016) no. 2, 182.
- [79] K. Scholberg, *Supernova signatures of neutrino mass ordering*, Journal of Physics G: Nuclear and Particle Physics **45** (2017) no. 1, 014002.
- [80] G. D’Agostini, *A multidimensional unfolding method based on Bayes’ theorem*, Nuclear Instruments and Methods in Physics Research Section A: Accelerators, Spectrometers, Detectors and Associated Equipment **362** (1995) no. 2, 487–498.
- [81] G. D’Agostini, *Improved iterative Bayesian unfolding*, [arXiv:1010.0632](https://arxiv.org/abs/1010.0632) [physics.data-an].